Calibration and wide field imaging with PAPER: a catalogue of compact sources

Author: **Liju Philip**

Supervisors: **Dr. Gianni Bernardi**
& Prof. Oleg M. Smirnov

A thesis submitted in fulfilment of the requirements
for the degree of Master of Science

in Physics

RHODES UNIVERSITY
Where leaders learn

Department of Physics and Electronics
Centre for Radio Astronomy Techniques and Technologies

March 7, 2016

Abstract

Observations of the redshifted 21 cm HI line promise to be a formidable tool for cosmology, allowing the investigation of the end of the so-called dark ages, when the first galaxies formed, and the subsequent Epoch of Reionization when the intergalactic medium transitioned from neutral to ionized. Such observations are plagued by foreground emission which is a few orders of magnitude brighter than the 21 cm line.

In this thesis I analyzed data from the Donald C. Backer Precision Array for Probing the Epoch of Reionization (PAPER) in order to improve the characterization of the extragalactic foreground component. I derived a catalogue of unresolved radio sources down to a 5 Jy flux density limit at 150 MHz and derived their spectral index distribution using literature data at 408 MHz.

I implemented advanced techniques to calibrate radio interferometric data that led to a few percent accuracy on the flux density scale of the derived catalogue. This work, therefore, represents a further step towards creating an accurate, global sky model that is crucial to improve calibration of Epoch of Reionization observations.

To my family for standing by me while I am gazing at the sky…

Acknowledgements

"In all your ways acknowledge Him, And He will make your paths straight. ∼Proverbs 3:6"

Dedicated to all those whose paths have crossed mine – it's an impossible task to summarize everything in this section, however, I make a humble effort by extending my heartfelt gratitude towards everyone who supported me during my M.Sc. journey, my sincerest apologies to anyone left out. I begin by thanking Oleg, our brave leader who funded my work via the NRF bursary scheme. Oleg handed me over to one of the best scientists in the league, my advisor – Gianni!!! Gianni's excellence reflects in his calm demeanour which always motivated me to push the envelope a bit further and nurture the scientist in me. My work would have been impossible without Griffin – the Python guru, his computer programming skills and astronomical knowledge successfully helped me move on in my research. I appreciate the RATT team for having me as a team member, to name a few – Ridhima deserves a standing ovation for her constant support during the whole journey, a genuine individual whom I can blindly fall back on. I thank her for motivating me to undergo a year of karate training, thus, helping me face tough times with a smile rather than with clenched fists. I also thank my close pals Alex, Eliz, Marcellin, Mark, Theo and Ulrich – for their selfless helping attitude and great company during my stay in Grahamstown. I thank Mrs. Ronel Groenewald for making most of my paperworks look extremely easy with her efficient management and office skills. I extend a special vote of thanks to the faculty and staff members of the Physics and Electronics Department at Rhodes University. I thank SKA-SA for helping me contribute towards the HERA-SA build-up in the Karoo desert near Carnarvon, South Africa. Apart from academia; I am extremely grateful towards my loving family – mom, dad and sister who backed me up at all times and helped me sail smoothly.

And above everything and everyone – I am grateful towards the Almighty for all His blessings in my life, and I conclude by saying – *the LORD has done this, and it is marvelous in our eyes. ∼Psalm 118:23.*

Contents

List of Figures

List of Tables

Chapter 1

Introduction

Cosmology has been transformed over the last two decades, moving into the so called era of "precision cosmology". We are witnessing the success of the "concordance model": a model that uses only six free parameters is now able to fit the best cosmological probes available to date, i.e. observations of the Cosmic Microwave Background (CMB, Planck Collaboration, 2015) the large scale structure (Tegmark et al., 2006) and the baryonic acoustic oscillations (Seo & Eisenstein, 2005; Xu et al., 2010). In this model, the large scale structure observed today grows from tiny perturbations in the photon baryon fluid generated after inflation. At z $\sim$ 1100 the Universe cooled down sufficiently to allow the formation of neutral Hydrogen (HI) and from that moment onwards, matter and radiation evolved independently. Perturbation in the matter density grew under gravitational attraction until local overdensities were sufficient to form the first stars and galaxies. As galaxy formation progressed, the HI in the InterGalactic Medium (IGM) eventually became ionized again. There are many evidences of the occurrence of such Epoch of Reionization (EoR), mostly coming from observations of the Gunn-Peterson trough towards distant quasars (Becker, Bolton & Lidz, 2015; Mortlock, 2015), of the CMB optical depth to Thomson scattering (Reichardt, 2015) and of the Lyα dropout in high redshift galaxies (Pentericci et al., 2014; Stark et al., 2011). However, even the combination of the various data is only able to provide a superficial, broad description of the reionization as a global process, barely constraining its duration (Robertson, Ellis, Furlanetto & Dunlop, 2015). The 21 cm line from neutral Hydrogen has been largely indicated to be the best probe of the reionization as it directly probes the evolution of the IGM (Barkana & Loeb, 2001; Furlanetto, Peng Oh & Briggs, 2006; Madau, Meiksin & Rees, 1997). In the next section I will give an overview of the theoretical framework of the 21 cm line in a cosmological context.

1.1 The Hyperfine 21 cm Hydrogen line

The abundance of Hydrogen in the universe combined with its major phase transition from being once neutral (HI) to ionized (HII) state makes it an extraordinary resource for studying the processes responsible for reionization. The HI 21 cm line arises from the electron spin flip relative to the nucleus, where the electron-proton parallel-parallel spin configuration has slightly higher energy than its parallel-antiparallel configuration. In the rest frame, the transition between these two states results in emitting a photon with frequency $\nu = 1420.41$ MHz. If emitted by a high redshift cloud, the 21 cm line will experience the usual $(1+z)$ frequency stretch and, for the redshift range relevant to reionization studies, it will be observable in the meter wavelength regime.

In the cosmological context, the 21 cm emission is always observable as a contrast with the CMB that provides a background radiation. If T_γ is the CMB temperature, the 21 cm emission will be observable if $T_s \neq T_\gamma$, where T_s is the 21 cm spin temperature that drives the population of the excited hyperfine level. T_s inevitably tends to T_γ unless there is a mechanism that couples it to the gas temperature T_k, which is the only other variable in the game. There are two main mechanisms that achieve coupling between T_s and T_k:

- collisional coupling, that dominates at early times when the gas density is high;
- the Wouthuysen-Field (WF, Field, 1959; Wouthuysen, 1952) effect. The WF effect couples T_s to T_k via the resonant scattering of Lyα photons by HI atoms. Figure 1.2 illustrates it: the HI hyperfine level can be populated via the absorption of a Lyα photon from an electron in the fundamental level and the consequent re-emission of photons with intermediate energy. Quantum selection rules allow the electron to decay to the hyperfine level and, with a consequent decay to the fundamental state, to emit a 21 cm photon. The WF effect is the main coupling mechanism once the first luminous sources are formed.

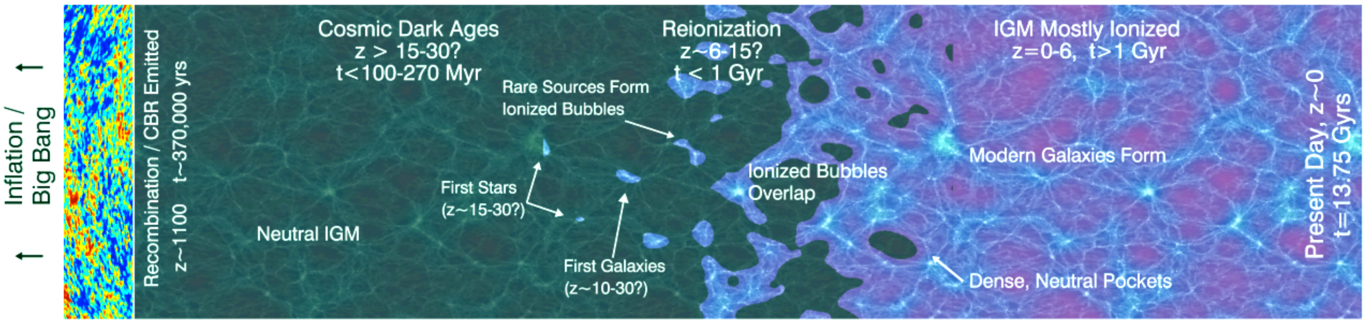

FIGURE 1.1: The transition of neutral intergalactic medium (post recombination z ∼1100) to fully ionized state (Robertson et al., 2010).

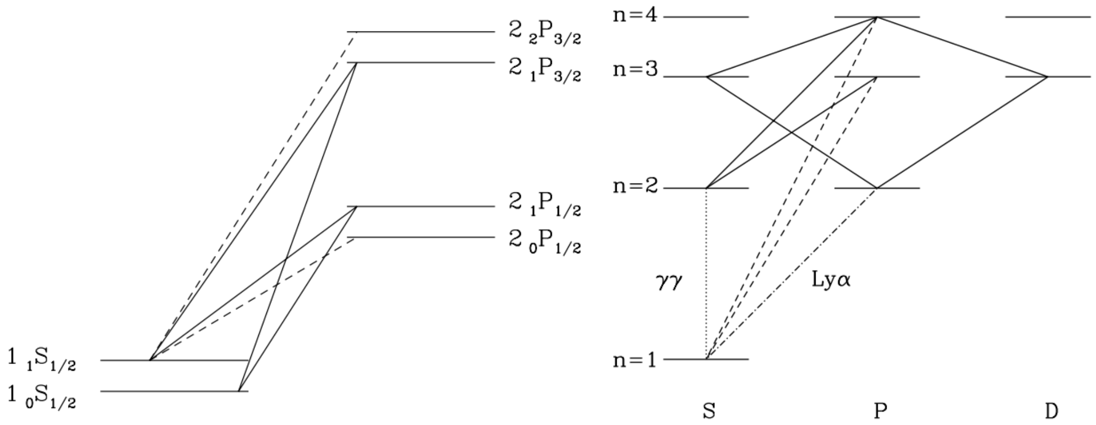

FIGURE 1.2: Diagram describing the Wouthuysen-Field effect, with the hyperfine slitting of the fundamental S and the excited P levels. Solid lines indicate transitions that populate the hyperfine levels from the ground state (from Furlanetto et al., 2006).

The general expression of the 21 cm brightness temperature fluctuations T_b with respect to the CMB temperature can be derived by equating absorption and emission in a HI cloud, leading to (i.e. Mesinger et al., 2015):

$$\delta T_b(\nu) \approx 27 x_{\mathrm{HI}} \left(1 - \frac{T_\gamma}{T_s}\right)(1+\delta)\left(\frac{H(z)(1+z)}{d\nu_r/dr}\right)\left(\frac{1+z}{10}\frac{0.15}{\Omega_m h^2}\right)^{\frac{1}{2}}\left(\frac{\Omega_b h^2}{0.023}\right)\left(\frac{1-Y_p}{0.75}\right)\mathrm{mK} \tag{1.1}$$

where x_{HI} is the HI neutral fraction, δ denotes the density contrast, $d\nu_r/dr$ is the comoving gradient of the line of sight velocity component, $H(z)$ is the Hubble parameter, Ω_m and Ω_b are the matter and baryon densities respectively and Y_p is the Helium mass fraction.

This basic knowledge is sufficient to understand the predicted evolution of the 21 cm signal.

1.2 Evolution of the 21 cm signal with cosmic time

The 21 cm brightness temperature T_b can be described by a spatially–averaged (or sky–averaged or global) component that retains only the dependence on the redshift evolution and a fluctuating component that describes spatial and redshift variations in T_b.

A cartoon representation of the evolution of the 21 cm brightness temperature is displayed in the top panel of Figure 1.3, whereas the bottom panel shows a fiducial model of the global 21 cm signal. The evolution of the global 21 cm signal is marked by several turning points (i.e. Furlanetto, 2015; Pritchard & Loeb, 2010)

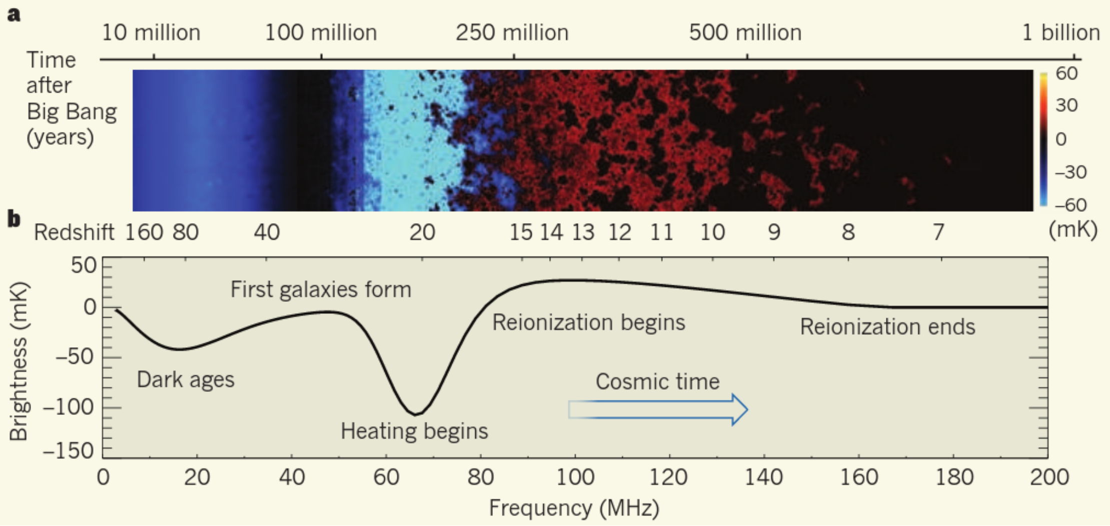

FIGURE 1.3: Upper panel: two dimensional slice of the time evolution of the 21 cm brightness temperature, T_b (from Mellema et al., 2006). Lower panel: predicted time evolution of the global 21 cm brightness temperature with relevant epochs highlighted (from Pritchard & Loeb, 2010).

- at $z > 200$ Compton heating keeps T_k tightly coupled to T_γ, therefore no 21 cm emission is expected from this epoch;

- at $z \sim 200$, Compton heating is no longer efficient to couple T_k to T_γ, whereas collisional coupling is effective in driving T_s to T_k. As the gas cools adiabatically faster than the CMB, we expect to see the 21 cm signal in absorption against the CMB. By $z \sim 80$, collisional coupling is no longer effectively coupling T_s to T_k and T_s eventually reaches T_γ at $z \sim 30$, making the 21 cm signal disappear. This epoch is often referred to as the “Dark Ages” and is governed by well understood atomic physics and the standard cosmology, at least in the absence of any exotic process that may input energy into the IGM (i.e. Valdes et al., 2010). The 21 cm signal from the “Dark Ages” therefore provides a clear probe of cosmology.
  Fluctuations in T_b are essentially driven by density fluctuations which follow, in turn, dark matter fluctuations. Observations of the 21 cm fluctuations from the Dark Ages have indeed been suggested to be one of the most powerful probes of the dark matter power spectrum (Loeb & Zaldarriaga, 2004);

- at $z \sim 30$ the first luminous sources are expected to form in the Universe. This epoch is indeed often referred as to the “Cosmic Dawn”. These sources are likely to be massive stars which generate a Lyα background that generates the 21 cm signal via the WF effect. Although the specific features of the global 21 cm evolution are now significantly model dependent, the fiducial model of Figure 1.3 captures the overall behaviour. As the gas keeps cooling and the WF is effective, T_b is driven to a minimum towards $z \sim 25 - 20$. The amplitude and redshift of the peak are due to the relative X–ray and Lyα production from first sources. Massive X–ray binaries (i.e. Pritchard & Furlanetto, 2007) or miniquasars (i.e. Zaroubi et al., 2007) can generate a significant amount of X–ray emission that will, in turn, heat the gas. Such heating would, therefore, precede the peak of the WF coupling and substantially reduce the peak of the absorption trough at $z \sim 25$, driving the 21 cm signal in emission against the CMB background already at $z > 20$. Conversely, a low X-ray emissivity, will delay gas heating, leading to a deeper peak and wider absorption trough (i.e. Pritchard & Loeb, 2010).

The 21 cm signal is a powerful probe of the early X–ray sources: Pacucci et al. (2014) showed that a significant X–ray emission can come from the hot InterStellar Medium and, if this is the dominating mechanism in the early Universe, the 21 cm signal is expected to be a factor of ~ 3 brighter than if massive X–ray binaries are dominant. Similarly, the WF coupling is sensitive to the star population, with a closer space between the WF and heating epochs and a weaker peak if the first luminous sources are essentially Pop III stars.

Fluctuations in the 21 cm T_b are initially driven by T_s fluctuations but are subsequently dominated by fluctuations in the gas temperature T_k when heating becomes significant;

- by $z \sim 15$ the HI gas is expected to have been heated above the CMB temperature and the 21 cm signal turns now into emission against the CMB in most models. In the fiducial model of Figure 1.3, $T_k \gg T_\gamma$ at $z \sim 15$, saturating the dependence on the spin temperature that drops from Equation 1.1. Reionization is believed to start around this epoch with the first galaxies producing sufficient ionizing photons to escape the host galaxy and ionize the IGM (i.e. Barkana & Loeb, 2004; Ciardi et al., 2003; Mellema et al., 2006). Fialkov, Barkana & Visbal (2014) have, however, suggested that the IGM may instead remain cold until the midpoint of reionization ("cold reionization"), in which case the 21 cm emission would appear in absorption against the CMB up to $z \sim 10$.

  As galaxies are effective in continuing to ionize the IGM, however, the HI fraction keeps decreasing until approaches zero around $z \sim 6$ (Fan, Carilli & Keating, 2006) and the 21 cm signal signal vanishes. T_b fluctuations are driven by fluctuations in the HI fraction, encoding the physics details of ionizing sources and IGM feedback (Ghara, Choudhury & Datta, 2015) as it will be described in the next section.

The evolution of the global 21 cm signal is therefore a very sensitive probe of the physical processes occurring in the high$-z$ Universe. As previously mentioned, every component of Equation 1.1 can also fluctuate spatially and such fluctuations are rich in physical information that may be averaged out in the global 21 cm signal. In the next section we will describe the main features of 21 cm fluctuations.

1.3 Fluctuations in the 21 cm signal

Theoretical simulations have predicted 21 cm fluctuations for over a decade (Barkana & Loeb, 2008; Morales & Wyithe, 2010). The connection between simulated image cubes and input physical parameters is still, however, difficult to establish (Iliev et al., 2015; Mellema et al., 2015). Different statistics have, therefore, been developed in order to encapture information from simulations and link them to the actual physical parameters. The most widely used statistics is the power spectrum $P(k)$ of the 21 cm brightness temperature T_b (Furlanetto, Peng Oh & Briggs, 2006; Morales & Hewitt, 2004):

$$\langle T_b(\vec{k})\, \tilde{T}_b(\vec{k}')\rangle = (2\pi)^3\delta^3(k-k')P(k) \tag{1.2}$$

where $\vec{k}$ is the Fourier conjugate of the three dimensional spatial coordinate $\vec{x}$, $\langle\rangle$ indicates the ensemble average and δ is the Dirac delta function. The power spectrum assumes spherical symmetry of the signal and does not, therefore, encaptures deviations due to, for example, redshift space distortions from gas peculiar velocities (Jensen et al., 2013). Due to the peculiar velocities, gas particles flow towards high-density regions and away from low density regions. The signal reaching the observer from the far side of high-density regions will tend to appear blue-shifted, making them appear closer than they are, whereas that from the near side will appear farther away.

Following Furlanetto (2015), we use Figure 1.4 from Mesinger, Furlanetto & Cen (2011) and Figure 1.5 (Lidz et al., 2008) to summarize the evolution of the 21 cm power spectrum through the Cosmic Dawn and the Epoch of Reionization. Figure 1.4 shows the evolution through the Cosmic Dawn, spanning the $10 \geq z \geq 30$ range:

- the top panel displays the impact of the birth of the first luminous sources on the 21 cm brightness temperature, when the WF effect becomes effective. Fluctuations are here driven by the clustered distribution of the first sources that couple T_s to T_k around them, leaving the rest of the IGM neutral;
- the second panel from the top illustrates T_b fluctuations shortly after X–ray heating began ($z \sim 20$). Most of the IGM is still seen in absorption but it has been heated around the first sources to $T_s = T_k \gg T_\gamma$ and is, therefore, seen in emission. This generates a large contrast between emitting and absorbing regions, driving an increase in the power spectrum amplitude by nearly one order of magnitude;

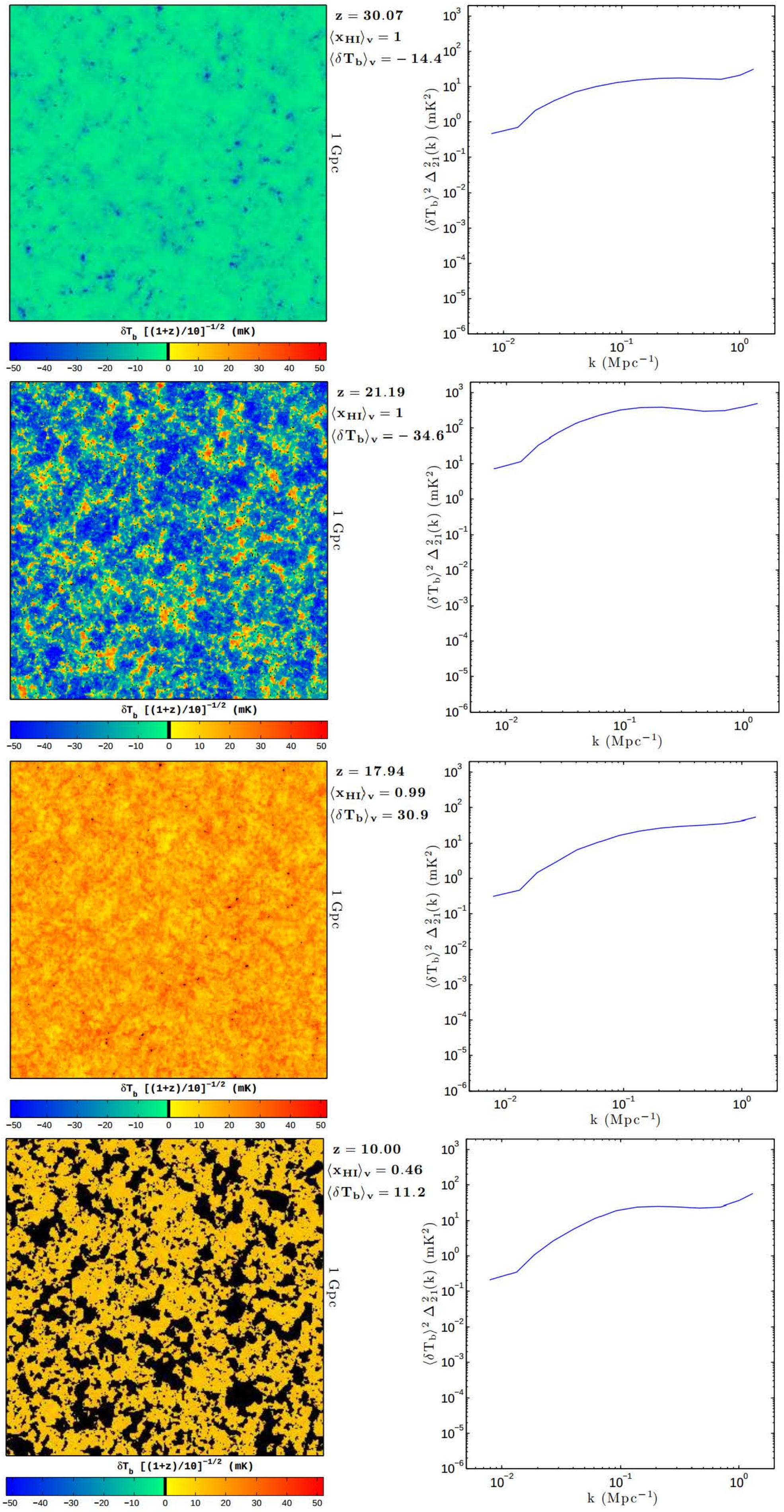

FIGURE 1.4: Panels from top to bottom show various epochs in the cosmic 21 cm signal (Mesinger et al., 2011). It slices through δT_b simulation (*left*) and the corresponding 3D power spectra (*right*) at $z = 30.1$, 21.2, 17.9 and 10.0.

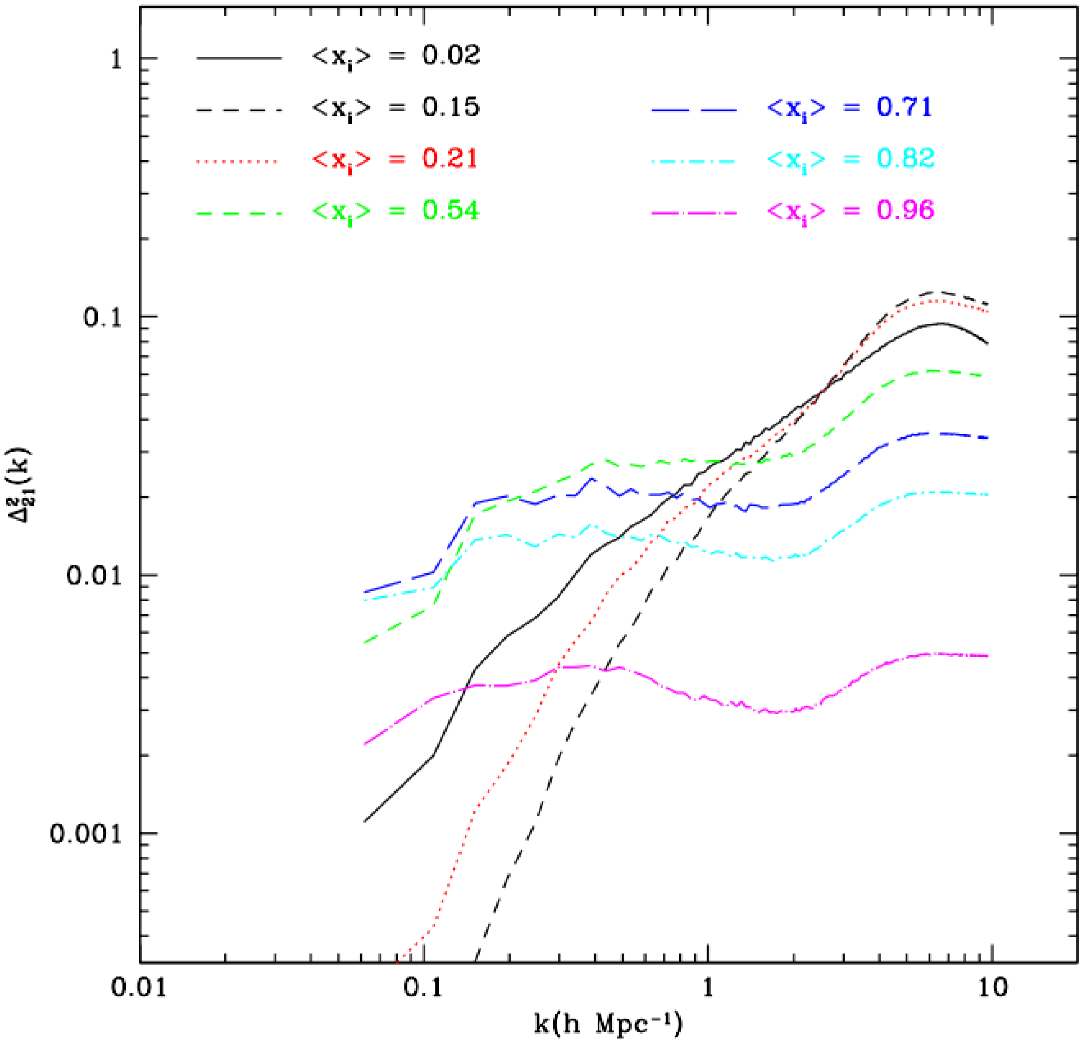

FIGURE 1.5: Evolution of the spherically averaged 21 cm power spectrum (Lidz et al., 2008). The ionization fraction parameters marks the redshift evolution. The wide variations in power spectrum amplitude (approximately two orders of magnitude) and slopes are clear features that can be tested by observations.

- the second panel from the bottom displays T_b fluctuations when the spin temperature saturates ($T_s = T_k \gg T_\gamma$, $z \sim 15$). T_s fluctuations no longer contribute significantly to T_b fluctuations, whereas density fluctuations contribute the most. The resulting power spectrum, therefore, decreases in amplitude by about one order of magnitude. As mentioned earlier, there are models, however, that predict a weaker heating of the IGM which would still have, at $z \sim 15$, T_b fluctuations dominated by gas fluctuations, leading to a smaller decrease in the power spectrum amplitude;

- the bottom panel displays the onset of reionization. T_b fluctuations are here dominated by the contrast between neutral and ionized regions, that will grow throughout reionization.

Ionized bubbles are the key feature of reionization and their size and distribution depend essentially upon the ionizing sources (Zaldarriaga, Furlanetto & Hernquist, 2004). The evolution of the 21 cm power spectrum during reionization is shown in more detail in Figure 1.5, where it is plotted as a function of the ionization fraction x_i, which acts as time coordinate. When x_i is still low, the power spectrum still follows the density fluctuations (see second bottom panel of Figure 1.4). As reionization progresses, the large scale ($k < 1$ h Mpc^{-1}) power drops quickly because ionized bubbles appear in the densest regions first. Half way through reionization ($x_i = 0.5$), the contrast between ionized and neutral gas becomes the dominating term and the power spectrum peaks at the characteristic bubble scale (McQuinn et al., 2007). The general flattening of the power spectrum is eventually determined by the fact that x_i and δ are uncorrelated within the bubble size (Sobacchi & Mesinger, 2014), flattening the power spectrum on scales smaller than the bubble size. Eventually, as x_i increases, the power spectrum amplitude steadily decreases to zero.

The variations in power spectrum amplitude and slope of the 21 cm signal are the most promising observables for the current generation of radio interferometers, particularly throughout reionization. We will describe these prospects in the next chapter.

Chapter 2

Challenges in 21 cm observations, current status and thesis motivation

The theoretical scenario described in the previous section, motivated a renaissance in low frequency radio observations. The intrinsic faintness of the 21 cm signal needs exceptional sensitivity, requiring, in turn, dedicated instrumentation. Alongside with exceptional sensitivity, control over systematic errors is perhaps the biggest challenge in 21 cm observations. As we will describe in this section, the separation between bright foreground emission and the 21 cm is the key observational challenge. Such separation requires a careful calibration and modeling of the instrument and this is the most active research line that the observational community has been pursuing over the last years, in the effort to achieve the first detection of the 21 cm signal.

2.1 Foregrounds

In a seminal paper, Shaver et al. (1999) immediately pointed out that the foreground emission is a few orders of magnitude brighter than the expected 21 cm signal. The real challenge lies, therefore, in separating the 21 cm emission, which is expected to have a brightness temperature of few mK on a few arcmin angular scales, from a much brighter Galactic and extragalactic foreground emission. The success rate of 21 cm experiments relies on our understanding of the foregrounds and the development of effective foreground removal techniques which require studying their physics and impact on EoR experiments.

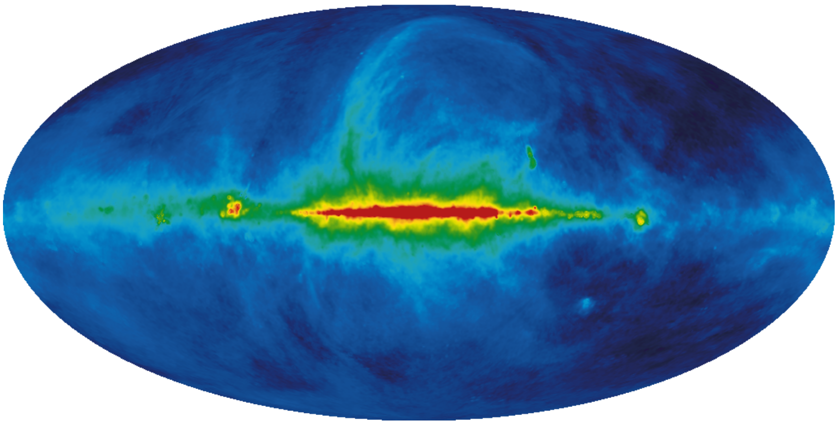

FIGURE 2.1: Galactic foreground (Haslam et al., 1982).

2.1.1 Galactic synchrotron emission

Synchrotron emission originates from relativistic electrons accelerated in a magnetic field. Synchrotron radiation from a single electron is highly anisotropic, beamed towards the direction of motion. A relativistic electron with energy $E = \gamma m_e c^2$, where γ is the Lorentz factor, m_e is the mass of the electron and c is the speed of light, emits at critical frequency ν_c:

$$\nu_c \sim \frac{\gamma^2 eB}{2\pi m_e c}$$

where B is the magnetic field strength. The synchrotron spectrum S emerging from a population of electrons emitting at a wide range of critical frequencies is, therefore, expected to span a wide range of frequencies and can be approximated by a power law (Rybicki & Lightman, 1979):

$$S_\nu \propto \nu^{-\beta} \tag{2.1}$$

where β can be related to the spectral energy distribution of the emitting electrons (Ginzburg & Syrovatskii, 1965).

When the intensity of synchrotron radiation or the electron density within a source is the sufficiently high, then the radiation can be (partially) absorbed by relativistic electrons themselves, leading to a characteristic peak in the synchrotron spectrum, below which $\beta \sim -0.5$. This phenomenon is termed *self absorption* and can be particularly prominent at low radio frequencies where the optical depth of the plasma is higher.

Synchrotron emission is the dominant emission mechanism for celestial radio sources at frequencies less than 2 GHz (i.e. Lawson et al., 1987). (Haslam et al., 1982) mapped the synchrotron emission at 408 MHz, showing that Galactic synchrotron emission varies significantly across the sky, where, outside the Galactic plane, shows a variety of features like spurs and cirrus, related to variations of the spectrum of relativistic electrons (i.e. Beuermann et al., 1985; Sironi, 1976). Beuermann et al. (1985) showed that the Galactic synchrotron radiation observed at 408 MHz can be explained by a model that described the emission from a thick disk (essentially the Galactic plane) and a thin disk (essentially the Galactic halo) whose sizes and emissivities are fit to the observational data.

The sky–averaged synchrotron spectrum is observed to be $\beta \sim 2.6 - 2.7$ although spatial variations up to $\Delta\beta \sim 0.3$ are common on degree scales (i.e. Lawson et al., 1987; Platania et al., 1998).

At low frequencies, the average spectrum seems to flatten $2.4 < \beta < 2.6$ (Bridle & Baldwin, 1967; Rogers & Bowman, 2008), although information about spatial variations of the spectral index are still very limited. Through the compilation of a wide range of surveys, de Oliveira-Costa et al. (2008) constructed an empirical model of the Galactic synchrotron emission from 10 MHz up to 90 MHz, which is still the state of the art in describing the spatial and spectral variation of the Galactic foreground.

2.1.2 Extragalactic foregrounds

Synchrotron radiation is also the dominant emission in extragalactic sources emitting at radio wavelengths. The brightest radio sources are classified as Active Galactic Nuclei (AGN), where the presence of a central supermassive black hole is believed to power the emission “jets” and “lobes” where relativistic electrons are accelerated in magnetic fields. Radio sources have been extensively studied through surveys over the last decades and we will focus here on the main results at low frequencies, where they constitutes ~25% of the total power in the radio sky (Di Matteo et al., 2002).

At 74 MHz, the Very Large Array Low-Frequency Sky Survey (VLSS, Cohen et al., 2007) surveyed the sky north of $\delta = -30$ down to a flux density of 0.7 Jy, with an angular resolution of $80''$. The Westerbork Northern Sky Survey (WENSS, Rengelink et al., 1997) is the deepest low-frequency radio survey at 325 MHz carried out using the Westerbork Synthesis Radio Telescope (WSRT) covering the sky region $\delta > +29°$, yielded 11299 sources at an angular resolution of $54'' \times 54''$ cosecδ. With the advent of the new low frequency instrumentation, surveys were carried out with the Low frequency ARray (LOFAR), the Murchison Widefield Array (MWA) and the Precision Array to Probe the Epoch or Reionization (PAPER). Hurley-Walker et al. (2014) carried out a $\sim$ 6100 deg^2 at $-58° < \delta < -14°$, with the MWA, covering the 104 - 196 MHz band with an angular resolution of $6' - 3'$. They compiled a catalogue complete down to 40 mJy beam^{-1}. Heald et al. (2015) carried out a LOFAR survey of 100 deg^2 centered at $(\alpha, \delta) = (15^{\rm h}, 69°)$, with an angular resolution of $\sim 2'$ over the 30 - 160 MHz frequency range. The resulting catalogue is complete down to 100 mJy at 105 MHz and 550 mJy at 60 MHz. Jacobs et al. (2011) detected $\approx$ 500 sources down to a flux density of 0.7 Jy, over a sky area of 4800 $\deg^2$ below $\delta = +10$ using the Precision Array for Probing the Epoch of Reionization (PAPER) at 145 MHz, with an angular resolution of $26'$.

Due to limited angular resolution, low frequency radio surveys are limited by confusion noise of ~ 3 mJy beam^{-1} (Bernardi et al., 2009, 2010). The construction of an all-sky catalogue of compact sources is not only useful for foreground subtraction as those sources can be modeled and removed from the data, but is important to accurately calibrate radio interferometric observations (see Chapter 3), a necessary requirement in order to detect the EoR signal.

2.2 The foreground separation problem

Several techniques have been proposed in the literature in order to separate foregrounds although they all rely on the different spectral behaviour between the foreground and the EoR signal. As (Galactic and extragalactic) foregrounds are synchrotron emitting sources, their spectrum is expected to be coherent (i.e. smooth) over tens of MHz whereas the EoR signal is only coherent on kHz scales due to the redshift evolution of the 21 cm signal (i.e. Santos et al., 2005; Zaldarriaga et al., 2004). That said, foreground separation methods are grouped in two different types: foreground removal and foreground avoidance.

2.2.1 Foreground removal

Foreground removal methods attempt to model and subtract the foreground emission from the data. These methods normally assume that a sky image cube is generated over a wide range of frequencies (i.e. $100 - 200$ MHz) and the foreground emission is modeled and subtracted along each line of sight (i.e. each image pixel). Subtraction methods are classified as parametric and non-parametric.

Parametric methods assume that the functional foreground spectrum is known and fit the function coefficients to the data. The most commonly adopted functional frequency form is polynomial or log-polynomial (Bowman et al., 2009; Gleser et al., 2008; Jelić et al., 2008; Liu et al., 2009; Petrovic & Oh, 2011; Santos et al., 2005; Wang et al., 2006). The advantage of parametric methods is their simplicity whereas the disadvantage is in the assumption of a known spectral form which may be incorrect at some level.

Unlike parametric methods, non-parametric methods attempt to use data properties to define the foreground model. Such methods include the minimization of spectral inflection points (Harker et al., 2009), spectral single value decomposition (Paciga et al.,

2013) and Generalized Morphological Component Analysis (Chapman et al., 2014). Non-parametric models are generally preferable as they do not impose a priori model, however, any subtraction method is limited by the accuracy achieved in the data calibration as calibration errors can impart deviations of the observed spectrum from smoothness (i.e. Morales et al., 2006).

2.2.2 Foreground avoidance

The foreground avoidance technique leverages on the foreground smoothness in order not to remove foreground emission, but to identify a region of parameter space (the EoR window) where the foreground contamination is minimal with respect to the EoR signal. Figure 2.2 illustrates the principle of the foreground avoidance scheme. Rather then using a spherically averaged power spectrum, a cylindrical representation that isolates the spatial from the spectral components can be adopted. This representation is function of two variables $(k_\perp, k_\|)$ (Liu et al., 2014a,b; Morales & Hewitt, 2004; Vedantham et al., 2014). Modes $k_\|$ and $k_\perp$ have respective constraints. The angular resolution of the instrument set by the longest baseline (b_{max}) defines the high $k_\perp$ boundary. The shortest baseline (b_{min}) approximate the angular extent of the interferometric array thus, forming a boundary for the low $k_\perp$ window. Boundaries at low and high $k_\|$ are defined by the bandwidth (B) of the instrument and the frequency resolution ($\Delta\nu$) of the observation respectively. Equations 2.2, 2.3, 2.4 and 2.5 define these boundaries as described in Chapman et al. (2014) and Vedantham et al. (2012), where $D_M(z)$ is the transverse comoving distance at redshift z, $\nu_{\rm HI} = 1420$ MHz is the rest frequency of 21 cm HI emission, $H_0 = 70$ km sec^{-1} Mpc^{-1} is the present value of the Hubble constant and $E(z) = \sqrt{\Omega_m(1+z)^3 + \Omega_\wedge}$.

$$k_{\perp max} = \frac{2\pi b_{max} \nu_{\rm HI}}{c(1+z)D_M(z)} \tag{2.2}$$

$$k_{\perp min} = \frac{2\pi b_{min} \nu_{\rm HI}}{c(1+z)D_M(z)} \tag{2.3}$$

$$k_{\| max} = \frac{2\pi H_0 \nu_{\rm HI} E(z)}{c(1+z)^2 \Delta\nu} \tag{2.4}$$

$$k_{\| min} = \frac{2\pi H_0 \nu_{\rm HI} E(z)}{c(1+z)^2 B} \tag{2.5}$$

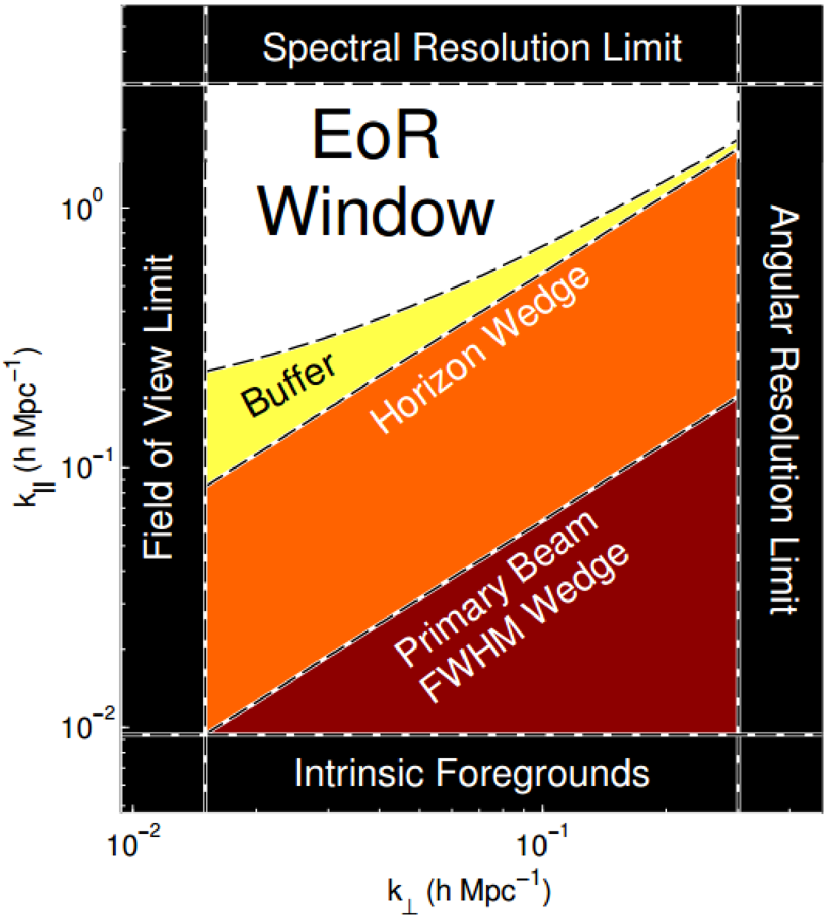

FIGURE 2.2: Cartoon of the avoidance scheme with the various regions highlighted (Dillon et al., 2015).

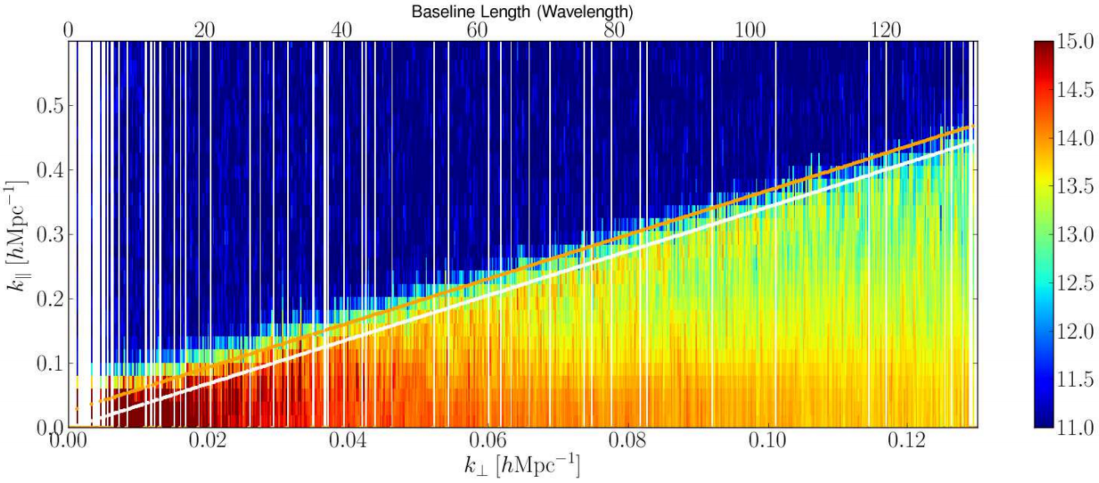

FIGURE 2.3: Individual power spectra from each baseline of the array yields a 2D power spectra, the foreground emission occupies a wedge leaving a window at higher $k_{||}$ values for 21 cm EoR studies (Pober et al., 2013). The white line marks the horizon limit of each baseline and the orange line is 50 ns beyond.

The chromaticism in the baseline response of an interferometer confines the foreground into a "wedge" shaped region in the 2D $(k_\perp, k_{||})$ plane, with shorter baselines (i.e. at low $k_\perp$ values) contributing more $k_{||}$ modes free from foreground contamination. This behaviour is revealed in actual observations by Pober et al. (2013), shown in Figure 2.3. The white line in Figure 2.3 marks the "horizon limit" which is the $k_{||}$ mode on a given baseline that corresponds to its chromatic response to a flat-spectrum source located at the horizon. The emission at $k_{||}$ values greater than the horizon limit extends the wedge beyond the horizon limit, thus, describing a "supra-horizon" emission which does not have a constant width in $k_{||}$ as a function of $k_\perp$ (Pober et al., 2013). It is assumed that the power spectrum of 21 cm HI emission can be recovered from a limit down to $k_{||}$ modes bound by the Full Width at Half Maximum (FWHM) of the instrument's primary beam response, and this extension of the foreground wedge to FWHM of primary beam is represented by "Primary Beam FWHM Wedge" in Figure 2.2. And in order to be certain that the EoR window is foreground free, we consider a small buffer beyond the horizon.

This approach helps us work in a region free from foreground contamination, however, complications such as scattering of power from the wedge into the EoR window has been identified. The EoR signals outside the wedge gets corrupted while combining redundant visibilities without image plane correction as demonstrated by Moore et al. (2013). Therefore, it is important to check the efficiency of foreground avoidance approach with respect to foreground removal method.

2.2.3 Foreground removal vs. foreground avoidance

Although foreground removal seems, in principle, a more effective strategy, it is, at present, unclear which strategy will ultimately be the winning one. The best upper limits to date have been achieved using the avoidance scheme applied to the analysis of PAPER data taken in a highly redundant configuration (Ali et al., 2015; Parsons et al., 2014). It is, however, likely that some form of foreground subtraction is required if future experiments like the Square Kilometre Array (SKA[1]) aim to image the ionized bubbles throughout reionization at 5 arcminute resolution (Koopmans et al., 2015; Mellema et al., 2015).

In the light of this scenario, minimizing calibration imperfections is crucial to prevent power from being spread into the EoR window and validating the basic assumption of foreground subtraction algorithms - i.e. frequency smoothness - as much as possible. The aim of this thesis is indeed to help the calibration by deriving an accurate catalogue

---

[1] https://www.skatelescope.org/

of compact sources at relatively low angular resolution that can be used as a global (i.e. covering a large fraction of the southern sky) sky model. Such sky model is necessary for absolute flux density calibration (see Jacobs et al., 2011) as well as ionospheric and primary beam calibration (i.e. Mitchell et al., 2008). If direction dependent calibration techniques are necessary (i.e. Yatawatta et al., 2013), an accurate global sky model becomes indispensable.

Chapter 3

Observations and data analysis

3.1 Basics of radio interferometry

Radio interferometry is a well established technique where individual telescopes are connected in order to achieve an angular resolution equivalent to the longest separation between the two furthermost antennas. The simplest form of radio interferometer is formed by connecting two elements (two-element interferometer, Figure 3.1). I will describe the principles of the two-element interferometer to illustrate the basics of radio interferometry.

Let us begin with considering a plane wave emitted by a celestial source along the direction $\hat{s}$. Such wave will reach the antenna i with a certain time delay τ_g with respect to antenna j due to the extra path length between the two antennas. Such delay is called *geometrical* delay and can be expressed as:

$$\tau_g = \frac{\vec{b} \cdot \hat{s}}{c} \tag{3.1}$$

where $\vec{b}$ is the baseline vector that describes the separation between antenna i and j and c is the speed of light. The output voltages of each individual antennas are directed to a correlator, that performs the cross-multiplication and time average of the inputs for each antenna pair.

The correlator output is the actual data measured by the interferometer and is called *visibility*, V, and is directly related to the sky brightness, I, by the van Cittert-Zernike theorem (Thompson, Moran & Swenson, Jr., 1986)

$$V_{ij}(u,v) = \int_{\Omega} A(l,m)\ I(l,m)\ e^{-2i\pi(ul+vm)} dl\ dm \tag{3.2}$$

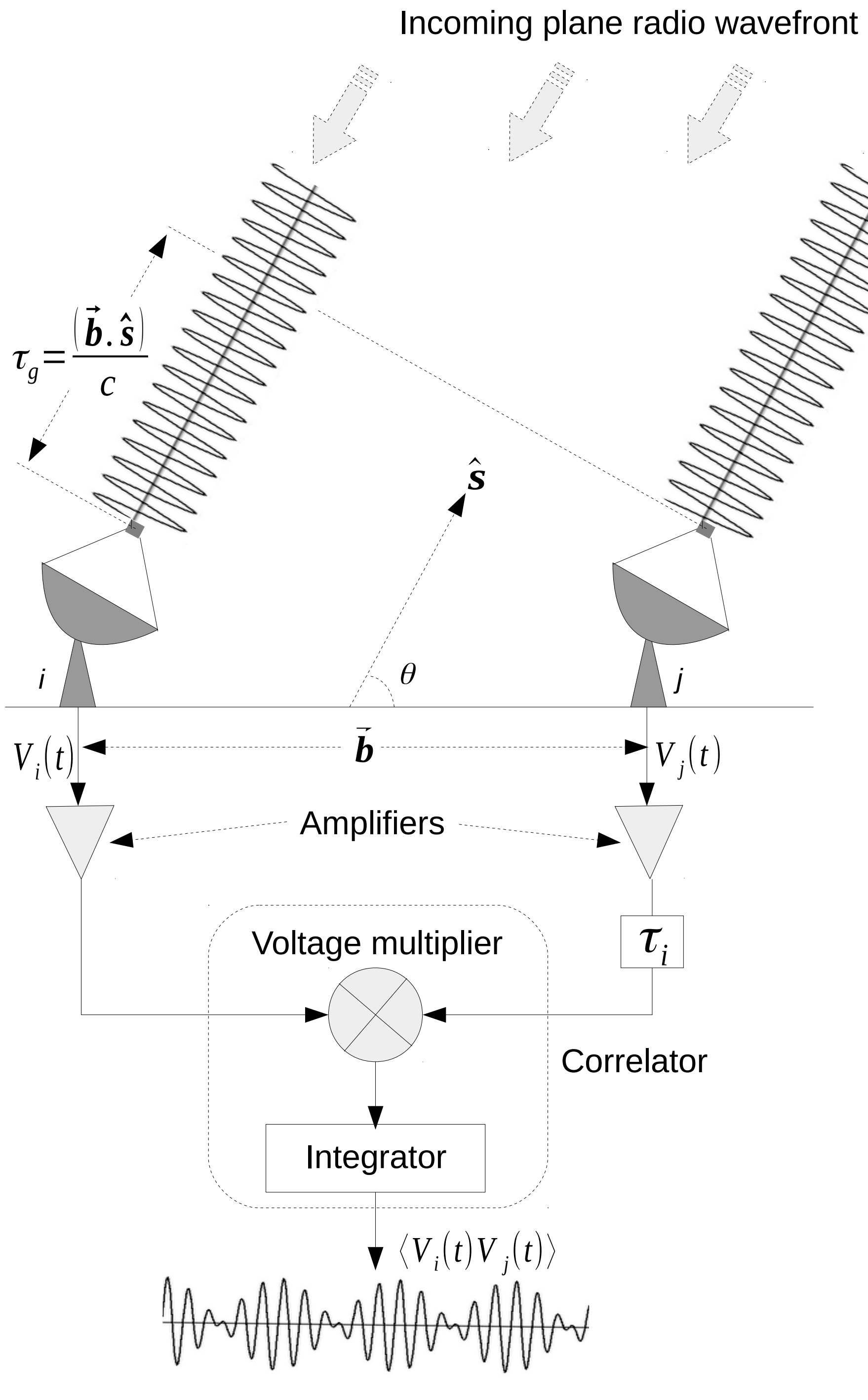

FIGURE 3.1: A schematic of a two-element radio interferometer, where i and j are the antenna positions. A delay τ_i is often introduced to compensate the geometrical delay (τ_g) and track the source as it moves across the sky. The correlator multiplies and integrates the input voltages, producing output visibilities.

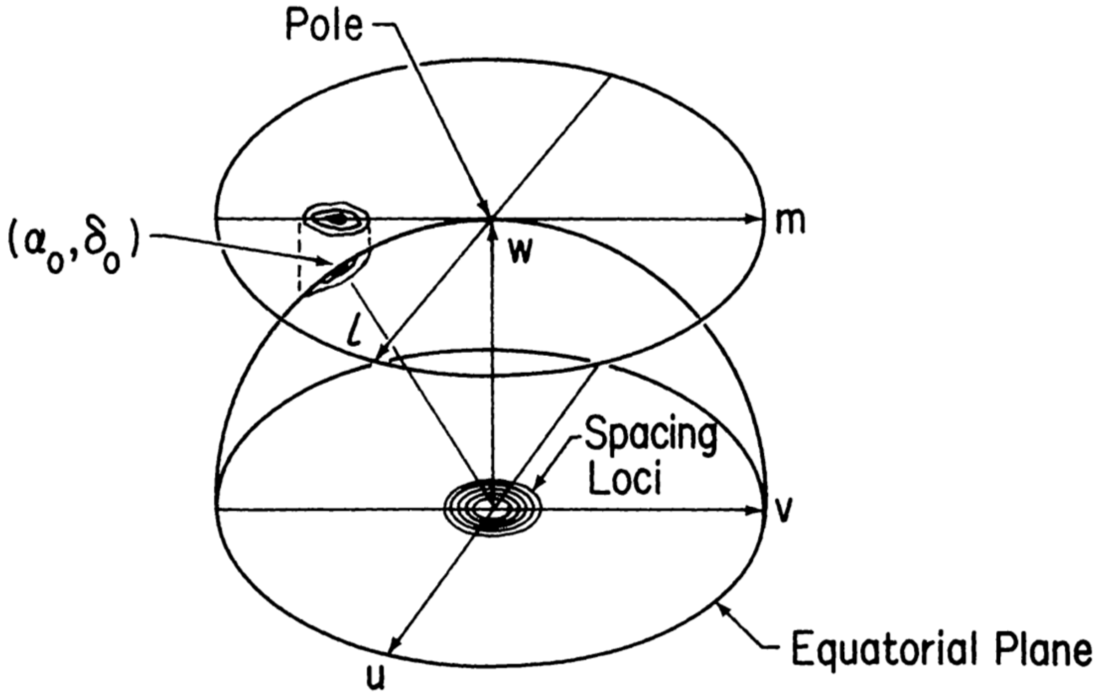

FIGURE 3.2: Schematic illustrating the reference frame the defines the direction cosines (l, m) in Equation 3.2. The source is located at the Equatorial coordinates (α_0,δ_0). The direction of the w-axis is here chosen to be that of the pole ($\delta = 90°$) (from Thompson, Moran & Swenson, Jr., 1986).

where (u, v) are the coordinates of the antenna pair (i, j), Ω is the source area, A is the primary beam response of the antennas and (l, m) are coordinates defined in the reference system illustrated in Figure 3.2.

Equation 3.2 describes a two dimensional, spatial Fourier transform between the source brightness and the measured visibilities and form the basis of the reconstruction of the intrinsic sky brightness. If the Fourier transform of the source brightness is measured at many (u, v), points then Equation 3.2 can be Fourier inverted to obtain an estimate of the sky brightness I. The process of measuring many (u, v) points is often referred as to sampling the uv plane and is normally obtained by Earth rotation. The process of obtaining interferometric images by filling the uv plane through Earth's rotation is called synthesis imaging and is normally used in modern radio interferometry.

3.2 Calibration

Visibilities measured by an interferometer are usually corrupted by effects that occur along the signal path, either due to the instrumental response or the ionosphere/atmosphere. The process that corrects for such corruptions is named calibration and is described in terms of the Radio Interferometric Measurement Equation (RIME, Hamaker et al., 1996; Smirnov, 2011a). In the RIME formalism, instrumental corruptions are described by antenna-based, 2 × 2 complex matrices **J** (Jones matrices):

$$\mathbf{V}_{ij} = \mathbf{J}_i \left[\int_{\Omega} \mathbf{B}_{ij} \; e^{-2i\pi(ul+vm)} dl \; dm \right] \mathbf{J}_j^H \tag{3.3}$$

where the visibility **V** is now a 2 × 2 complex matrix that includes all the polarization p, q products:

$$\mathbf{V}_{ij} = \begin{bmatrix} V_{ij}^{pp} & V_{ij}^{pq} \\ V_{ij}^{qp} & V_{ij}^{qq} \end{bmatrix}, \tag{3.4}$$

where H is the Hermitian conjugate operator.
The 2 × 2 complex matrix **B** describes a model for the sky brightness distribution generally indicated as:

$$\mathbf{B} = \begin{bmatrix} I+Q & U+iV \\ U-iV & I-Q \end{bmatrix}, \tag{3.5}$$

where I, Q, U and V are the usual Stokes parameters (Sault et al., 1996) that describe the polarization state of an electromagnetic wave. Throughout the present thesis we will assume only unpolarized (i.e. $Q = U = V = 0$) sky models.
As **B** is assumed to be known, the Jones matrices can be determined via a non-linear fit of the visibility data to the model. Once the Jones matrices are calculated, corrected visibilities $\tilde{\mathbf{V}}$ can be formed as:

$$\tilde{\mathbf{V}}_{ij} = \mathbf{J}_i^{-1} \mathbf{V}_{ij} \mathbf{J}_j^{H^{-1}}. \tag{3.6}$$

3.3 The Precision Array to Probe the Epoch of Reionization

The Precision Array to Probe the Epoch of Reionization (PAPER) is an interferometric array of dual polarization dipole elements operating within 100–200 MHz band (Parsons et al., 2010). A PAPER element (Figure 3.3) has crossed dipoles inserted between two steel discs that act as sleeves to broaden the frequency response by creating a dual-resonance structure. The trough reflectors limit sensitivity at low elevations without introducing nulls (Jacobs, 2011). A balun is directly attached to the antenna which provides a gain of 60 dB before the unbalanced signal is transmitted via coaxial cable to a central RFI tight central processing location. A PAPER 32-dipole array was initially deployed at the NRAO site near Green Bank, West Virginia, followed by a staged

Table 3.1: Summary of the observational setup

Array longitude	21:25:41.9
Array latitude	-30:43:17.5
Number of Dipoles	32
Frequency range	100 - 200 MHz
Total number of channels	2048
Angular resolution	16'× cosec(δ)
Right ascension	$0^{\mathrm{h}} < \alpha < 8^{\mathrm{h}}$ and $23^{\mathrm{h}} < \alpha < 24^{\mathrm{h}}$
Declination	$\delta = -30°43'17.5''$
Observed on	15^{th} September 2011 from 2:04 hrs to 06:44 hrs
Method	Drift scan

deployment in the radio quiet SKA-SA reserve in the Karoo desert near Carnarvon in South Africa (Jacobs et al., 2013; Parsons et al., 2014). A 32, 64 and 128-dipole arrays were deployed in the Karoo leading to improved constraints on the 21 cm power spectrum from the EoR (Ali et al., 2015; Jacobs et al., 2015; Pober et al., 2013).

The 32-dipole PAPER array in the Karoo (PSA32 hereafter) was deployed in two different layouts: a redundant configuration for 21 cm line power spectrum analysis (Parsons et al., 2014) and an imaging configuration with antennas distributed pseudo-randomly within a $\sim$ 350 m diameter circle. (Figure 3.4). A $\sim$ 4 hour integration taken during night time in the imaging configuration was used in the present thesis (see Table 3.1 for details of the observations).

3.4 Initial calibration and data compression

After correlation, an initial calibration was applied to the visibility data in order to correct for cable lengths. Time variations in the dipole gains were corrected by extrapolating system temperature variation measurements carried out in the lab (Parsons et al., 2014).

Due to the pristine quality of radio frequency interference (RFI) environment at the Karoo site, RFI flagging was limited to channels that were known to be affected by satellite transmission, and any visibility with amplitudes 2σ above the mean amplitude, where σ is the standard deviation of the distribution. Data were then compressed in both time and frequency to reduce their volume. Compression was performed by applying a delay-delay-rate filter (Parsons & Backer, 2009) that preserves the coherency of the emission down to the horizon for a 350 m baseline. The final data set has an integration time of 43 seconds and a frequency resolution of 490 kHz.

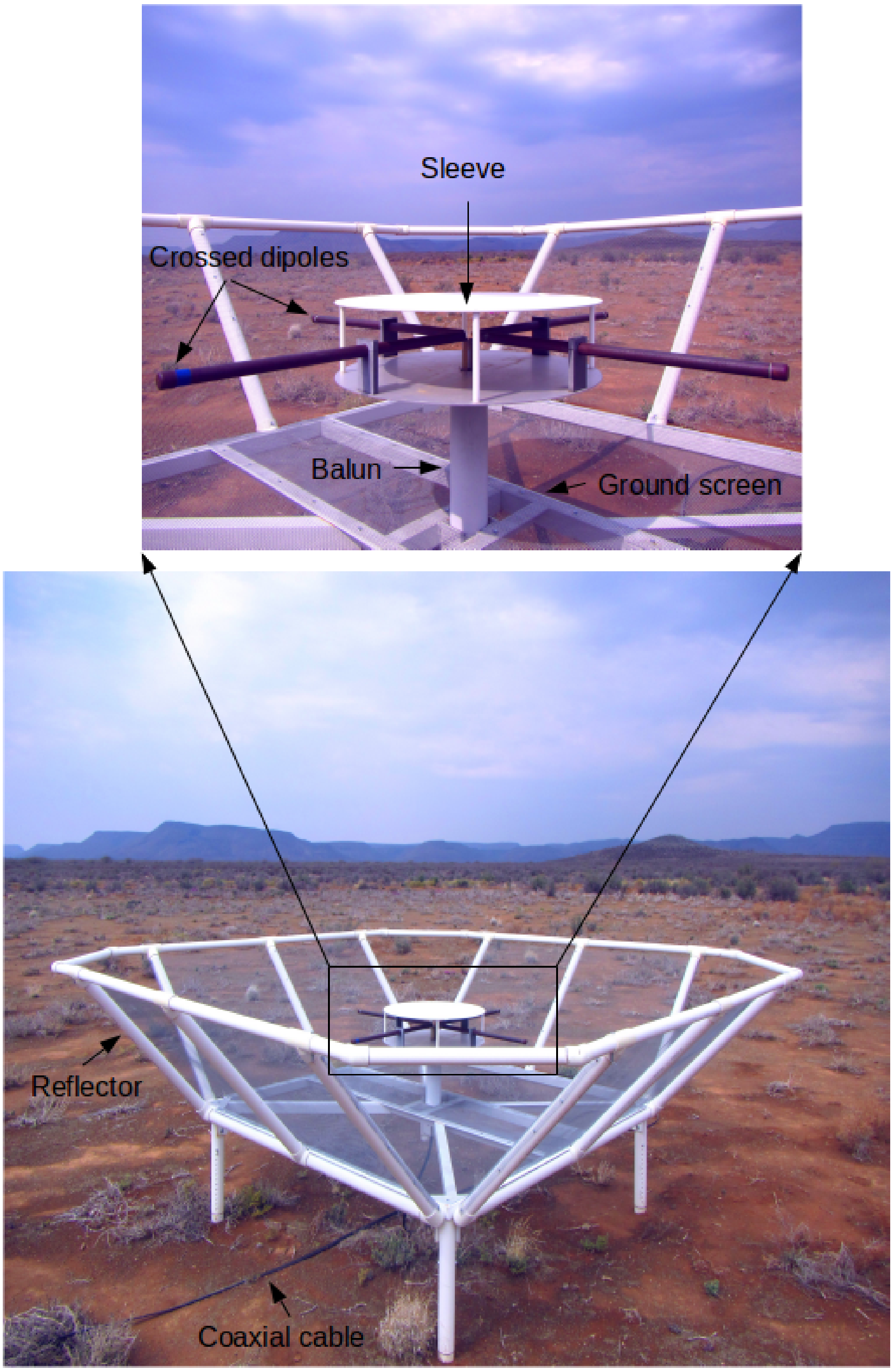

FIGURE 3.3: A PAPER antenna (bottom panel) with a zoom into the central area, showing PAPER crossed dipole with steel sleeves (top panel).

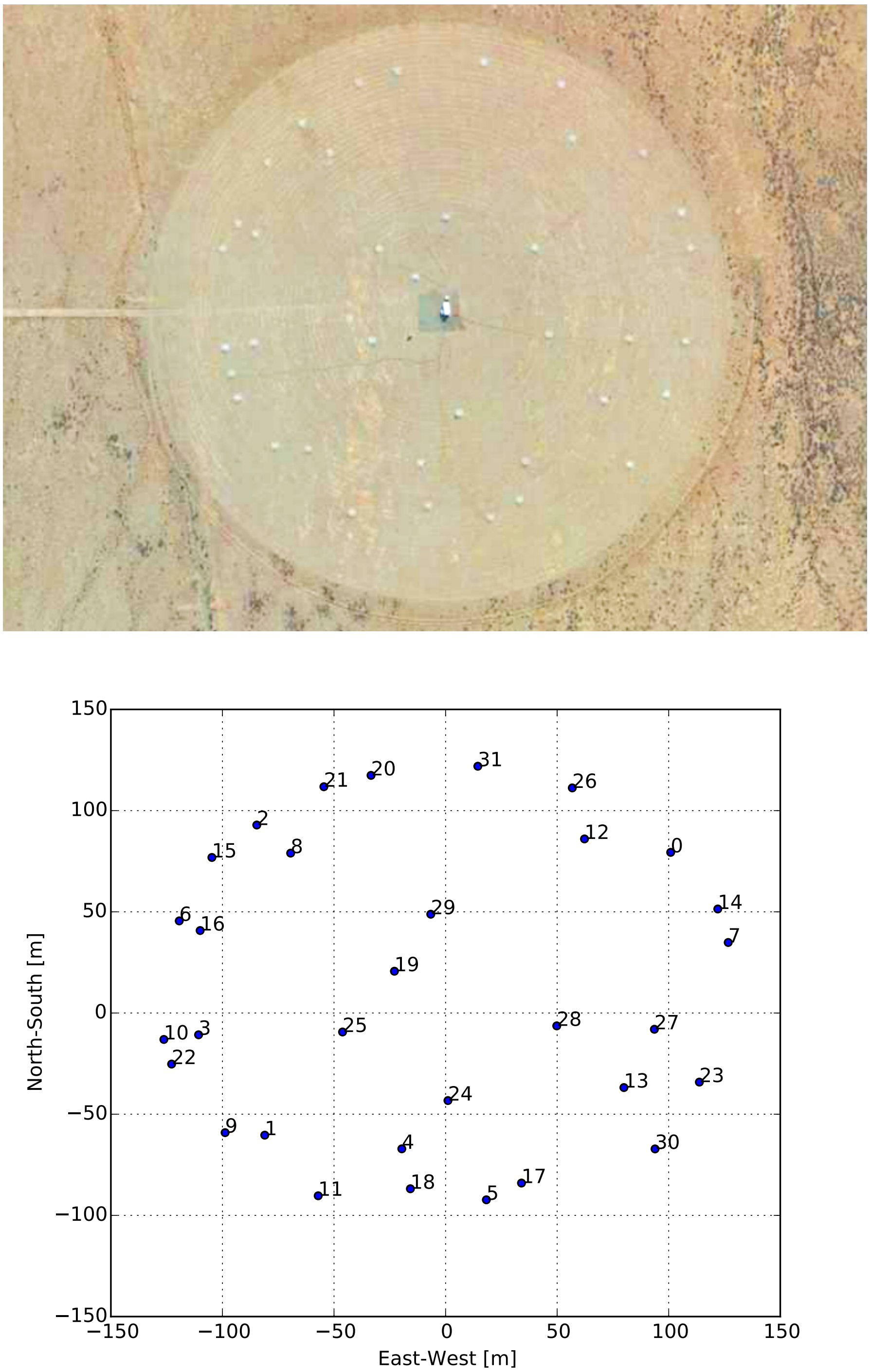

FIGURE 3.4: Aerial view of PSA32 (top panel, from Jacobs, 2011) and its antenna distribution (bottom panel).

3.5 Snapshot images

Data were recorded to disk into a single file every 10 minutes and we will refer to such data as a snapshot throughout the thesis. As the PAPER primary beam is very broad (Figure 3.5), it can be assumed to be constant across each snapshot. As the PAPER correlator does not fringe track, we rotated the visibilities within each 10 minute file to its middle time. The data analysis was carried out using the Common Astronomy Software Applications package (CASA[1]), complemented by scripts to perform some of the dedicated tasks described below.

Visibilities for each snapshot were Fourier transformed into individual images with a ∼ 51.2° field of view. Uniform weights were applied in order to minimize the sidelobe contribution across the whole field of view. The multi-frequency synthesis algorithm (Conway & Sault, 1995; Junklewitz et al., 2014) was used in order to provide a better uv coverage by taking advantage of the wide bandwidth (Figure 3.6). Only the bandwidth between 120 and 180 MHz was used as the filter response rolls off fairly sharp beyond those edges. The resulting image frequency was, therefore, 149.75 MHz.

When the field of view is large, as in our case, Equation 3.2 only approximately describes the relationship between the sky brightness and the measured visibilities. The three dimensional nature of the sky emission should be accounted for by obtaining a relationship between the 2D sky intensity and the 3D coherence function by rewriting Equation 3.2 as a 3D Fourier transform with w-axis to lie in the direction of the celestial pole (refer Figure 3.2) and n is an independent variable which defines the direction cosine for w (Cornwell & Perley, 1992):

$$V_{ij}(u,v,w) = \int_{\Omega} A(l,m)\ I(l,m)\ e^{-2i\pi(ul+vm+wn)} dl\ dm\ dn \tag{3.7}$$

Instantaneous non-coplanarity of the array was corrected using the w-projection algorithm (Cornwell & Bhatnagar, 2005) by setting the number of $w-$terms to 32. Each dirty image was deconvolved using the Cotton-Schwab algorithm until a threshold of 5 Jy was reached.

Figures 3.7 and 3.8 shows four examples of deconvolved snapshot images. It can be seen that the majority of the emission comes from point-like sources, with the exception of Fornax A, a double-lobed radio galaxy that extends over ∼ 2° (Bernardi et al., 2013; Geldzahler & Fomalont, 1984). The well known Pictor A radio galaxy (Perley, Roser & Meisenheimer, 1997) is unresolved at our resolution.

---

[1] `http://casa.nrao.edu/`

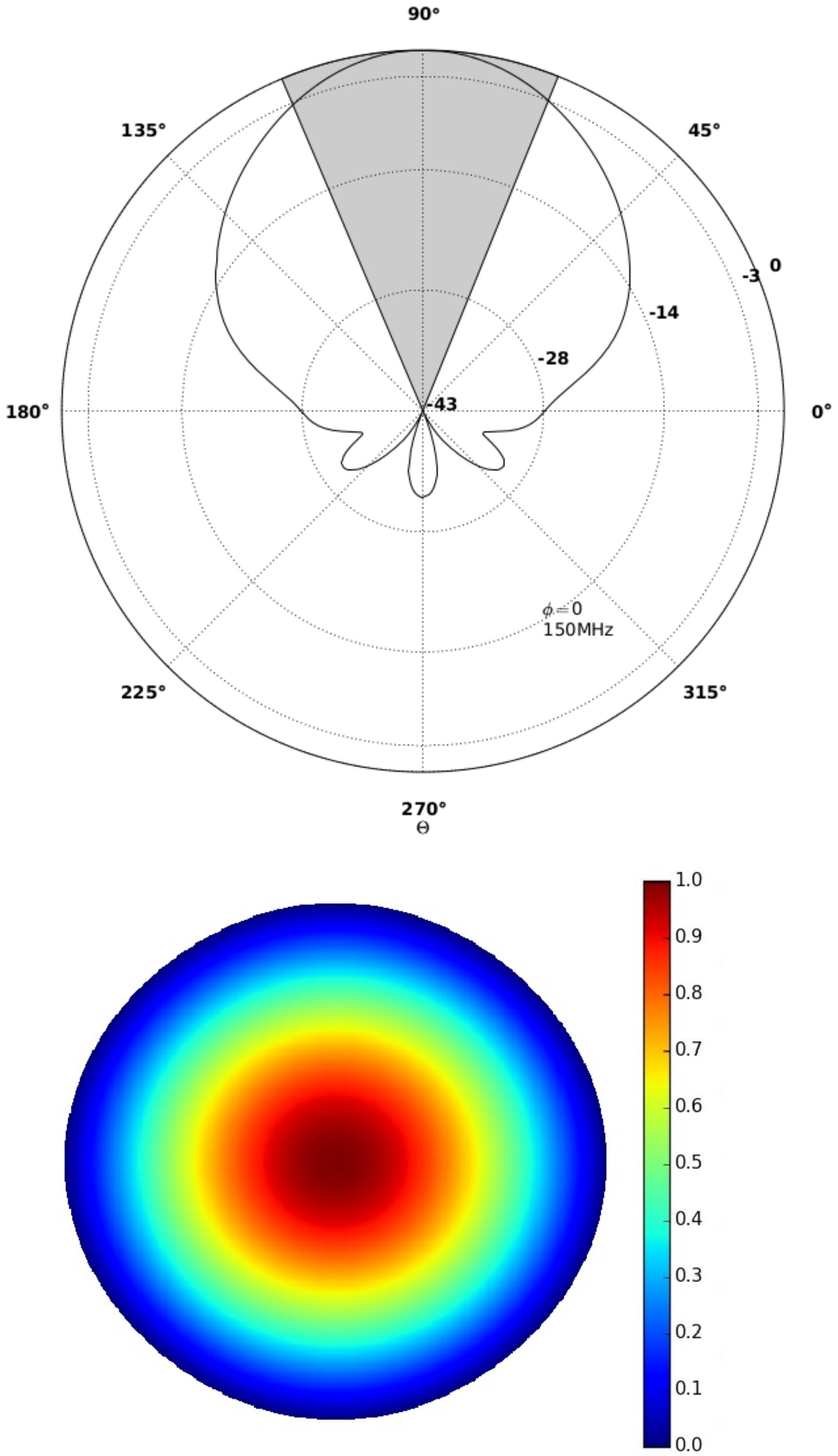

Figure 3.5: Top: Orthogonal view of the simulated PAPER dipole beam pattern (from Jacobs, 2011). The grey region represents the 45° Half Power Beam Width (HPBW). Bottom: Top view of the simulated PAPER primary beam at 150 MHz.

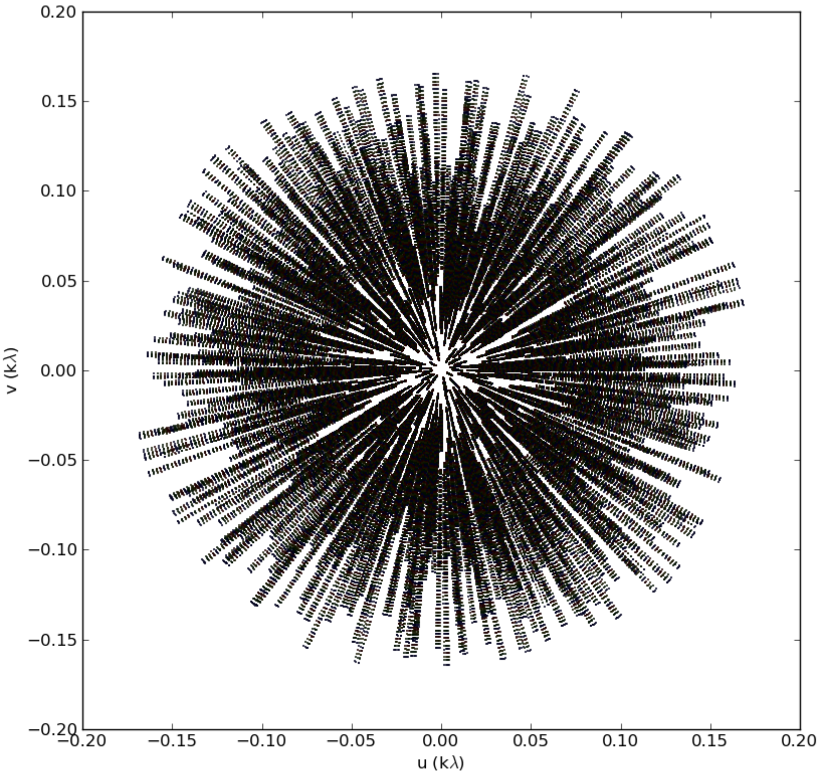

FIGURE 3.6: *uv* coverage of PSA32 for one of the snapshots. The radial spiky pattern is due to the very large instantaneous bandwidth.

A peculiar feature of both images (and common to any snapshot image actually) is the presence of a spiky error pattern around both Fornax A and Pictor A and spreading across most of the image. Such errors are at the level of ~ 5 Jy beam^{-1}, limiting a clean detection of the faintest sources. In the next Sections we show what the source of such errors is and how we corrected them.

3.6 Self-calibration

Self-calibration is a fairly established technique that uses the observed sky brightness as a model to correct time and/or frequency variations of the telescope gains (Cornwell & Fomalont, 1999). Self-calibration is generally an iterative process that involves the following steps:

- obtaining an initial estimate of the sky model - either derived from deconvolution or from an external source catalogue;
- using such sky model to predict visibilities and solve equation 3.3 in order to derive the instrument Jones matrices at a higher time and/or frequency cadence;

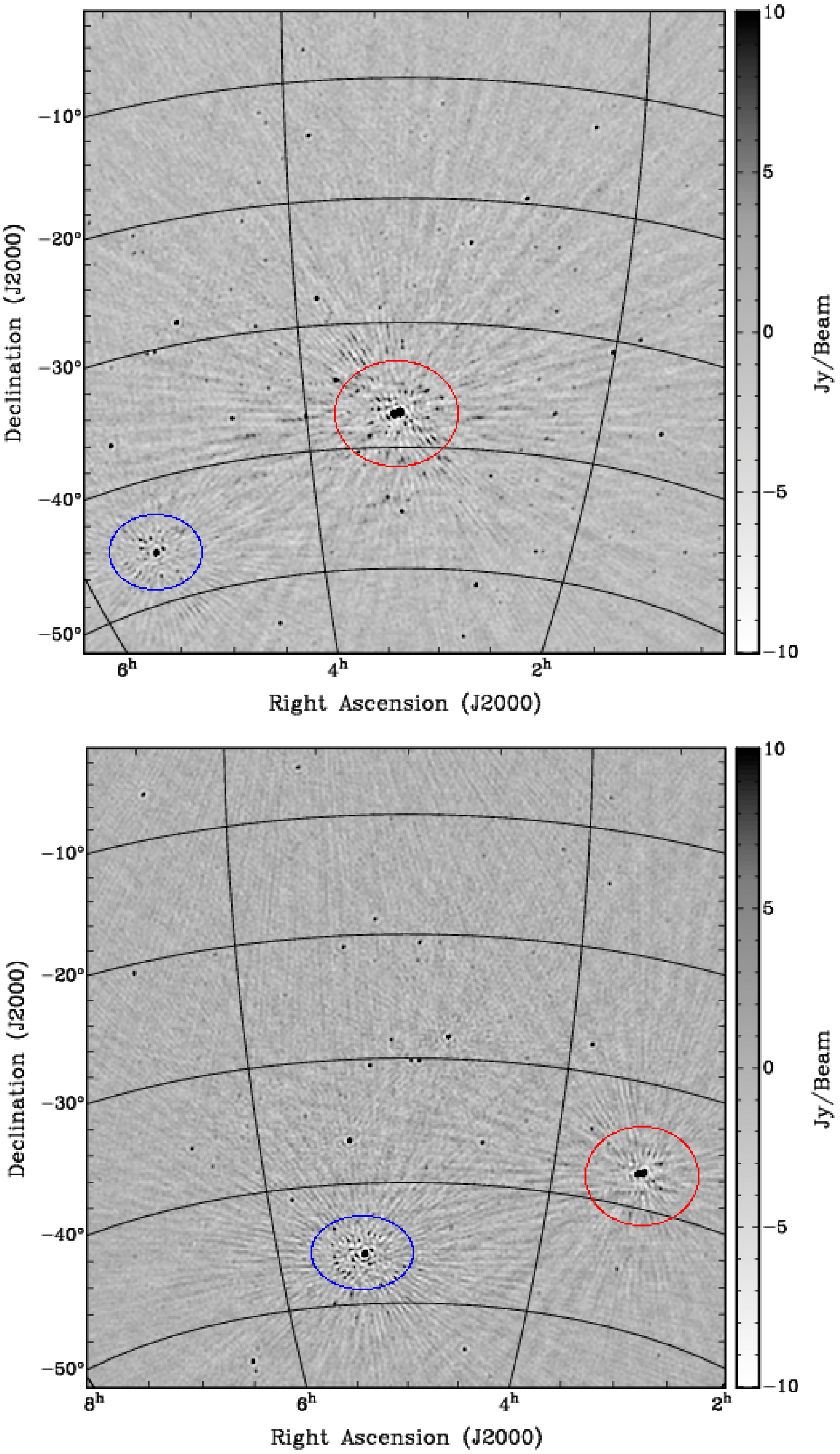

Figure 3.7: Example of two snapshot images by PSA32 with phase-center at LSTs 3.3 hours (top) and 5 hours (bottom) respectively. Spiky patterns are seen around bright sources like Pictor A (blue) and Fornax A (red).

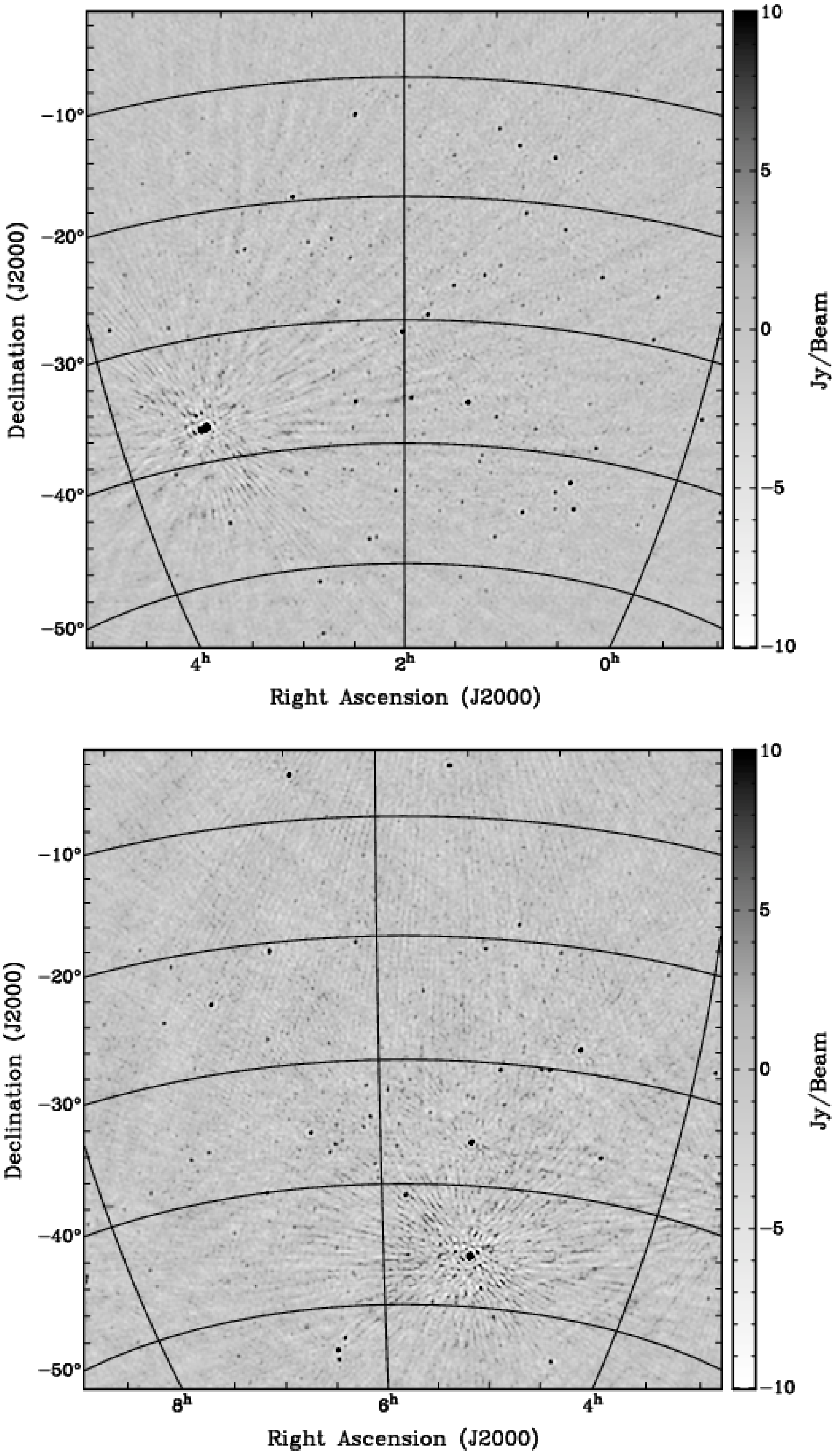

FIGURE 3.8: Same as the top panel of Figure 3.7 but for LST ∼ 2 hours (top) and ∼ 6 hours (bottom) respectively.

- correcting visibilities by using the updated gains and then Fourier transforming them into images;
- deriving an improved sky model by deconvolving the newly calibrated images.

The aforementioned steps are repeated until convergence is reached or, more empirically, until no further improvement in the sky model and/or the instrument gains are achieved. If the sky model is carefully derived, self-calibration is a very powerful tool to achieve high dynamic range images (Pearson & Readhead, 1984).

We self-calibrated each individual PSA32 snapshot by using the sky model obtained from the initial CLEAN deconvolution (see Section 3.5). We then solved for time–independent phases for each frequency channel. Although most of the solutions are essentially flat across the bandwidth, some of them show a slope as a function of frequency (Figure 3.9), indicating that the cable length correction may be inaccurate for some dipoles. Figure 3.10 shows that some of the error patterns seen in the images are corrected after self-calibration, in particular the errors associated with the transiting source (either Pictor A or Fornax A). Self-calibration does not, however, calibrate well Pictor A or Fornax A when they are away from transit, indicating that further, direction dependent errors are present.

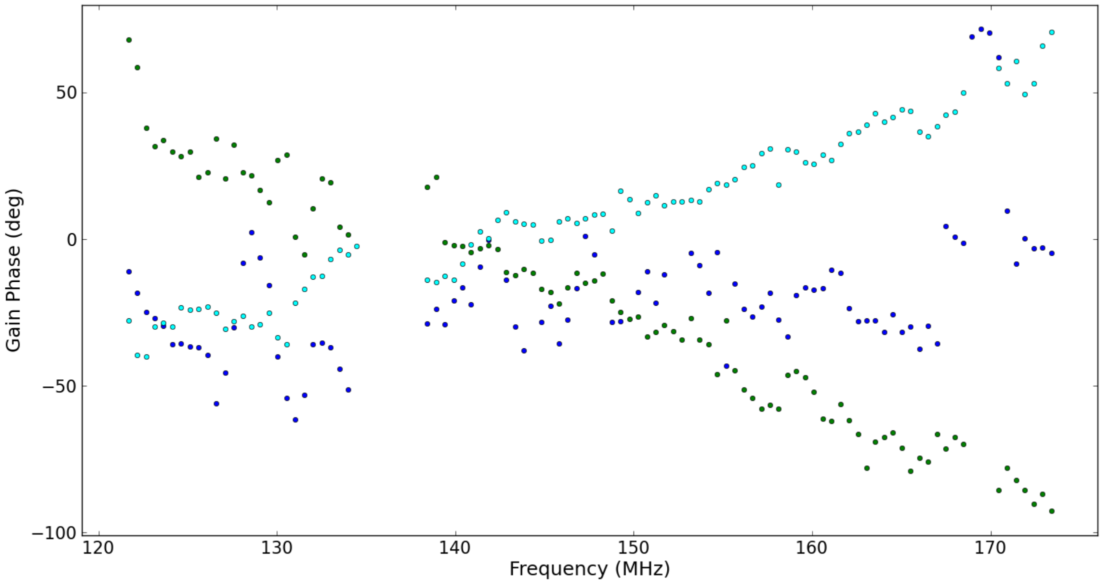

FIGURE 3.9: Phase solutions as a function of frequency for three dipoles that likely have a wrong cable correction, leading to the frequency phase slopes.

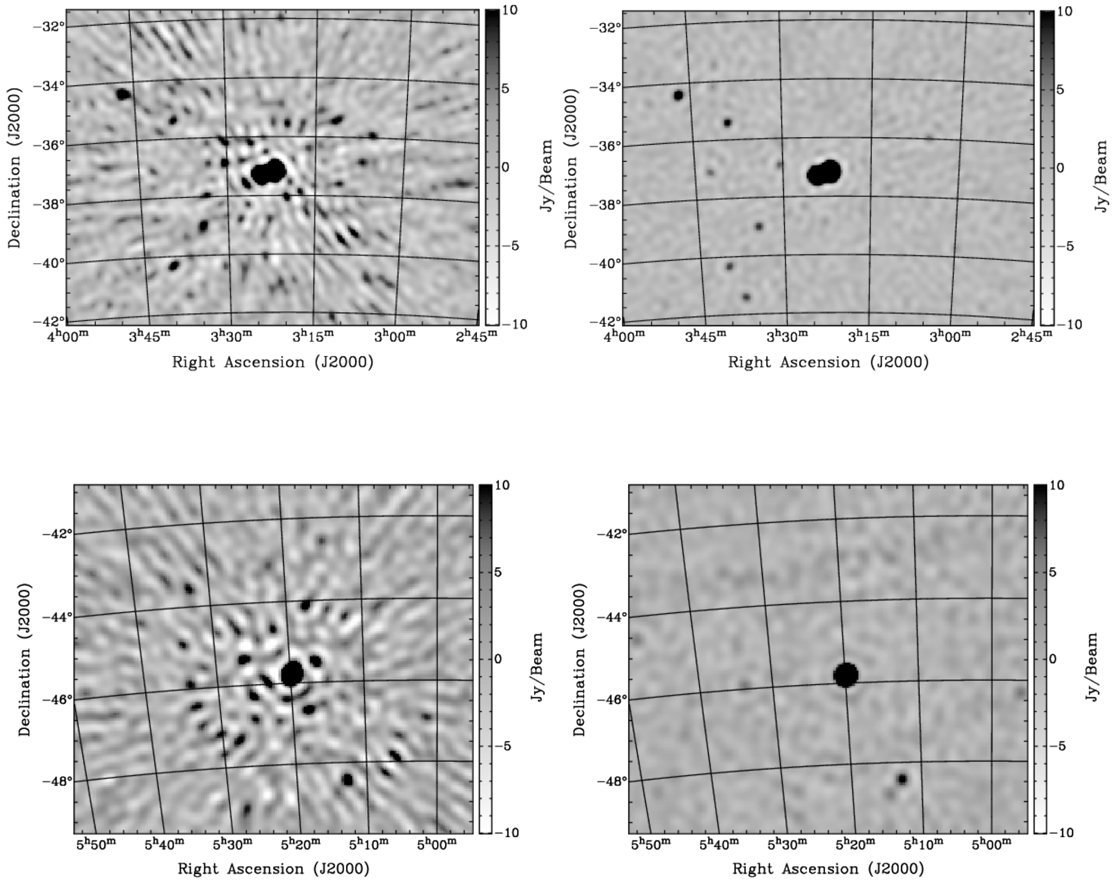

FIGURE 3.10: Zoomed-in images before (left) and after (right) the frequency dependent phase correction. Fornax A and Pictor A are the source at transit in the top and bottom panels respectively.

3.7 Direction dependent calibration

In widefield imaging, a single calibration solution does not often suffice to correct for effects across the field of view. When the effects that corrupt the signal path are different for different lines of sight, they are often named *direction dependent* effects. At low frequencies the ionosphere is the most common source of direction dependent corruptions as its turbulence introduces an additional time-variable phase error to the incoming signal (Intema et al., 2009; Loi et al., 2015; Noordam, 2004). Different lines of sight may, therefore, experience different phase errors. Time and frequency variable primary beams may also cause direction dependent errors. As PAPER is not electronically steered, its primary beams are very stable with time and frequency, therefore this effect is expected to play a minor role in our data.

Direction dependent calibration has become a more and more routinely requirement for the calibration of low frequency interferometric observations (Intema et al., 2009;

Mitchell et al., 2008) and the pursuit of high dynamic range imaging (Bernardi et al., 2010; Smirnov, 2011b). Direction dependent calibration can be performed in several ways, although we used here the approach called *peeling* as described in Mitchell et al. (2008). Peeling involves the following steps:

- a model is derived for each source s to be peeled;
- a model r is derived for the remaining sky brightness;
- in order to peel source s_i, a sky model $r + \sum_{j \neq i}^{N} s_j$ is created, where N is the number of sources to be peeled. The visibilities predicted from such sky model are subtracted from the data $\mathbf{V}$;
- the Jones matrices for source s_i is derived by solving the RIME (equation 3.3) for that source;
- corrupted visibilities $\tilde{\mathbf{V}}_i$ are generated by applying the derived solutions to the model visibilities for the source s_i;
- the source s_i and its corruptions are removed from the data forming residual visibilities $\mathbf{V}_r = \mathbf{V} - \tilde{\mathbf{V}}_i$.

The above procedure can be iterated over the number of sources to be peeled. As it can be seen from the top panels of Figures 3.12 and 3.13, only the source away from transit needs a correction for direction dependent effects. We therefore implemented the aforementioned peeling scheme with $N = 1$ number of sources to be peeled for each snapshot. Models for Pictor A and Fornax A were both derived from the CLEAN deconvolution with a 5 Jy threshold. We only solved for time and frequency independent dipole phases in the direction of the source to be peeled or, in other words, we only derived one antenna phase solution per snapshot.

The bottom panels of Figures 3.12 and 3.13 show the effectiveness of peeling in removing the direction dependent errors. It is interesting to note that a simple phase correction is sufficient to calibrate direction dependent effects, suggesting that errors may indeed be due to ionospheric fluctuations across the field of view.

3.8 Absolute flux density calibration

The initial gain calibration did not tie the visibility amplitude to an absolute flux scale, therefore the last step of the data reduction was the absolute calibration of the image snapshots.

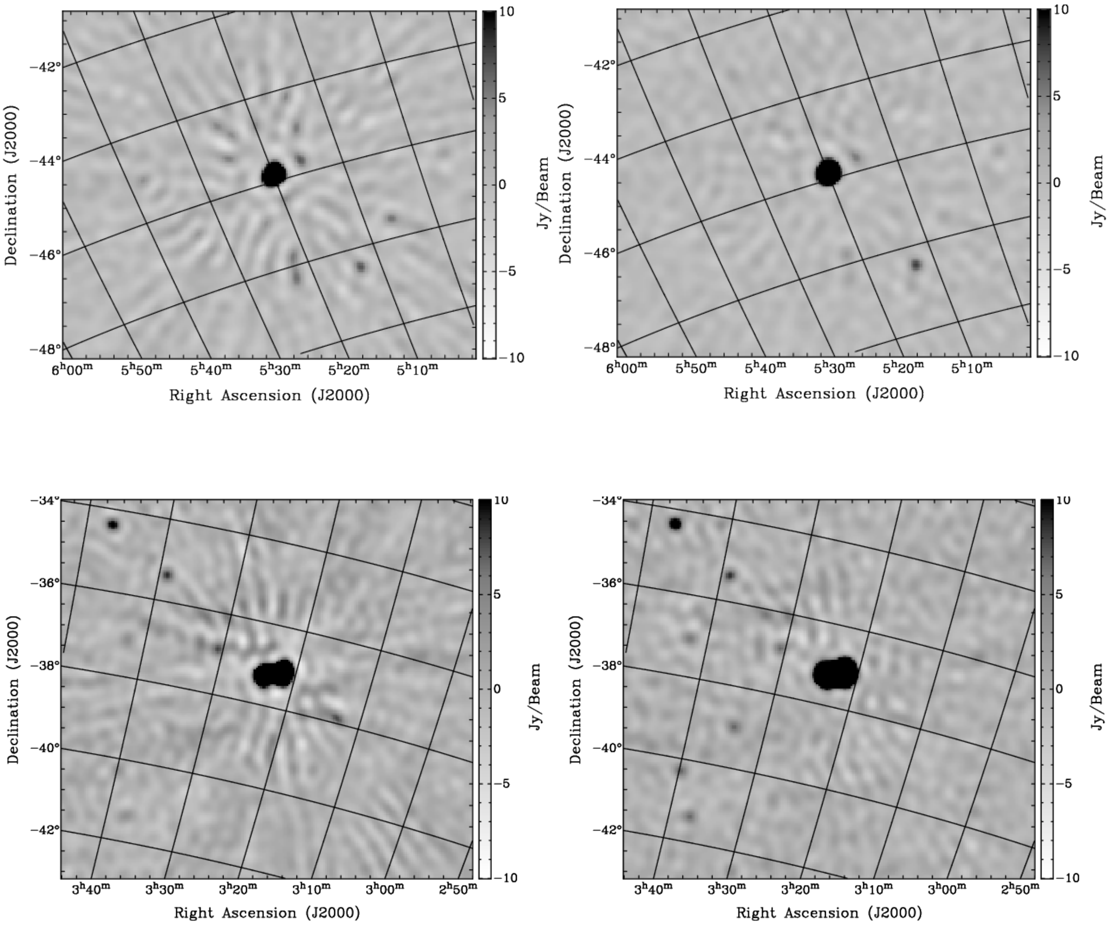

Figure 3.11: Zoomed-in images before (left) and after (right) direction dependent phase correction. Pictor A and Fornax A are the sources away from transit in the top and bottom panels respectively.

Standard interferometric flux calibration uses observations of a well known, isolated, non variable, point-like source such as 3C48, 3C138, and 3C147 (i.e. Perley & Butler, 2012) to set the absolute flux density scale. PSA32 is, however, such a compact array and its primary beam is so wide that the assumption of a single, known, isolated point source that dominates the visibility data is no longer valid, as tens of discrete sources as well as Galactic diffuse radiation contribute to the observed emission. Rather than attempting an antenna based absolute calibration that would require a complicated and uncertain sky model, we directly correct the snapshot images after direction dependent calibration is applied. We used Pictor A to set the absolute flux density scale according to the Jacobs et al. (2013) model:

$$F_\nu^m = A_{\nu_0} \left(\frac{\nu}{\nu_0} \right)^{-\beta} \tag{3.8}$$

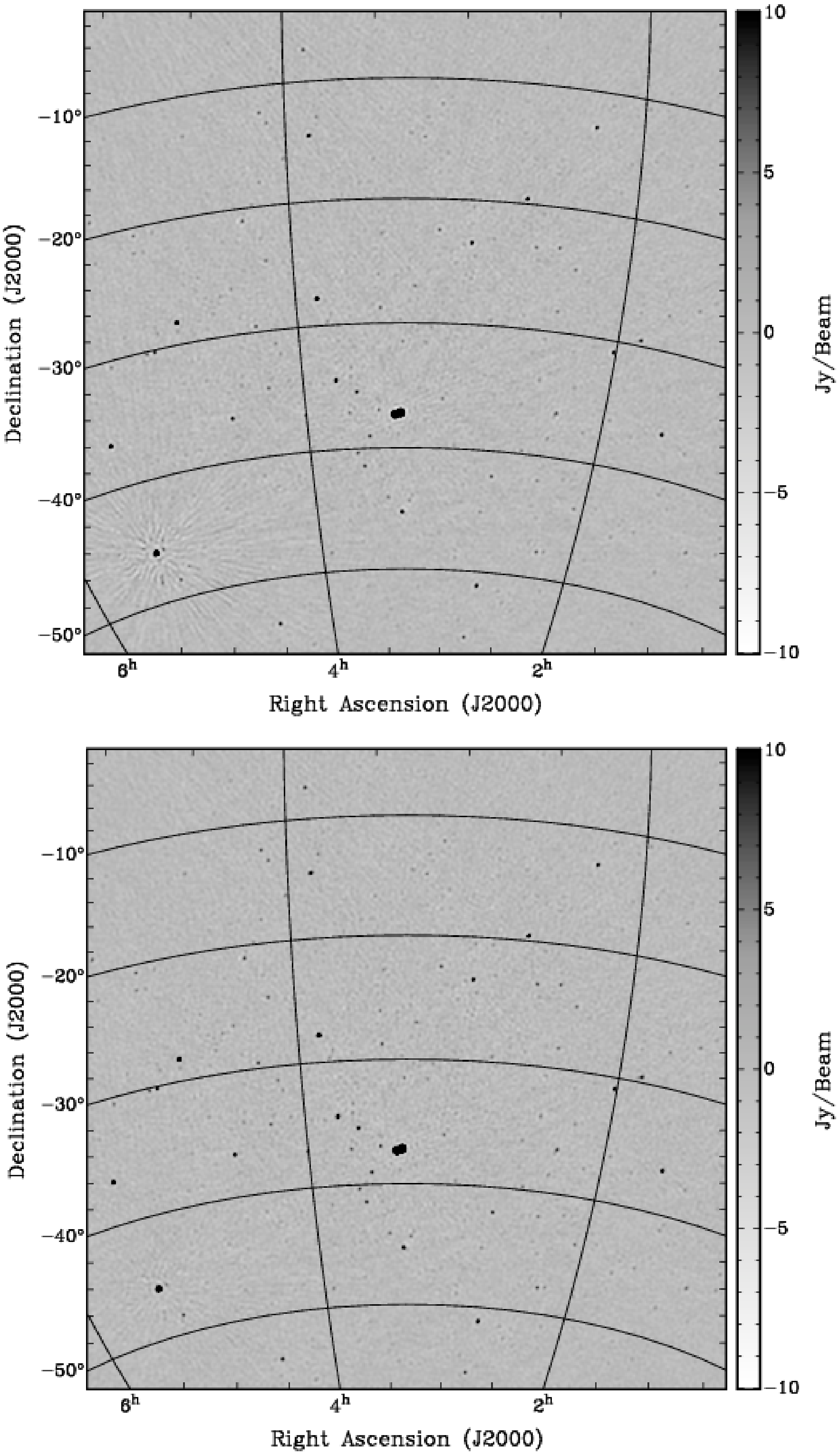

FIGURE 3.12: Same as Figure 3.7 but before (top) and after (bottom) direction dependent calibration towards Pictor A. The error patterns around Fornax A are corrected after solving for direction independent calibration.

where F^m_ν is the predicted flux density, $A_{\nu_0} = 382$ Jy is the source flux density at $\nu_0 = 150$ MHz and $\beta = 0.76$ is the spectral index in the $100 - 200$ MHz range.

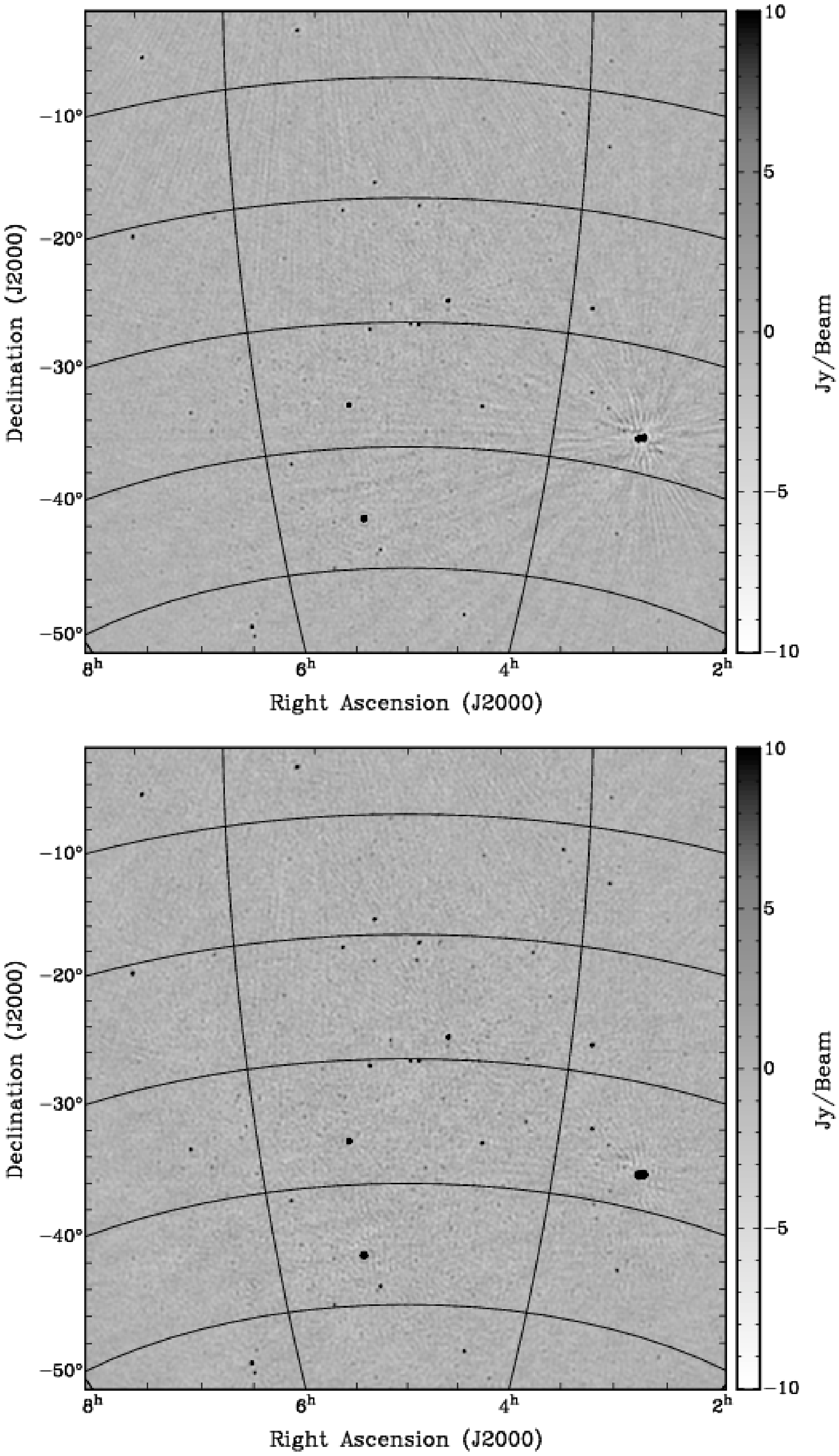

FIGURE 3.13: Same as Figure 3.7 but before (top) and after (bottom) direction dependent calibration towards Fornax A. The error patterns around Pictor A are corrected after solving for direction independent calibration. The top panel also shows sidelobes from Taurus A (outside the field of view) that were removed by just subtracting a model of the source from the visibility data.

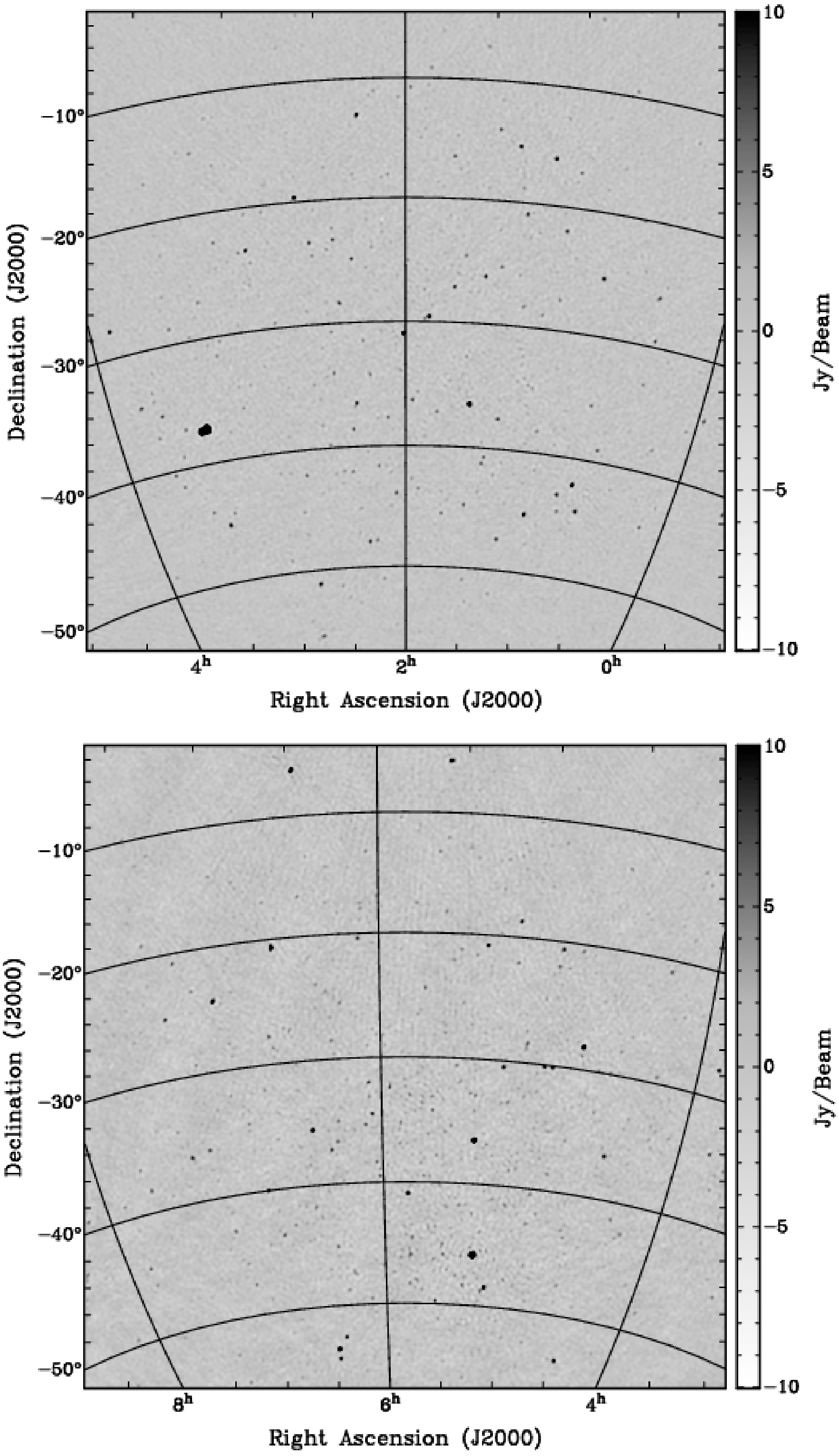

FIGURE 3.14: Same as the bottom panel of Figure 3.13, for snapshots at LSTs ∼ 2 and ∼ 6 hours respectively.

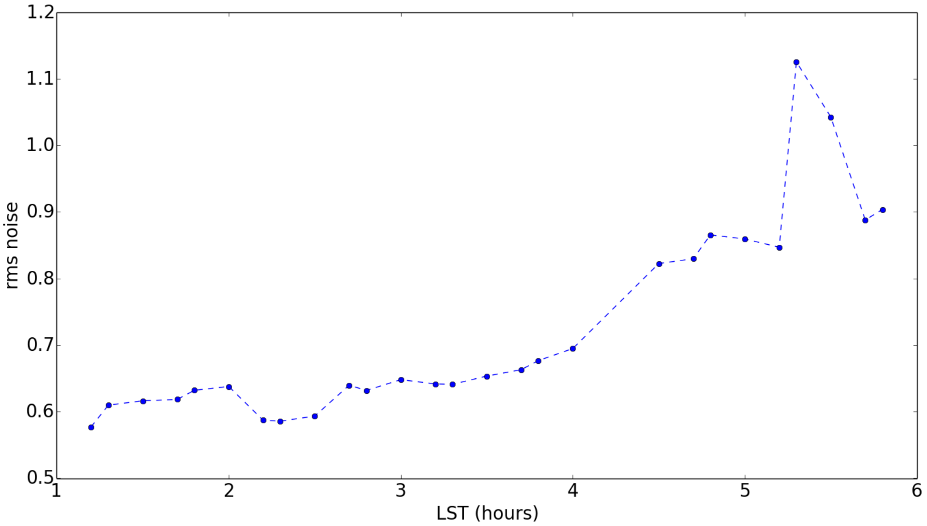

FIGURE 3.15: Rms noise calculated for each snapshot image as a function of LST after solving for direction dependent calibration. These rms values per snapshot image are tied to an absolute value (see Figure 4.1) after absolute flux calibration of individual snapshots as described in Section 3.8.

The apparent flux density of Pictor A in snapshot images for LSTs between 2.8 and 5.8 hours was extracted using PyBDSM[2], by fitting a two dimensional Gaussian to the source.

In order to absolutely calibrate each snapshot image i, we derived a scaling factor between the observed and model flux densities of Pictor A as,

$$c_i = \frac{F_\nu^m \, b_{\nu_i}}{F_{\nu_i}} \tag{3.9}$$

where $\nu = 149.75$ MHz is the frequency of the snapshot images, F_{ν_i} is the apparent flux density of Pictor A measured for the i snapshot image and b_{ν_i} is the primary beam evaluated at the frequency ν and position of Pictor A for the i snapshot image. The error Δc_i on the scaling factor was calculated using the error propagation:

$$\Delta c_i = \sqrt{\left(\frac{b_{\nu_i}}{F_{\nu_i}}\right)^2 \left(\frac{\nu}{\nu_0}\right)^{-2\beta} \left[(\Delta A_{\nu 0})^2 + (A_{\nu 0})^2 \left(\ln\frac{\nu}{\nu_0}\right)^2 (\Delta\beta)^2\right] + \left(\frac{F_\nu^m b_{\nu_i}}{F_{\nu_i}^2}\right)^2 (\Delta F_{\nu_i})^2} \tag{3.10}$$

and displayed in Figure 3.16.

We found that c_i has a strong correlation with the LST, monotonically decreasing as the source approaches transit, whereas in an ideal case we would expect c_i to be flat across the LST. Such behaviour can be explained if the adopted beam model suffers from a

---

[2] Python Blob Detection and Source Measurement, a source finding algorithm (refer Section 4.1).

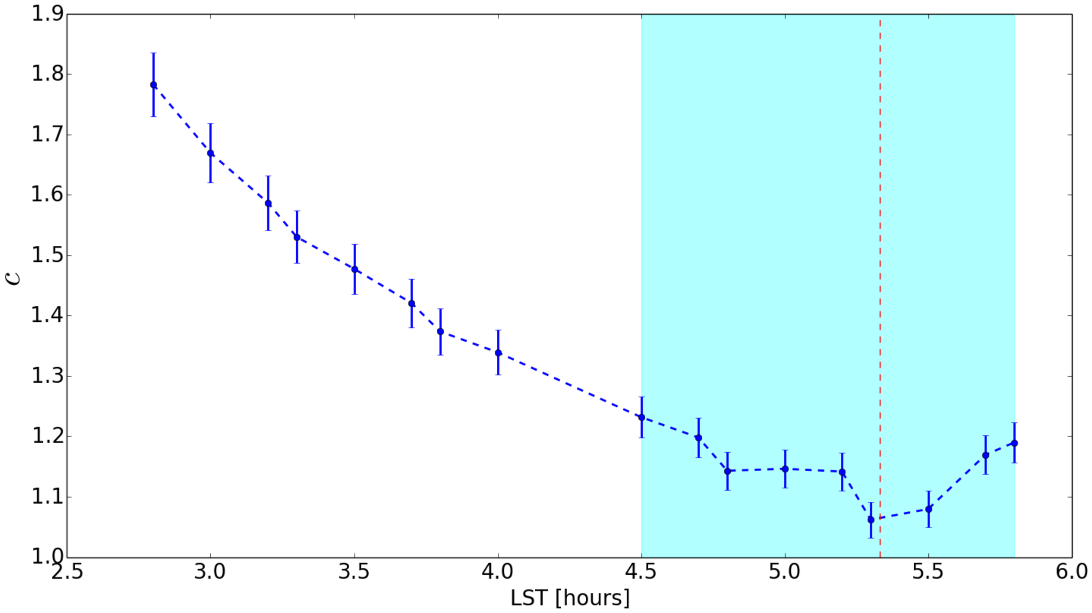

FIGURE 3.16: Scaling factor computed using Pictor A (see text for details). The red dashed line marks the transit of Pictor A. The region highlighted in cyan denotes the LST range over which Pictor A was used for absolute calibration.

systematic error, although variations in the system temperature or the individual dipole gains can also play a role.

In the presence of such trend, using Pictor A to absolutely calibrate all the snapshots is not ideal, as inaccuracies in the primary beam model will affect the absolute calibration for LST $\leq$ 4 hours, introducing a systematic error in the measurement of source flux densities. We decided, therefore, to adopt a multi-step approach to perform the absolute flux calibration of the whole data set: Pictor A was used as primary calibrator and a set of secondary sources were identified as secondary calibrators.

The behaviour of the scaling factor derived from Pictor A indicates that, within $\sim$ 50 minutes from transit, the beam model is sufficiently precise and system variations can be considered small (see the region highlighted in cyan in Figure 3.16). We therefore decided to use Pictor A to calibrate the snapshot images whose centre fell in the $4.5 \leq \text{LST} \leq 5.8$ hour range and then, in the absolutely calibrated snapshot images, identify a subset of bright sources that could serve as calibrators for the previous LST range. We selected four other sources to be used as secondary calibrators (see Table 3.2) amongst the brightest ones (with apparent flux density greater than 18 Jy) and in the $-45° < \delta < -15°$ range. The choice of the declination was dictated by the need to minimize possible primary beam deviations between the source and Pictor A. Eventually we carried out a three step absolute calibration:

Table 3.2: Sources used for absolute flux calibration other than Pictor A. The third column indicates the LST range over which the sources were used.

Source ID (NED)[3]	Transit (hours)	LST range (hours)
J0351-2744	3.86	$3 \leq \mathrm{LST} \leq 4$
J0346-3423	3.77	
J0216-1305	2.27	$1.2 \leq \mathrm{LST} \leq 2.8$
J0200-3052	2.00	

- snapshot images with centre in the $4.5 \leq \mathrm{LST} \leq 5.8$ hour range were calibrated using Pictor A. Absolutely calibrated flux density measurements for sources J0351-2744 and J0346-3423 were derived from this set of images;
- snapshot images with centre in the $3 \leq \mathrm{LST} \leq 4$ hour range were calibrated using J0351-2744 and J0346-3423. Absolutely calibrated flux density measurements for sources J0216-1305 and J0200-3052 were derived from this set of images;
- snapshot images with centre in the $1.2 \leq \mathrm{LST} \leq 2.8$ hour range were calibrated using J0216-1305 and J0200-3052.

Absolutely calibrated, beam corrected flux densities F^c of a secondary calibrator j were obtained by a weighted average of the measurements over the individual snapshots i:

$$F^c = \frac{\displaystyle\sum_{i=1}^{N} \frac{F_i^c}{({\sigma^c}_i)^2}}{\displaystyle\sum_{i=1}^{N} ({\sigma^c}_i)^{-2}} \tag{3.11}$$

where σ_i^c is the error associated to F_i^c. The scaling factor for a snapshot i that was not absolutely flux calibrated using Pictor A was obtained by averaging the scaling factors c_j for each source j:

$$c_i = \frac{\displaystyle\sum_{j=1}^{2} \frac{c_{i,j}}{(\sigma_{i,j})^2}}{\displaystyle\sum_{j=1}^{2} (\sigma_{i,j})^{-2}} \tag{3.12}$$

where σ_j is the flux density errors of secondary calibrators .

The scaling factors for the whole LST range spanned by our observations are displayed in Figure 3.17. The scaling factors derived from the secondary calibrators have higher

---

[3] The NASA/IPAC Extragalactic Database (NED) is operated by the Jet Propulsion Laboratory,California Institute of Technology, under contract with the National Aeronautics and Space Administration.

uncertainties as they have a poorer signal-to-noise (SNR) ratio than Pictor A. The overall accuracy on the absolute calibration is, however, within $\sim 10\%$.

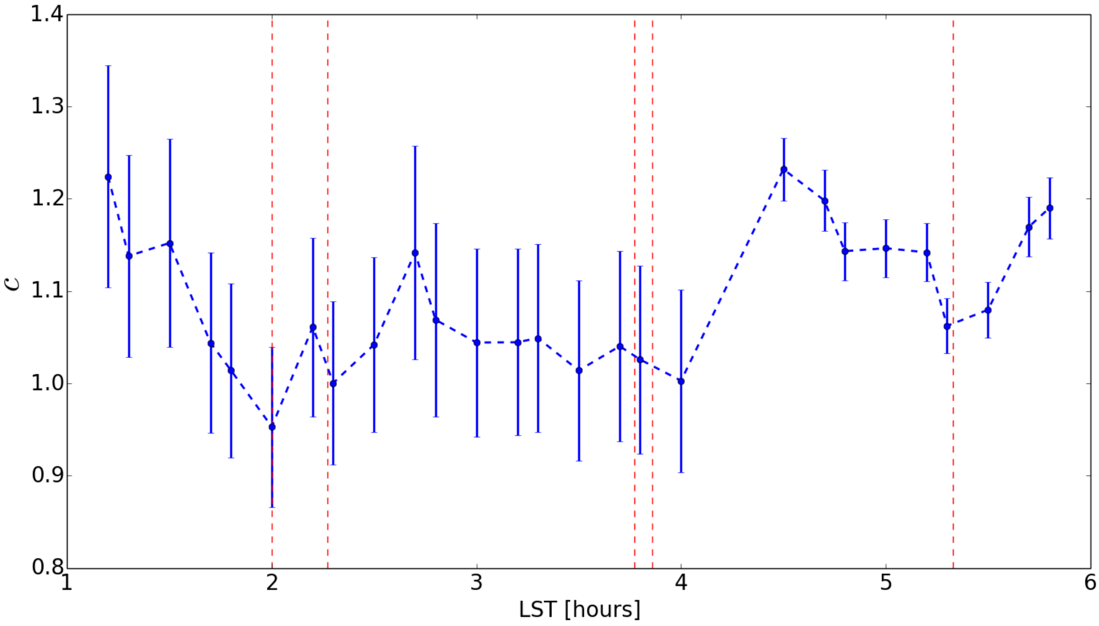

FIGURE 3.17: Scaling factors for the whole LST range spanned by our observations. Transcits of sources used for calibration are denoted by red dashed lines.

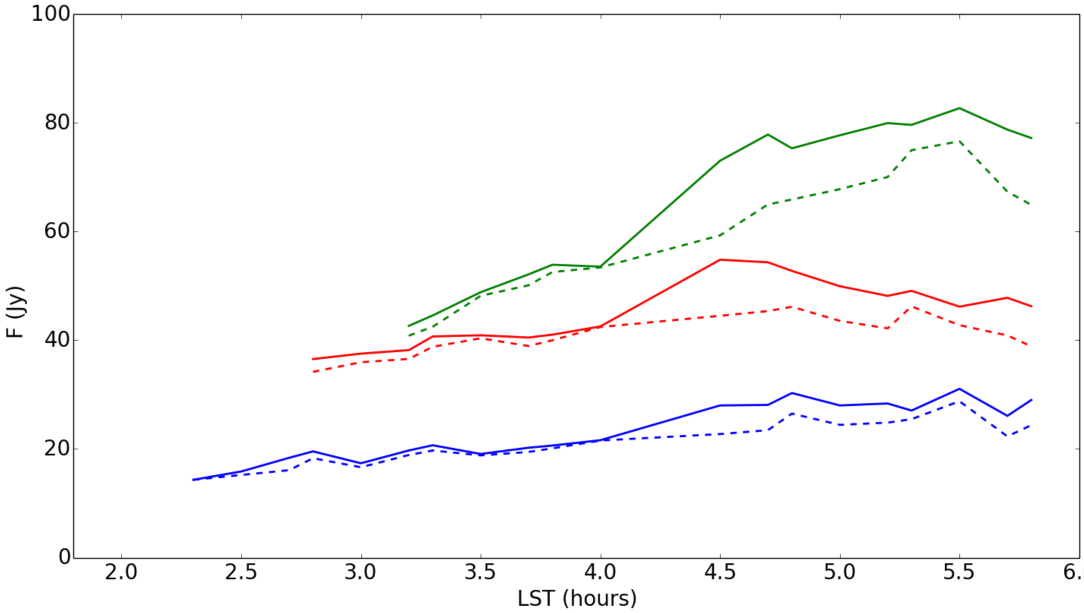

FIGURE 3.18: Flux density values for sources J0522-3627 (green line), J0444-2809 (red line) and J0429-5349 (blue line) as a function of LST before (dashed) and after (solid) absolute calibration. Other bright sources present a similar trend.

We tested the goodness of the absolute calibration by inspecting the flux density of the brightest sources extracted from the snapshot images. The comparison for the three brightest sources (J0429-5349, J0444-2809 and J0522-3627) of our sample is displayed in

Figure 3.18. We notice that the correction does not noticeably change the flux density distribution as a function of LST as, instead, it should be expected. For sources red and blue (J0429-5349 and J0444-2809) the flux density distribution was already relatively flat across the LST range and the absolute calibration procedure did not dramatically change the behaviour. Unfortunately our calibration procedure did not significantly flatten the flux density distribution for source green (J0522-3627) either as it would have been expected. It is not clear why the absolute calibration fails in the case of J0522-3627 and this is will be the subject of future inspection. We cannot exclude that our assumption that an image based scaling factor is not sufficient to provide an accurate correction and an antenna based gain calibration is required. In the next section we will provide more quantitative tests of the accuracy of our data analysis.

Chapter 4

Source catalogue

After absolute flux calibrating all the snapshot images, we proceed towards generating a catalogue from 27 snapshot images. The first step in catalogue generation is source extraction. Sources can either be extracted from individual snapshot images or from a mosaic image which is formed by combining data from different pointings (Sault et al., 1996). Mosaicing generally is done using pointings spaced at the half width of the primary beam apart in order to achieve a uniform noise over the observed sky patch. A drift scan observation is, therefore, not optimal for mosaicing because it covers the sky along the right ascension axis only, leading to a non uniform noise across the mosaic. Moreover, the beam response for a source away from the pointing direction of the mosaiced image will be significantly lower compared to the response for the same source in a snapshot the source is close to the pointing direction, making calibration more prone to beam uncertainties.

We eventually decided to generate a source catalogue by adopting a different approach where sources were extracted from each individual snapshot and the final catalogue formed from the individual catalogues.

4.1 Source extraction

In order to extract sources from the absolutely calibrated images, a source finder software called PyBDSM (Python Blob Detection and Source Measurement, Mohan & Rafferty, 2015) was run on all the snapshot images. PyBDSM runs on a Python based interactive environment and is integrated to operate with Python scripting. Absolutely calibrated images were not corrected for the primary beam. Source candidates are identified in islands of pixels brighter than a certain threshold. We set this threshold to be three times the standard deviation of the image noise, assumed to be uniform across each

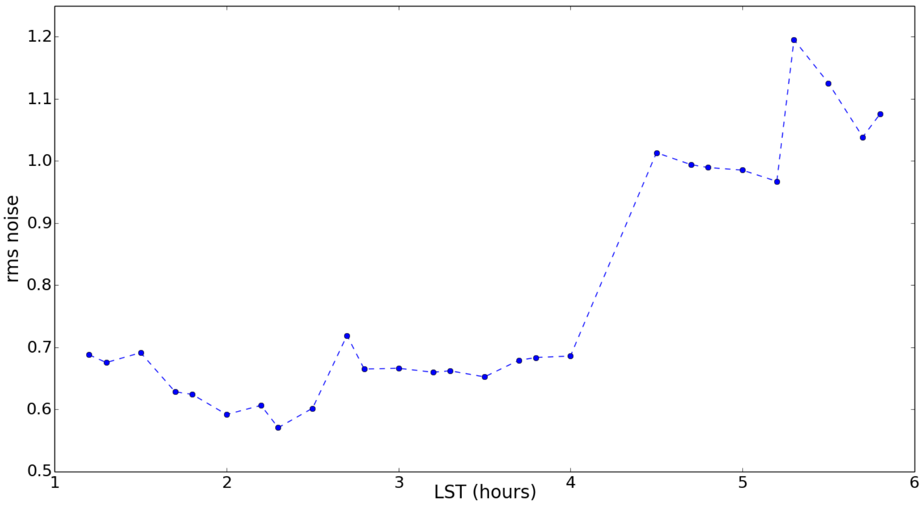

FIGURE 4.1: Rms noise calculated for each snapshot image as a function of LST, after absolute flux calibration.

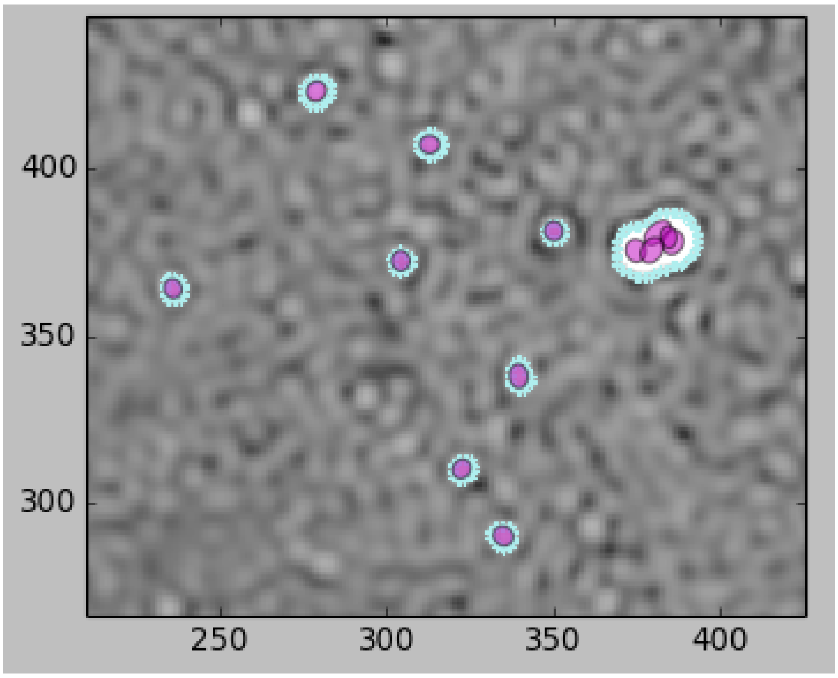

FIGURE 4.2: PyBDSM identifying potential source candidates in one of the snapshot images. The axes are labelled in pixel numbers, with each pixel of size $3' \times 3'$. Marked in cyan are the identified island boundaries. Pink areas correspond to the pixels actually used in the fit.

snapshot image. The noise estimated by PyBDSM varies up to $\sim 20\%$ from snapshot to snapshot across the whole LST range (Figure 4.1).

Within each island, a sub-set of connected pixels above a certain threshold are used to fit a two dimensional Gaussian to the source candidate (or multiple Gaussians in case of overlapping candidate sources, see Figure 4.2). As our goal is to create a catalogue useful for calibration, we are only interested in the brightest sources. We therefore set the threshold to be seven times the noise rms. The number of sources extracted for each catalogue forms a snapshot catalogue.

4.2 Source matching

After generating the snapshot catalogues, we proceeded by merging them into a final one. As image snapshots overlap within a certain LST range, each snapshot catalogue does not contain a unique set of sources. We therefore "clustered" sources together across the various snapshot catalogues, i.e. we matched together the common sources. Source clustering was performed as follows:

- each source s in catalogue C_i was matched to the closest source in all the $C_{j,j\neq i}$ catalogues, where $i,j = \{1,2,3,...\ 27\}$ (i.e. across all the 27 catalogues), within a tolerance distance of 20 arcminutes. This form a cluster of sources;
- after clustering, source s along with the matching sources were removed from all the C_j catalogues in order to avoid multiple associations of the same source;
- the above steps were repeated for all the sources in the C_j catalogues.

Afterwards, the flux density F of each source was calculated as:

$$F = \frac{\sum_{i=1}^{N} \left(\frac{F_i\ b_i}{\sigma_i^2} \right)}{\sum_{i=1}^{N} \left(\frac{b_i}{\sigma_i^2} \right)} \tag{4.1}$$

where b_i is the primary beam response towards the source in snapshot i, N is the number of sources in the cluster where the source is present and σ_i is the error associated with the extracted flux density F_i.

A final catalogue of 284 sources was generated. As the PAPER correlator does not introduce correction for precession, such correction was applied to the catalogue positions.

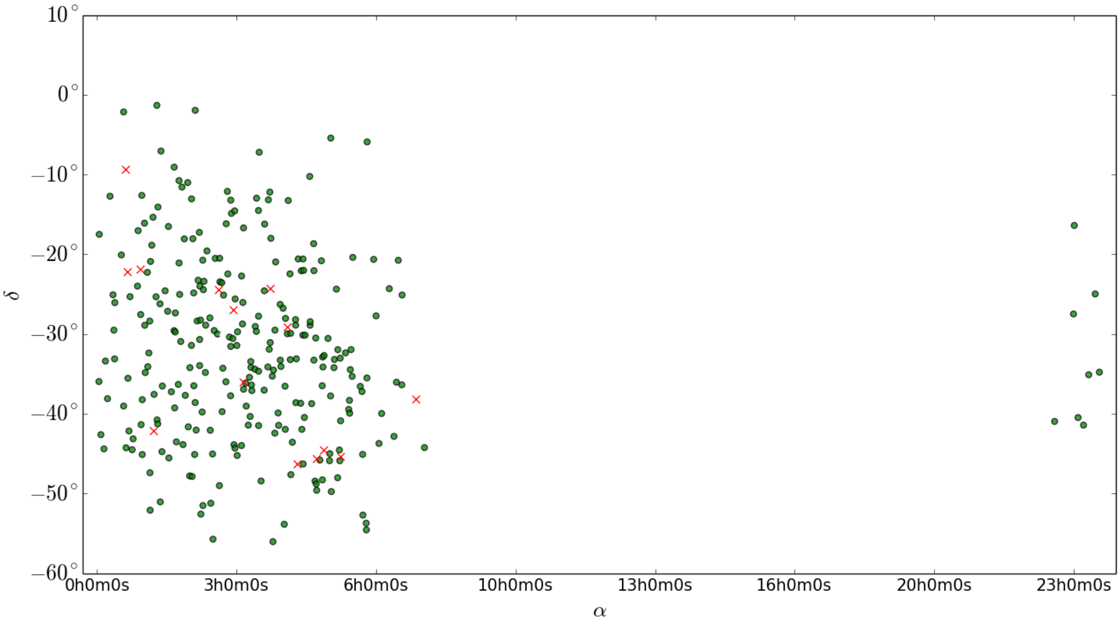

FIGURE 4.3: PSA32 sources that match with PKSCAT90 sources within a tolerance of 15′ are shown in green, while 14 unmatched PSA32 sources are indicated by red x marks.

4.3 Comparison with the Parkes-MIT-NRAO catalogue

After the catalogue of 284 unique sources is generated, it was compared with the Parkes–MIT–NRAO catalogue [1] (PKSCAT90 hereafter; Wright & Otrupcek (1990). The major reason in selecting PKSCAT90 for comparison is because PKSCAT90 covers all the sky south of declination +27° and contains 8264 radio sources with flux density measurements at different frequencies ranging from 80 MHz to 22 GHz, excluding the Galactic plane and the Magellanic cloud regions. The search for counterparts of PKSCAT90 sources was carried out by matching the closest sources in the two catalogues, using a 5′, 10′ and 15′ tolerance respectively. Table 4.3 shows the number of matching sources at the different search radii.

TABLE 4.1: Matched sources between our catalogue and PKSCAT90 at different search radii

Tolerance	Number of matched sources
5′	194
10′	268
15′	270

---

[1] Parkes Catalogue, 1990, Australia Telescope National Facility; http://vizier.cfa.harvard.edu/viz-bin/Cat?cat=VIII%2F15target=brief

Table 4.2: An attempt to cross-match 14 unmatched sources from Figure 4.3 via NED within a search radius of 15′. 7 sources were successfully matched to their counterparts, for which, columns NED Source ID, NED F (Jy) and NED ν (MHz) represent the source name, flux density value and the observed frequency. While 7 sources remained unmatched (represented using a dash (–)).

PSA32 (α, δ)	PSA32 F (Jy)	NED Source ID	NED F (Jy)	NED ν (MHz)	β
$00^{\mathrm{h}}41^{\mathrm{m}}24^{\mathrm{s}} - 09^{\circ}24'08''$	10.3	–	–	–	–
$00^{\mathrm{h}}44^{\mathrm{m}}02^{\mathrm{s}} - 22^{\circ}14'32''$	6.2	PMNJ0044-2212	2.1	365	-1.21
$01^{\mathrm{h}}02^{\mathrm{m}}32^{\mathrm{s}} - 21^{\circ}55'18''$	10.9	NVSSJ010241-215230	23	74	-1.17
$01^{\mathrm{h}}21^{\mathrm{m}}32^{\mathrm{s}} - 42^{\circ}10'54''$	6.0	PMNJ0121-4206	2.48	408	-0.89
$02^{\mathrm{h}}54^{\mathrm{m}}46^{\mathrm{s}} - 24^{\circ}29'08''$	5.2	LEDA2823297	1.8	365	-1.12
$03^{\mathrm{h}}15^{\mathrm{m}}55^{\mathrm{s}} - 27^{\circ}01'07''$	7.5	LEDA2823460	1.8	408	-1.42
$03^{\mathrm{h}}30^{\mathrm{m}}08^{\mathrm{s}} - 36^{\circ}04'00''$	9.5	–	–	–	–
$04^{\mathrm{h}}08^{\mathrm{m}}48^{\mathrm{s}} - 24^{\circ}20'17''$	9.5	LEDA2823818	3.9	365	-1.0
$04^{\mathrm{h}}33^{\mathrm{m}}19^{\mathrm{s}} - 29^{\circ}10'09''$	5.9	–	–	–	–
$04^{\mathrm{h}}47^{\mathrm{m}}30^{\mathrm{s}} - 46^{\circ}20'19''$	13.1	–	–	–	–
$05^{\mathrm{h}}15^{\mathrm{m}}07^{\mathrm{s}} - 45^{\circ}41'07''$	11.0	–	–	–	–
$05^{\mathrm{h}}25^{\mathrm{m}}23^{\mathrm{s}} - 44^{\circ}35'57''$	10.5	–	–	–	–
$05^{\mathrm{h}}49^{\mathrm{m}}33^{\mathrm{s}} - 45^{\circ}24'18''$	10.8	–	–	–	–
$07^{\mathrm{h}}37^{\mathrm{m}}30^{\mathrm{s}} - 38^{\circ}12'36''$	12.7	PMNJ0737-3812	7.3	408	-0.55

Figure 4.3 shows 270 sources that found an association with a PKSCAT90 source, together with 14 unmatched sources which could not be matched within a search radius of 15′. These 14 unmatched sources were cross-matched using the NASA/IPAC Extragalactic Database (NED[2]) within tolerances of 5′, 10′ and 15′, Table 4.2 shows 7 out of 14 sources were successfully matched whereas 7 sources remained unmatched. The 7 unmatched sources do not have any data at radio wavelengths, however, their possible matches are:

- $00^{\mathrm{h}}41^{\mathrm{m}}24^{\mathrm{s}} - 09^{\circ}24'08''$: Is a galaxy with an apparent magnitude of 24.0 in the V band as identified by WIde Field Nearby Galaxy-cluster Survey (WINGS, Varela et al., 2009).
- $03^{\mathrm{h}}30^{\mathrm{m}}08^{\mathrm{s}} - 36^{\circ}04'00''$: Is a galaxy with a magnitude of 19.4 as identified by the Muenster Red Sky Survey (Ungruhe et al., 2003).
- $04^{\mathrm{h}}33^{\mathrm{m}}19^{\mathrm{s}} - 29^{\circ}10'09''$: Is a galaxy with a magnitude of 20.1 as identified by the Muenster Red Sky Survey (Ungruhe et al., 2003).
- $04^{\mathrm{h}}47^{\mathrm{m}}30^{\mathrm{s}} - 46^{\circ}20'19''$: Is a galaxy with a magnitude of 18.06 at 6.41×10^{14} Hz as identified by the APM galaxy survey (Maddox et al., 1990).

---

[2] https://ned.ipac.caltech.edu/

- $05^{\rm h}15^{\rm m}07^{\rm s} - 45°41'07''$: Is a galaxy with a magnitude of 19.71 as identified by the APM galaxy survey (Maddox et al., 1990).
- $05^{\rm h}25^{\rm m}23^{\rm s} - 44°35'57''$: Is a galaxy identified by the Two Micron All Sky Survey (2MASS, Skrutskie et al., 2006).
- $05^{\rm h}49^{\rm m}33^{\rm s} - 45°24'18''$: Is a galaxy (UV source) with a magnitude of 22.7 as identified by the Galaxy Evolution Explorer (GALEX [3]) satellite.

4.3.1 Positional errors

Figure 4.4 shows the positional differences between the nominal (i.e. PKSCAT90) and our catalogue positions. We tested the matching accuracy by plotting the positional differences as function of source flux density (Figure 4.5). By fitting a straight line to the distribution, we found that the median in right ascension and declination are $\langle \Delta\alpha \rangle = -2.4'$ and $\langle \Delta\delta \rangle = -2.1'$ respectively. Their distribution widens at lower flux densities as one would expect when positional errors are dominated by the signal-to-noise ratio. We also point out that we made no correction for ionospheric effects that may affect the fitted positions in our catalogue. With a standard deviation of $\sigma_\alpha \sim 2.5$ and $\sigma_\delta \sim 1.5$, the overall offsets are essentially within the statistical errors, consistent with the $1.2'$ error from Hurley-Walker et al. (2014) with a four times better angular resolution.

4.3.2 Spectral index distribution

We computed the spectral indices for the matched sources, using the PKSCAT90 flux density value at 408 MHz. The spectral index distribution of the matched sources as a function of tolerance ratio is displayed in Figure 4.6. We fitted a Gaussian to each spectral index distribution and found that the mean spectral index only marginally changes with the tolerance radius, $-0.79 < \beta < -0.78$ moving from $5'$ to $15'$ tolerance.

We compared our spectral index results with other surveys in the literature. The NRAO VLA Sky Survey (NVSS, Condon et al., 1998), covering 82% of the sky north of $\delta = -40°$ at 1.4 GHz comprised of 217446 snapshots, each of which was separately imaged at $45''$ FWHM. A catalogue of $\sim$ 2000000 sources was generated from the images, which spans radio sources and galaxies, quasars, pulsars, nebulae, stars, AGNs and galaxies in the IRAS Faint Source Catalogue (Moshir et al., 1992). Sources from the NVSS peak at brightness ≥ 2 mJy with an accuracy of 2%, and the positional offset is $\langle \alpha \rangle =$

---

[3] http://galex.stsci.edu/GR6/

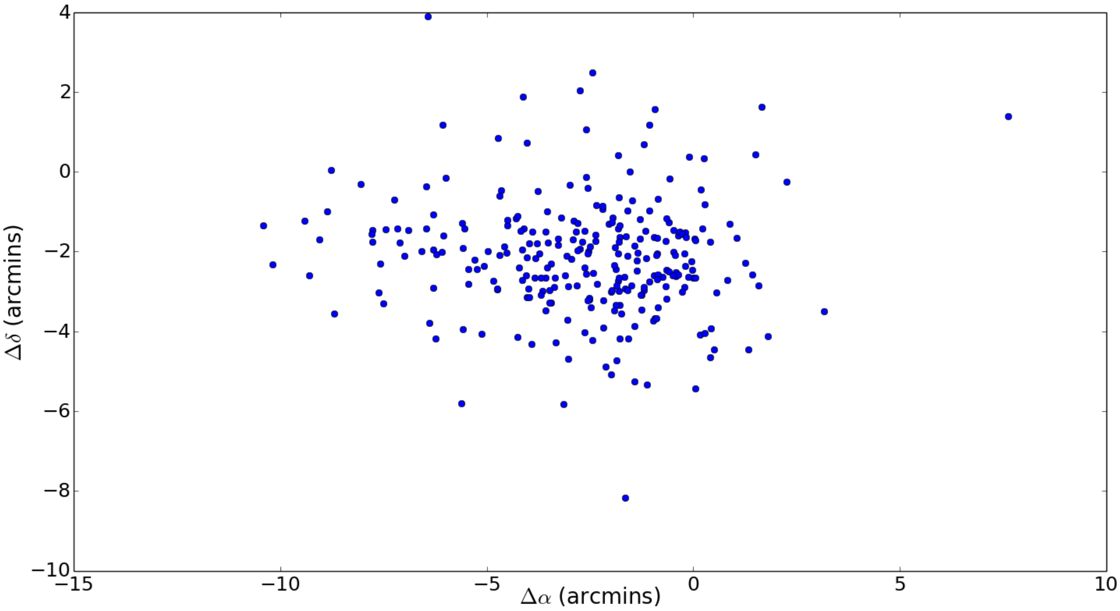

FIGURE 4.4: Difference between our catalogue and PKSCAT90 positions.

$0.025'' \pm 0.022''$ and $\langle\delta\rangle = 0.113'' \pm 0.027''$, and measured a median spectral index of $\langle\beta\rangle = -0.7$. The median spectral index value of our catalogue ($\langle\beta\rangle = -0.81$) is lower than this value.

The Sydney University Molongo Sky Survey (SUMSS, Mauch et al., 2003), describes a source catalogue at 843 MHz, extracted from 590 $4.3^\circ \times 4.3^\circ$ mosaic images at a resolution of $45'' \times 45''$cosecδ. The images cover approximately 3500 deg^2 of the southern sky, 43% out of the survey area. Mauch et al. (2003) compared SUMSS with NVSS, thus, yielding 7000 overlapping sources and measuring a median spectral index $\langle\beta_{843}^{1400}\rangle = -0.83\pm0.02$, consistent with DeBreuck et al. (2000), who reported the median of Texas[4]-NVSS spectral indices to be $\langle\beta_{365}^{1400}\rangle = -0.879$ with median spectral index error $\Delta\beta_{365}^{1400} = 0.04$ (for $F_{365} > 1$ Jy) to 0.07 (for $F_{365} > 150$ mJy). The median spectral index value of our catalogue, $\langle\beta\rangle = -0.81 \pm 0.02$, agrees with the values by DeBreuck et al. (2000) and Mauch et al. (2003).

Our spectral index distribution shows tails at steep and flat spectral index values. Following DeBreuck et al. (2000), the distribution was further analyzed by dividing it into steep population, $\beta > -0.60$ and flat population $\beta < -0.60$. After fitting a Gaussian to the distributions, we notice that the peaks of the steep and the flat populations at $\bar{\beta} = -0.95$ and $\bar{\beta} = -0.37$ do not show significant shifts over different tolerance values (Figure 4.7). Also, the $\bar{\beta}$ values where the steep and the flat population peaks in our

---

[4] The Texas survey was carried out using the Texas interferometer at a frequency of 365 MHz during 1974 - 1983 (Douglas et al., 1996).

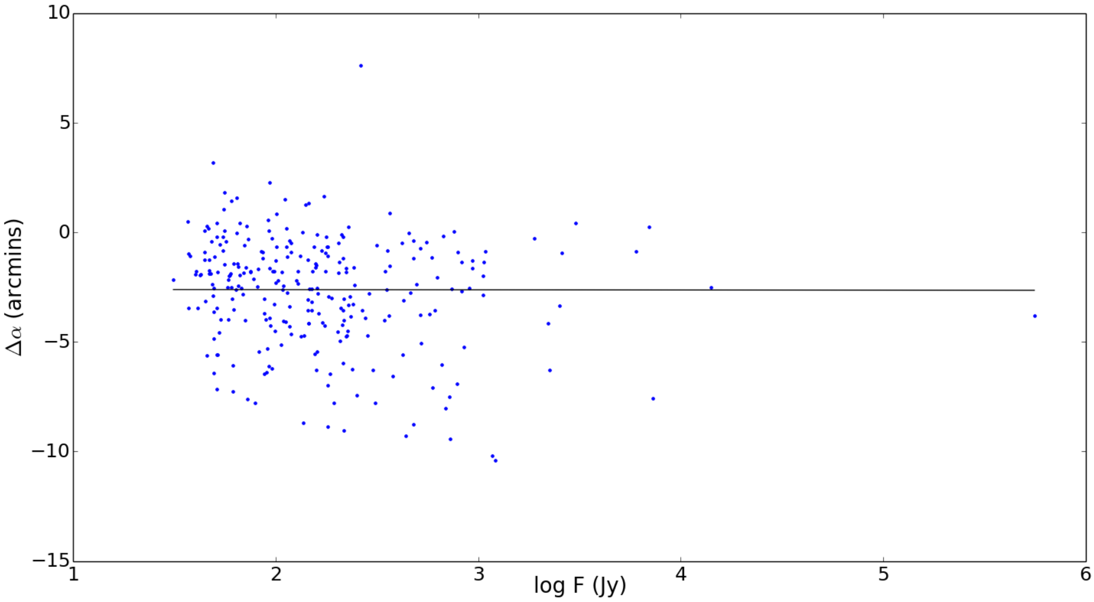

(A) Positional offset in right ascension, $\langle \Delta\alpha \rangle = -2.4'$

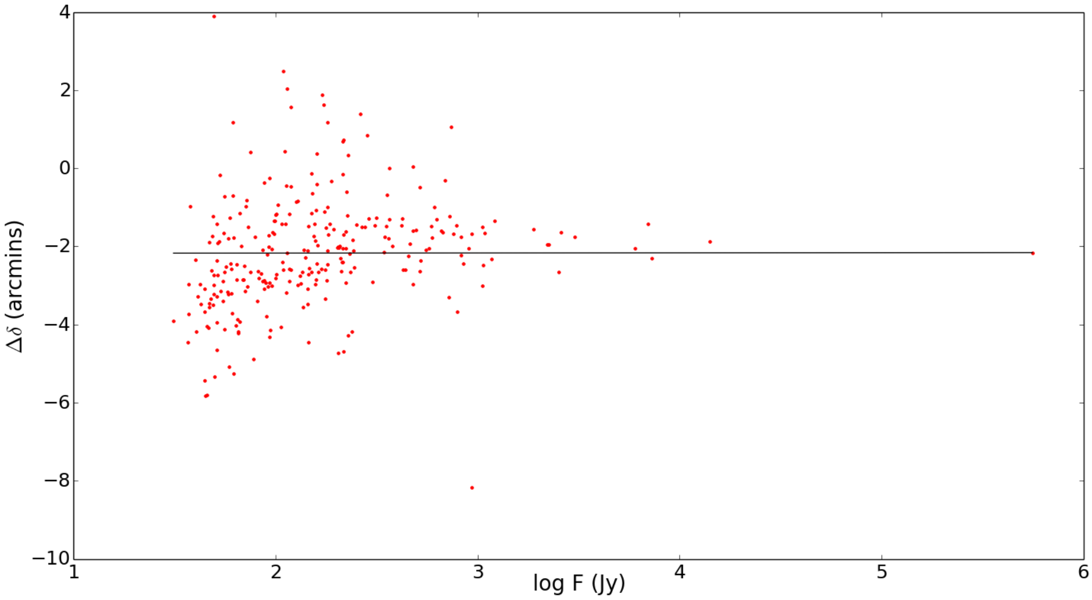

(B) Positional offset in declination, $\langle \Delta\delta \rangle = -2.1'$

FIGURE 4.5: Positional offsets in α and δ as a function of source flux density at 150 MHz. The solid lines indicate the corresponding median values.

Table 4.3: Outliers in the spectral index distribution.

Source ID	F (Jy) 149.75 MHz	F (Jy) 408 MHz	β
J0025-2602	13.0	17	0.27
J0038-0207	12.7	16.5	0.26
J0133-3629	28.3	160	1.73
J0219-4503	5.7	1.0	-1.76
J0241-2755	4.5	0.9	-1.62
J0333-3608	9.5	1.1	-2.19
J0348-2944	5.4	1.0	-1.68
J0440-4333	7.9	8.1	0.02
J0444-2809	43.8	220	1.61
J0505-2824	9.0	1.0	-2.16
J0534-4456	10.8	1.7	-1.84
J0534-3747	11.2	1.1	-2.33
J0535-0523	30.0	450	2.70
J0545-4756	10.4	1.4	-1.98
J0548-4554	10.3	2.0	-1.64
J0602-3957	9.3	1.4	-1.92
J0709-3603	11.6	2.2	-1.64

catalogue is consistent with the steep ($\bar{\beta} = -0.8$) and the flat ($\bar{\beta} = -0.4$) population peaking values mentioned in DeBreuck et al. (2000).

We report the outliers in Table. 4.3, sources with fairly flat spectral indices such as J0025-2602 (AGN), J0038-0207 (Seyfert galaxy) and J0440-4333 (flat spectrum radio source), all information via NED. The other outliers are of the type hybrid (FR-I + FR-II) extended radio sources, blazars and radio galaxies, they are synchrotron self-absorbed, that is, their emission is dominated by the core rather than the lobes.

At the end of our analysis it is worth commenting on the effect of different angular resolution on catalogue comparison as well as on the completeness of the derived catalogue. The PKSCAT90 catalogue is derived from observations with ~ 6 arcmin resolution, i.e. more than twice compared to ours, therefore blending of individual sources may be an issue at low flux densities. Significant source blending would, however, produce a steepening of the spectral index distribution, particularly at low flux densities. Our spectral index analysis does not show evidence of such effect, suggesting that blending should not significantly affect our catalogue given its relative shallow depth. Simulations where point sources are injected in the visibility data or in the images are normally used to quantify the catalogue completeness and this will be the subject of future work. As surveys normally approach completeness at the 6-8 σ level (Hurley-Walker et al., 2014; Mauch et al., 2003; Prandoni et al., 2000), we can conservatively consider our catalogue complete down to 8 Jy.

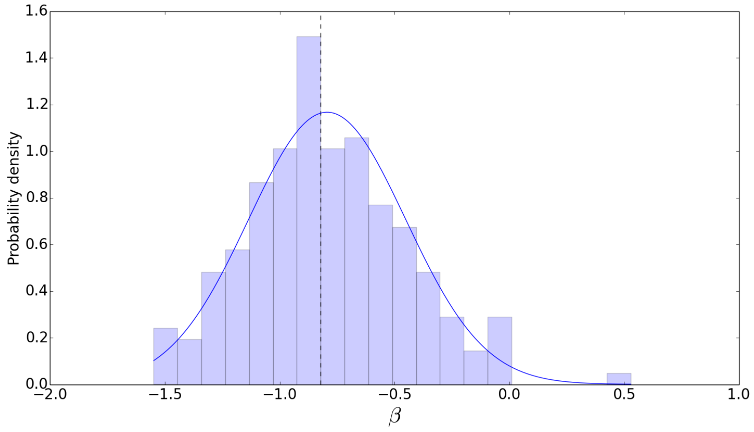

(A) 5 arcmins, $\mu = -0.79, \sigma = 0.34$ for the Gaussian fit, median $\langle\beta\rangle = -0.82 \pm 0.03$

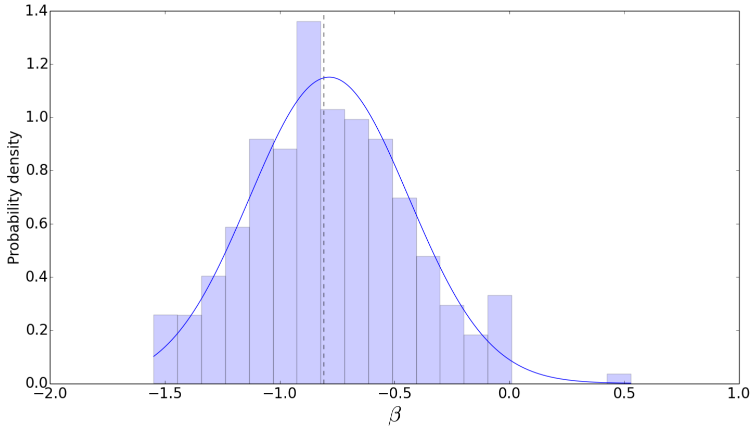

(B) 10 arcmins, $\mu = -0.78, \sigma = 0.35$ for the Gaussian fit, median $\langle\beta\rangle = -0.81 \pm 0.02$

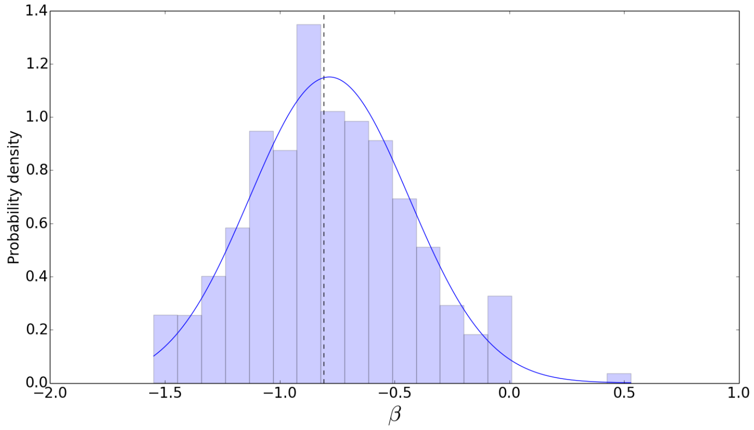

(C) 15 arcmins, $\mu = -0.78, \sigma = 0.35$ for the Gaussian fit, median $\langle\beta\rangle = -0.81 \pm 0.02$

FIGURE 4.6: Spectral index distribution of PSA32 sources and their matching PKSCAT90/NED counterparts within search radii of $5'$, $10'$ and $15'$. The dashed vertical line denotes the median spectral index value in each plot. The overall median value is $\langle\beta\rangle = -0.81 \pm 0.02$.

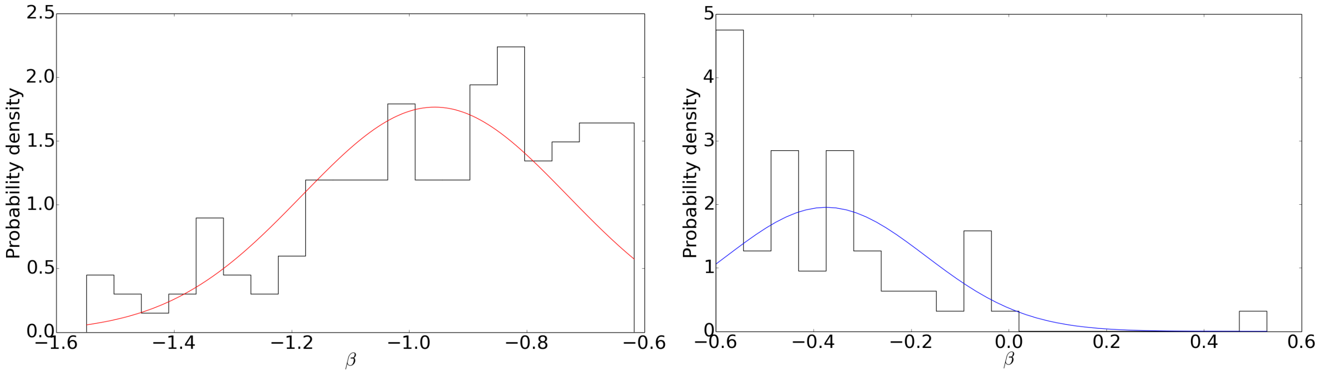

(A) Steep spectrum population at $5'$ tolerance, $\mu = -0.95$, $\sigma = 0.2$

(B) Flat spectrum population at $5'$ tolerance, $\mu = -0.37$, $\sigma = 0.2$

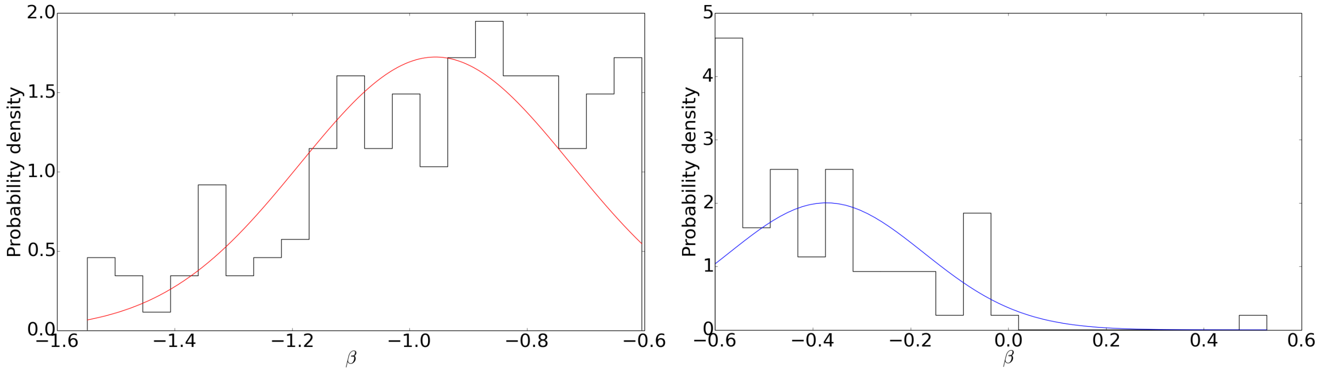

(C) Steep spectrum population at $10'$ tolerance, $\mu = -0.95$, $\sigma = 0.2$

(D) Flat spectrum population at $10'$ tolerance, $\mu = -0.37$, $\sigma = 0.2$

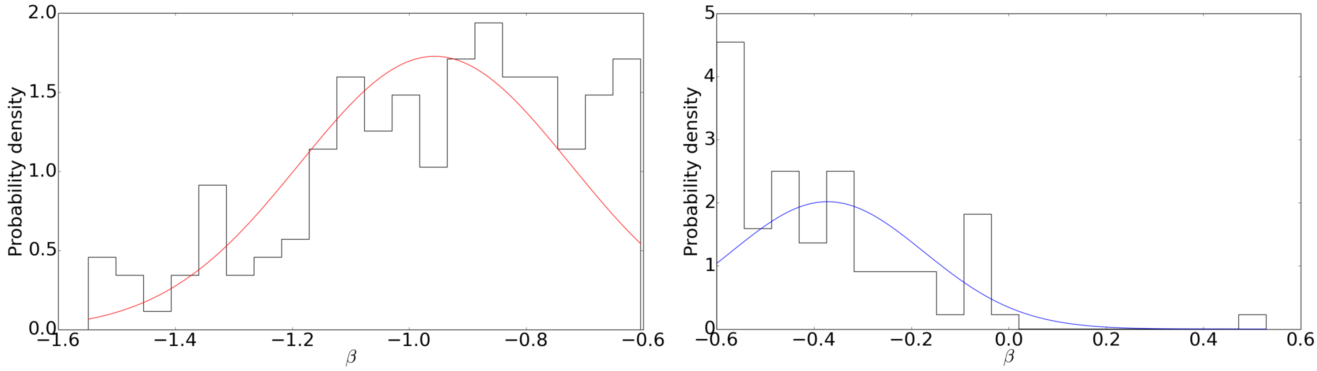

(E) Steep spectrum population at $15'$ tolerance, $\mu = -0.95$, $\sigma = 0.2$

(F) Flat spectrum population at $15'$ tolerance, $\mu = -0.37$, $\sigma = 0.2$

FIGURE 4.7: Sources in our catalogue distributed into steep (left) and flat (right) spectrum populations across tolerances of $5'$, $10'$ and $15'$.

4.4 Catalogue format

Our catalogue covers ~11000 deg^2, including 284 point sources excluding Fornax A and Pictor A down to a minimum flux density of 4.5 Jy. It is reported in Table 4.4. A description of each of the columns of the catalogue is as follows:

- Column 1 : Source name, taken from PKSCAT90 and the NASA/IPAC Extragalactic Database (NED). The term NA denotes the sources which failed to find an association during cross-matching.
- Columns 2 and 3 : The right ascension (α) and declination (δ) of the sources in J2000 coordinates taken from PKSCAT90 and NED.
- Column 4 : The source flux density at 149.75 MHz.
- Column 5 : The source spectral index.

TABLE 4.4: Final source catalogue extracted from PAPER data.

Source ID	α	δ	F (Jy)	β
J0003-3555	$00^{h}03^{m}09^{s}$	$-35^{\circ}55'03''$	7.1 ± 0.9	-1.06
J0003-1727	$00^{h}03^{m}22^{s}$	$-17^{\circ}27'11''$	8.7 ± 1.1	-0.28
J0006-4247	$00^{h}06^{m}18^{s}$	$-42^{\circ}47'01''$	7.1 ± 0.9	NA
J0010-4422	$00^{h}10^{m}29^{s}$	$-44^{\circ}22'54''$	11.0 ± 1.1	-0.48
J0012-3321	$00^{h}12^{m}19^{s}$	$-33^{\circ}21'51''$	6.0 ± 0.8	-0.70
J0015-3804	$00^{h}15^{m}24^{s}$	$-38^{\circ}04'31''$	8.5 ± 0.9	-0.55
J0018-1242	$00^{h}18^{m}51^{s}$	$-12^{\circ}42'33''$	8.2 ± 1.1	-0.18
J0023-2502	$00^{h}23^{m}08^{s}$	$-25^{\circ}02'40''$	7.6 ± 0.8	-0.35
J0024-2928	$00^{h}24^{m}30^{s}$	$-29^{\circ}28'52''$	12.6 ± 0.8	-0.48
J0025-3303	$00^{h}25^{m}32^{s}$	$-33^{\circ}03'07''$	7.2±0.8	-0.56
PKS 0023-26	$00^{h}25^{m}46^{s}$	$-26^{\circ}02'18''$	12.9±0.9	-0.28
J0035-2003	$00^{h}35^{m}08^{s}$	$-20^{\circ}03'59''$	8.8±0.9	-0.25
3C 017	$00^{h}38^{m}18^{s}$	$-02^{\circ}07'44''$	12.8±1.6	-0.4
J0038-3859	$00^{h}38^{m}26^{s}$	$-38^{\circ}59'46''$	10.3±0.9	-0.57
NA	$00^{h}41^{m}24^{s}$	$-09^{\circ}24'08''$	10.3±1.2	NA
J0042-4414	$00^{h}42^{m}9^{s}$	$-44^{\circ}14'15''$	16.0±1.0	-0.45
PMNJ0044-2212	$00^{h}44^{m}8^{s}$	$-22^{\circ}12'31''$	6.2±0.8	-1.21
J0044-3530	$00^{h}44^{m}41^{s}$	$-35^{\circ}30'41''$	7.7±0.8	-0.28
J0046-4207	$00^{h}46^{m}16^{s}$	$-42^{\circ}07'37''$	28.6±0.9	-0.60
J0047-2517	$00^{h}47^{m}32^{s}$	$-25^{\circ}17'18''$	14.4±0.8	-0.85
J0050-4428	$00^{h}50^{m}52^{s}$	$-44^{\circ}28'38''$	9.5±0.9	-0.69

Source ID	α	δ	F (Jy)	β
J0052-4306	$00^h52^m15^s$	$-43°06'30''$	13.2±0.9	-0.49
J0058-2401	$00^h58^m28^s$	$-24°01'07''$	6.0±0.7	-1.15
J0059-1700	$00^h59^m06^s$	$-17°00'38''$	9.6±0.9	-0.43
NVSSJ010241-215230	$01^h02^m41^s$	$-21°52'30''$	10.9±0.8	-1.17
J0102-2731	$01^h02^m44^s$	$-27°31'13''$	5.9±0.7	-0.67
J0103-4120	$01^h03^m45^s$	$-41°20'43''$	5.5±0.7	-0.59
J0104-1235	$01^h04^m22^s$	$-12°35'29''$	7.3±0.9	-0.34
J0105-3811	$01^h05^m09^s$	$-38°11'19''$	7.0±0.8	-0.59
J0105-4505	$01^h05^m20^s$	$-45°5'32''$	18.1±1.0	-1.03
J0108-1604	$01^h08^m16^s$	$-16°04'20''$	18.5±0.9	-0.34
J0108-2851	$01^h08^m37^s$	$-28°51'31''$	5.5±0.7	-0.49
J0109-3447	$01^h09^m25^s$	$-34°47'19''$	5.4±0.7	-0.57
J0112-2210	$01^h12^m24^s$	$-22°10'37''$	5.2±0.7	-1.38
J0113-3403	$01^h13^m04^s$	$-34°03'08''$	4.8±0.7	-1.06
J0114-3217	$01^h14^m20^s$	$-32°17'57''$	5.5±0.7	NA
J0115-2817	$01^h15^m39^s$	$-28°17'15''$	5.2±0.7	-1.12
J0116-4722	$01^h16^m25^s$	$-47°22'40''$	12.1±1.0	-0.15
J0116-5202	$01^h16^m46^s$	$-52°02'18''$	8.5±0.9	-0.82
J0116-2052	$01^h16^m51^s$	$-20°52'06''$	10.8±0.8	-0.02
J0118-1849	$01^h18^m34^s$	$-18°49'17''$	6.1±0.8	-0.63
J0120-1520	$01^h20^m27^s$	$-15°20'16''$	16.4±0.9	-0.19
PMNJ0121-4206	$01^h21^m47^s$	$-42°07'06''$	6.0±0.7	-0.89
J0122-3731	$01^h22^m03^s$	$-37°31'37''$	8.8±0.7	-0.85
J0124-2517	$01^h24^m45^s$	$-25°17'10''$	7.2±0.7	-0.64
J0126-0120	$01^h26^m00^s$	$-01°20'41''$	17.6±1.8	-0.07
J0126-4048	$01^h26^m47^s$	$-40°48'39''$	6.6±0.7	-1.70
J0127-4112	$01^h27^m14^s$	$-41°12'44''$	8.7±0.8	-0.78
J0127-1402	$01^h27^m30^s$	$-14°02'52''$	10.4±0.9	-0.34
J0130-2610	$01^h30^m28^s$	$-26°10'05''$	10.9±0.8	-0.71
J0131-5101	$01^h31^m15^s$	$-51°01'29''$	6.7±0.9	-0.58
J0132-0652	$01^h32^m12^s$	$-06°52'36''$	7.7±1.1	-0.72
J0133-4431	$01^h33^m02^s$	$-44°31'02''$	9.0 ±0.9	NA
NGC 0612	$01^h33^m50^s$	$-36°29'25''$	28.3 ±0.8	-0.90
J0137-2430	$01^h37^m38^s$	$-24°30'53''$	5.3 ±0.6	-0.88
J0141-2706	$01^h41^m27^s$	$-27°06'07''$	8.2±0.8	-0.49
J0142-1628	$01^h42^m24^s$	$-16°28'22''$	8.4±0.9	-0.59
J0143-4529	$01^h43^m25^s$	$-45°29'53''$	6.8±0.8	-0.73

Source ID	α	δ	F (Jy)	β
J0146-3711	$01^h46^m46^s$	$-37^\circ11'52''$	5.8±0.7	-0.98
J0150-2932	$01^h50^m34^s$	$-29^\circ32'00''$	15.1±0.8	-0.76
J0150-0901	$01^h50^m51^s$	$-09^\circ01'33''$	7.0±0.9	-0.54
J0151-3910	$01^h51^m43^s$	$-39^\circ10'07''$	5.3±0.7	-0.77
J0151-2940	$01^h51^m59^s$	$-29^\circ40'50''$	5.7±0.7	-0.86
J0152-2718	$01^h52^m24^s$	$-27^\circ18'32''$	5.4 ±0.7	-1.02
J0154-4327	$01^h54^m09^s$	$-43^\circ27'43''$	5.5 ±0.7	-1.05
J0156-3616	$01^h56^m47^s$	$-36^\circ16'32''$	7.9 ±0.7	-0.68
J0157-1043	$01^h57^m41^s$	$-10^\circ43'40''$	7.8±0.9	-0.38
J0157-2102	$01^h57^m52^s$	$-21^\circ02'08''$	5.0 ±0.7	-0.74
J0158-2458	$01^h58^m32^s$	$-24^\circ58'48''$	5.7 ±0.8	-1.41
J0200-3053	$02^h00^m12^s$	$-30^\circ53'26''$	20.5 ±0.8	-0.69
J0201-1132	$02^h01^m57^s$	$-11^\circ32'33''$	6.2 ±0.9	-0.09
J0203-4349	$02^h03^m40^s$	$-43^\circ49'51''$	9.0 ±0.9	-0.38
J0205-1801	$02^h05^m20^s$	$-18^\circ01'11''$	5.9 ±0.8	-0.74
J0206-3738	$02^h06^m48^s$	$-37^\circ38'24''$	5.5±0.7	-0.89
J0210-1057	$02^h10^m06^s$	$-10^\circ57'52''$	6.9±0.9	-0.36
J0211-4138	$02^h11^m19^s$	$-41^\circ38'02''$	6.0 ±0.8	NA
J0213-4743	$02^h13^m09^s$	$-47^\circ43'41''$	7.6 ±0.9	NA
J0213-3413	$02^h13^m16^s$	$-34^\circ13'41''$	6.5 ±0.7	-1.03
J0215-3121	$02^h15^m27^s$	$-31^\circ21'58''$	4.8 ±0.7	-0.56
J0215-1313	$02^h15^m48^s$	$-13^\circ13'14''$	18.2 ±1.0	NA
J0216-4749	$02^h16^m45^s$	$-47^\circ49'09''$	12.0 ± 0.9	-0.23
J0217-1757	$02^h17^m32^s$	$-17^\circ57'53''$	5.9 ±0.8	-0.94
J0218-2448	$02^h18^m43^s$	$-24^\circ48'12''$	9.0 ±0.8	-0.78
J0219-3625	$02^h19^m02^s$	$-36^\circ25'24''$	10.6 ±0.8	-0.96
LCRS B021805.9-451805	$02^h19^m57^s$	$-45^\circ03'58''$	5.7 ±0.8	-1.04
J0220-0156	$02^h20^m54^s$	$-01^\circ56'53''$	13.0 ±1.7	-0.09
J0220-3832	$02^h20^m57^s$	$-38^\circ32'53''$	7.0 ±0.7	-0.85
J0222-4159	$02^h22^m18^s$	$-41^\circ59'51''$	7.4±0.8	-0.76
J0223-2819	$02^h23^m43^s$	$-28^\circ18'59''$	9.5±0.7	-0.89
J0225-2312	$02^h25^m02^s$	$-23^\circ12'45''$	9.4±0.8	-0.55
J0226-3041	$02^h26^m25^s$	$-30^\circ41'25''$	6.0 ±0.7	-1.86
J0227-1713	$02^h27^m04^s$	$-17^\circ13'23''$	5.5±0.7	-0.66
J0227-3352	$02^h27^m18^s$	$-33^\circ52'46''$	6.6±0.7	-1.11
J0227-2354	$02^h27^m33^s$	$-23^\circ54'49''$	5.5 ±0.7	-0.93
J0228-2813	$02^h28^m28^s$	$-28^\circ13'45''$	5.3±0.6	-1.28

Source ID	α	δ	F (Jy)	β
J0229-5232	$02^{h}29^{m}25^{s}$	$-52^{\circ}32'10''$	6.4±0.9	-0.49
J0230-3944	$02^{h}30^{m}56^{s}$	$-39^{\circ}44'16''$	6.3 ±0.7	-0.71
J0231-2040	$02^{h}31^{m}37^{s}$	$-20^{\circ}40'35''$	5.3 ±0.7	NA
J0232-5127	$02^{h}32^{m}16^{s}$	$-51^{\circ}27'09''$	7.1 ±0.9	-0.60
J0232-2422	$02^{h}32^{m}28^{s}$	$-24^{\circ}22'13''$	4.8 ±0.6	-0.82
J0233-2321	$02^{h}33^{m}23^{s}$	$-23^{\circ}21'11''$	9.5 ±0.8	-0.85
J0235-3445	$02^{h}35^{m}29^{s}$	$-34^{\circ}45'30''$	5.0 ±0.7	-1.12
J0235-2850	$02^{h}35^{m}54^{s}$	$-28^{\circ}50'46''$	5.1 ±0.7	-0.95
J0237-1932	$02^{h}37^{m}43^{s}$	$-19^{\circ}32'31''$	20.7±0.9	-0.44
PKS 0239-281	$02^{h}42^{m}03^{s}$	$-27^{\circ}55'40''$	4.5 ±0.6	-1.12
J0242-4201	$02^{h}42^{m}35^{s}$	$-42^{\circ}01'45''$	9.1 ±0.8	-0.77
J0243-5112	$02^{h}43^{m}43^{s}$	$-51^{\circ}12'35''$	19.5 ±1.2	-0.89
J0245-4459	$02^{h}45^{m}54^{s}$	$-44^{\circ}59'39''$	6.4 ±0.8	-0.81
J0246-5541	$02^{h}46^{m}55^{s}$	$-55^{\circ}41'19''$	14.1 ±1.1	-0.53
J0248-2931	$02^{h}48^{m}00^{s}$	$-29^{\circ}31'41''$	5.5 ±0.7	-1.24
J0249-2030	$02^{h}49^{m}34^{s}$	$-20^{\circ}30'40''$	5.6 ±0.7	NA
J0252-2958	$02^{h}52^{m}50^{s}$	$-29^{\circ}57'59''$	5.0 ±0.7	-1.33
LEDA2823297	$02^{h}54^{m}53^{s}$	$-24^{\circ}27'59''$	5.2 ±0.7	-1.21
J0255-2027	$02^{h}55^{m}51^{s}$	$-20^{\circ}27'49''$	6.3 ±0.8	-0.68
J0255-4858	$02^{h}55^{m}51^{s}$	$-48^{\circ}58'40''$	7.2 ±0.9	-0.86
J0256-2324	$02^{h}56^{m}15^{s}$	$-23^{\circ}24'42''$	14.6 ±0.9	-0.91
J0258-2330	$02^{h}58^{m}51^{s}$	$-23^{\circ}30'01''$	6.2 ±0.7	-1.04
J0259-3940	$02^{h}59^{m}26^{s}$	$-39^{\circ}40'35''$	5.3 ±0.7	-0.73
J0300-3414	$03^{h}00^{m}36^{s}$	$-34^{\circ}14'07''$	5.4 ±0.7	-1.17
J0301-2504	$03^{h}01^{m}22^{s}$	$-25^{\circ}04'32''$	5.4 ±0.7	-1.55
J0304-3556	$03^{h}04^{m}52^{s}$	$-35^{\circ}56'55''$	6.8 ±0.8	-0.84
J0305-1608	$03^{h}05^{m}14^{s}$	$-16^{\circ}08'06''$	5.8 ±0.8	-0.76
J0306-1205	$03^{h}06^{m}58^{s}$	$-12^{\circ}05'50''$	7.4 ±0.9	-0.29
J0307-2225	$03^{h}07^{m}31^{s}$	$-22^{\circ}25'26''$	9.5 ±0.8	-0.65
J0310-3019	$03^{h}10^{m}00^{s}$	$-30^{\circ}19'32''$	5.3±0.7	-1.09
J0311-3743	$03^{h}11^{m}44^{s}$	$-37^{\circ}43'38''$	5.4 ±0.7	-1.33
J0311-1311	$03^{h}11^{m}47^{s}$	$-13^{\circ}11'40''$	6.5 ±0.9	-0.79
J0311-3130	$03^{h}11^{m}52^{s}$	$-31^{\circ}30'12''$	5.8 ±0.7	-0.99
J0312-1450	$03^{h}12^{m}46^{s}$	$-14^{\circ}49'52''$	9.3 ±0.9	-0.42
J0314-3030	$03^{h}14^{m}47^{s}$	$-30^{\circ}30'17''$	5.2 ±0.7	-1.16
LEDA2823460	$03^{h}16^{m}01^{s}$	$-26^{\circ}57'59''$	7.5 ±0.8	-1.42
J0316-4351	$03^{h}16^{m}38^{s}$	$-43^{\circ}51'30''$	5.8 ±0.8	-0.85

Source ID	α	δ	F (Jy)	β
J0317-1430	$03^h17^m28^s$	$-14°30'48''$	6.9 ±0.9	-0.79
J0317-4414	$03^h17^m57^s$	$-44°14'17''$	7.2 ±0.8	-0.84
J0318-2535	$03^h18^m07^s$	$-25°35'17''$	4.8 ±0.7	-1.14
J0320-3124	$03^h20^m22^s$	$-31°24'37''$	5.7 ±0.7	-1.19
J0321-4510	$03^h21^m25^s$	$-45°10'35''$	17.4 ±1.1	-0.60
J0321-2940	$03^h21^m27^s$	$-29°40'45''$	5.7 ±0.7	-0.43
J0327-2239	$03^h27^m03^s$	$-22°39'57''$	5.4 ±0.7	-1.00
J0327-4356	$03^h27^m24^s$	$-43°56'36''$	8.7 ±0.9	-0.94
J0328-2841	$03^h28^m36^s$	$-28°41'35''$	8.4±0.8	-0.73
J0329-2600	$03^h29^m13^s$	$-26°00'12''$	6.5±0.7	-0.97
J0330-1638	$03^h30^m04^s$	$-16°38'40''$	7.2±0.9	-0.62
NA	$03^h30^m08^s$	$-36°04'00''$	9.5±1.3	NA
J0330-3653	$03^h30^m15^s$	$-36°53'37''$	9.1 ±0.9	-1.18
NGC 1365	$03^h33^m34^s$	$-36°08'28''$	9.5 ±1.3	-1.26
J0334-3900	$03^h34^m07^s$	$-39°00'02''$	10.2 ±0.9	-0.81
J0337-4123	$03^h37^m05^s$	$-41°23'29''$	10.3 ±0.9	-0.92
J0338-3523	$03^h38^m45^s$	$-35°23'27''$	13.9 ±0.9	-0.56
J0339-4018	$03^h39^m48^s$	$-40°18'09''$	10.7 ±0.9	-1.08
J0340-3325	$03^h40^m42^s$	$-33°25'24''$	5.6 ±0.7	-1.10
J0340-3410	$03^h40^m48^s$	$-34°10'01''$	6.2 ±0.8	-1.34
J0341-3622	$03^h41^m34^s$	$-36°22'22''$	5.4 ±0.7	-0.93
J0342-3703	$03^h42^m05^s$	$-37°03'21''$	8.7 ±0.8	-0.55
J0346-3422	$03^h46^m30^s$	$-34°22'46''$	18.5 ±1.0	-0.69
J0347-2900	$03^h47^m00^s$	$-29°00'24''$	5.1 ±0.7	-0.87
J0348-1254	$03^h48^m41^s$	$-12°54'59''$	7.1 ±0.9	-1.04
PKS 0346-298	$03^h48^m48^s$	$-29°44'30''$	5.4 ±0.7	-1.18
J0351-1429	$03^h51^m28^s$	$-14°29'08''$	20.8 ±1.3	-0.58
J0351-2744	$03^h51^m35^s$	$-27°44'32''$	30.3 ±1.0	-0.65
J0351-3434	$03^h51^m39^s$	$-34°34'37''$	6.0 ±0.8	-1.05
J0351-4126	$03^h51^m55^s$	$-41°26'21''$	5.4±0.8	-1.14
J0352-0711	$03^h52^m30^s$	$-07°11'02''$	14.6 ±1.4	-0.36
J0355-4823	$03^h55^m29^s$	$-48°23'03''$	8.4 ±1.0	-0.79
J0359-3700	$03^h59^m47^s$	$-37°00'29''$	10.7 ±0.9	-0.82
J0359-2433	$03^h59^m56^s$	$-24°33'59''$	5.7 ±0.8	-0.97
J0400-1610	$04^h00^m16^s$	$-16°10'13''$	10.2 ±1.0	-0.59
J0405-3404	$04^h05^m03^s$	$-34°04'57''$	5.2 ±0.7	-0.89
J0405-1308	$04^h05^m33^s$	$-13°08'14''$	8.6 ±1.1	-0.24

Source ID	α	δ	F (Jy)	β
J0407-3152	$04^{\mathrm{h}}07^{\mathrm{m}}01^{\mathrm{s}}$	$-31^\circ52'02''$	6.3 ±0.8	-1.09
J0407-1211	$04^{\mathrm{h}}07^{\mathrm{m}}48^{\mathrm{s}}$	$-12^\circ11'36''$	12.8 ±1.3	-0.45
J0408-3100	$04^{\mathrm{h}}08^{\mathrm{m}}25^{\mathrm{s}}$	$-31^\circ00'40''$	6.1 ±0.7	-1.19
LEDA2823818	$04^{\mathrm{h}}08^{\mathrm{m}}49^{\mathrm{s}}$	$-24^\circ18'21''$	9.5 ±0.9	-1.0
J0409-1757	$04^{\mathrm{h}}09^{\mathrm{m}}06^{\mathrm{s}}$	$-17^\circ57'10''$	6.1 ±0.8	-0.08
J0411-3513	$04^{\mathrm{h}}11^{\mathrm{m}}22^{\mathrm{s}}$	$-35^\circ13'15''$	6.1 ±0.8	-1.16
J0412-5600	$04^{\mathrm{h}}12^{\mathrm{m}}48^{\mathrm{s}}$	$-56^\circ00'48''$	10.3 ±1.4	-0.42
J0413-3429	$04^{\mathrm{h}}13^{\mathrm{m}}00^{\mathrm{s}}$	$-34^\circ30'10''$	10.1 ±0.9	-0.84
J0415-2929	$04^{\mathrm{h}}15^{\mathrm{m}}08^{\mathrm{s}}$	$-29^\circ29'05''$	10.1 ±0.9	-0.99
J0415-4223	$04^{\mathrm{h}}15^{\mathrm{m}}08^{\mathrm{s}}$	$-42^\circ23'02''$	5.6 ±0.8	-0.85
J0416-2056	$04^{\mathrm{h}}16^{\mathrm{m}}04^{\mathrm{s}}$	$-20^\circ56'27''$	12.1 ±1.1	-0.51
J0419-3949	$04^{\mathrm{h}}19^{\mathrm{m}}46^{\mathrm{s}}$	$-39^\circ49'48''$	6.1 ±0.8	-0.68
J0420-4126	$04^{\mathrm{h}}20^{\mathrm{m}}37^{\mathrm{s}}$	$-41^\circ26'08''$	7.4 ±0.9	-0.99
J0422-2616	$04^{\mathrm{h}}22^{\mathrm{m}}34^{\mathrm{s}}$	$-26^\circ16'56''$	7.8 ±0.9	-0.79
J0422-3315	$04^{\mathrm{h}}22^{\mathrm{m}}53^{\mathrm{s}}$	$-33^\circ15'15''$	5.9 ±0.7	-0.82
J0423-3402	$04^{\mathrm{h}}23^{\mathrm{m}}47^{\mathrm{s}}$	$-34^\circ02'42''$	7.6 ±0.9	-0.73
J0426-2643	$04^{\mathrm{h}}26^{\mathrm{m}}41^{\mathrm{s}}$	$-26^\circ43'48''$	5.9 ±0.8	-0.59
J0429-5349	$04^{\mathrm{h}}29^{\mathrm{m}}06^{\mathrm{s}}$	$-53^\circ49'38''$	21.5 ±1.4	-0.39
J0429-3630	$04^{\mathrm{h}}29^{\mathrm{m}}40^{\mathrm{s}}$	$-36^\circ30'56''$	19.2 ±1.0	-0.82
J0430-4153	$04^{\mathrm{h}}30^{\mathrm{m}}03^{\mathrm{s}}$	$-41^\circ53'16''$	6.1 ±0.8	-1.16
J0430-2800	$04^{\mathrm{h}}30^{\mathrm{m}}17^{\mathrm{s}}$	$-28^\circ00'33''$	6.9 ±0.9	-1.02
J0432-2956	$04^{\mathrm{h}}32^{\mathrm{m}}59^{\mathrm{s}}$	$-29^\circ56'19''$	9.0 ±0.9	-0.90
NA	$04^{\mathrm{h}}33^{\mathrm{m}}19^{\mathrm{s}}$	$-29^\circ10'09''$	5.9±0.9	NA
J0434-1322	$04^{\mathrm{h}}34^{\mathrm{m}}10^{\mathrm{s}}$	$-13^\circ22'12''$	10.1±1.1	-1.73
J0436-2226	$04^{\mathrm{h}}36^{\mathrm{m}}35^{\mathrm{s}}$	$-22^\circ26'32''$	6.4±0.9	NA
J0437-3312	$04^{\mathrm{h}}37^{\mathrm{m}}08^{\mathrm{s}}$	$-33^\circ12'15''$	6.4 ±0.9	-0.89
J0437-2954	$04^{\mathrm{h}}37^{\mathrm{m}}36^{\mathrm{s}}$	$-29^\circ54'05''$	7.4 ±0.9	-0.98
J0438-4736	$04^{\mathrm{h}}38^{\mathrm{m}}13^{\mathrm{s}}$	$-47^\circ36'56''$	9.0 ±1.3	-1.52
HB89 0438-436	$04^{\mathrm{h}}40^{\mathrm{m}}15^{\mathrm{s}}$	$-43^\circ33'13''$	7.9±1.1	-0.06
PKS 0442-28	$04^{\mathrm{h}}44^{\mathrm{m}}35^{\mathrm{s}}$	$-28^\circ09'55''$	43.8±1.0	-0.84
J0444-2851	$04^{\mathrm{h}}44^{\mathrm{m}}43^{\mathrm{s}}$	$-28^\circ51'42''$	7.1±0.9	-0.78
J0445-3838	$04^{\mathrm{h}}45^{\mathrm{m}}12^{\mathrm{s}}$	$-38^\circ38'38''$	7.8 ±1.1	-1.31
J0445-3305	$04^{\mathrm{h}}45^{\mathrm{m}}59^{\mathrm{s}}$	$-33^\circ05'00''$	7.8 ±1.1	-1.39
J0447-2032	$04^{\mathrm{h}}47^{\mathrm{m}}29^{\mathrm{s}}$	$-20^\circ32'08''$	7.8 ±0.9	NA
NA	$04^{\mathrm{h}}47^{\mathrm{m}}30^{\mathrm{s}}$	$-46^\circ20'19''$	13.1 ±1.4	NA
J0452-3840	$04^{\mathrm{h}}52^{\mathrm{m}}03^{\mathrm{s}}$	$-38^\circ40'23''$	7.5 ±1.0	-1.46
J0452-2201	$04^{\mathrm{h}}52^{\mathrm{m}}44^{\mathrm{s}}$	$-22^\circ01'18''$	7.4 ±0.9	-0.83

Source ID	α	δ	F (Jy)	β
J0453-4156	$04^{h}53^{m}55^{s}$	$-41^\circ56'51''$	8.0 ±0.9	-1.08
J0455-3006	$04^{h}55^{m}14^{s}$	$-30^\circ06'49''$	19.5 ±1.0	-0.76
J0455-2034	$04^{h}55^{m}23^{s}$	$-20^\circ34'14''$	15.9 ±1.1	-0.34
J0455-4615	$04^{h}55^{m}51^{s}$	$-46^\circ16'03''$	10.0±1.2	-0.86
J0456-2159	$04^{h}56^{m}09^{s}$	$-21^\circ59'15''$	10.3 ±1.1	-0.74
J0458-4029	$04^{h}58^{m}13^{s}$	$-40^\circ29'54''$	7.9 ±1.1	-1.81
J0458-3007	$04^{h}58^{m}26^{s}$	$-30^\circ07'23''$	14.8 ±1.0	-0.99
J0504-1014	$05^{h}04^{m}53^{s}$	$-10^\circ14'50''$	10.6 ±1.5	-0.82
J0505-2856	$05^{h}05^{m}34^{s}$	$-28^\circ56'25''$	7.7 ±1.1	-0.33
PKS 0503-284	$05^{h}05^{m}40^{s}$	$-28^\circ24'39''$	9.0 ±1.1	-0.87
J0507-3842	$05^{h}07^{m}56^{s}$	$-38^\circ42'20''$	8.7 ±1.1	-1.22
J0510-1838	$05^{h}10^{m}32^{s}$	$-18^\circ38'37''$	17.8±1.2	-1.27
J0511-2201	$05^{h}11^{m}00^{s}$	$-22^\circ01'45''$	8.9±1.1	-0.56
J0511-3315	$05^{h}11^{m}01^{s}$	$-33^\circ15'49''$	8.2 ±1.0	-0.96
J0512-4824	$05^{h}12^{m}51^{s}$	$-48^\circ24'21''$	18.7±1.3	-0.35
J0513-3028	$05^{h}13^{m}33^{s}$	$-30^\circ28'09''$	15.6 ±1.0	-0.57
J0514-4845	$05^{h}14^{m}31^{s}$	$-48^\circ45'30''$	10.1 ±1.4	-0.92
NA	$05^{h}15^{m}07^{s}$	$-45^\circ41'07''$	11.0 ±1.2	NA
J0515-4933	$05^{h}15^{m}11^{s}$	$-49^\circ33'03''$	10.5 ±1.3	-1.36
J0521-2047	$05^{h}21^{m}38^{s}$	$-20^\circ47'39''$	13.8 ±1.1	-0.64
J0522-3627	$05^{h}22^{m}58^{s}$	$-36^\circ27'31''$	63.4 ±1.1	-0.56
J0523-4816	$05^{h}23^{m}19^{s}$	$-48^\circ16'15''$	11.5 ±1.4	-1.54
J0523-3251	$05^{h}23^{m}33^{s}$	$-32^\circ51'24''$	8.7 ±1.1	-0.88
J0523-3408	$05^{h}23^{m}41^{s}$	$-34^\circ08'13''$	7.2±1.0	-1.53
NA	$05^{h}25^{m}23^{s}$	$-44^\circ35'57''$	10.5±1.2	NA
J0525-3242	$05^{h}25^{m}27^{s}$	$-32^\circ42'30''$	9.0±1.1	NA
J0531-3032	$05^{h}31^{m}15^{s}$	$-30^\circ32'06''$	7.3 ±1.0	-1.17
J0533-4552	$05^{h}33^{m}36^{s}$	$-45^\circ52'38''$	10.5±1.3	-1.12
PKS 0532-449	$05^{h}34^{m}05^{s}$	$-44^\circ55'39''$	10.8±1.2	-1.35
PKS 0532-378	$05^{h}34^{m}17^{s}$	$-37^\circ47'25''$	11.2±1.3	-1.22
NVSS J053517-052420	$05^{h}35^{m}18^{s}$	$-05^\circ24'21''$	30.0 ±1.8	0.52
J0536-4944	$05^{h}36^{m}13^{s}$	$-49^\circ44'26''$	13.8 ±1.4	-0.72
J0539-3412	$05^{h}39^{m}47^{s}$	$-34^\circ12'33''$	8.9 ±1.1	-1.08
J0540-3309	$05^{h}40^{m}17^{s}$	$-33^\circ09'11''$	8.0 ±1.1	-1.33
J0543-2420	$05^{h}43^{m}07^{s}$	$-24^\circ20'55''$	9.5 ±1.2	-1.10
PKS 0543-479	$05^{h}45^{m}05^{s}$	$-47^\circ56'50''$	10.4 ±1.4	-1.11
J0545-3159	$05^{h}45^{m}15^{s}$	$-31^\circ59'36''$	8.0 ±1.2	-1.26

Source ID	α	δ	F (Jy)	β
J0547-4431	$05^{\rm h}47^{\rm m}39^{\rm s}$	$-44°31'07''$	10.8 ±1.2	-0.89
PKS 0546-459	$05^{\rm h}48^{\rm m}00^{\rm s}$	$-45°54'27''$	10.3 ±1.4	-1.17
J0548-3257	$05^{\rm h}48^{\rm m}26^{\rm s}$	$-32°57'37''$	8.7±1.2	-1.47
J0549-4051	$05^{\rm h}49^{\rm m}23^{\rm s}$	$-40°51'15''$	15.8 ±1.2	-0.65
NA	$05^{\rm h}49^{\rm m}33^{\rm s}$	$-45°24'18''$	10.8 ±1.3	NA
J0556-3223	$05^{\rm h}56^{\rm m}15^{\rm s}$	$-32°23'07''$	9.5 ±1.1	-0.91
J0600-3936	$06^{\rm h}00^{\rm m}31^{\rm s}$	$-39°36'22''$	9.4±1.1	NA
J0602-3819	$06^{\rm h}02^{\rm m}01^{\rm s}$	$-38°19'07''$	9.7±1.2	-0.89
PKS 0600-399	$06^{\rm h}02^{\rm m}22^{\rm s}$	$-39°57'54''$	9.3±1.2	-1.35
J0603-3426	$06^{\rm h}03^{\rm m}11^{\rm s}$	$-34°26'34''$	12.7 ±1.2	-1.06
J0604-3156	$06^{\rm h}04^{\rm m}14^{\rm s}$	$-31°55'54''$	10.5 ±1.2	-0.45
J0605-3518	$06^{\rm h}05^{\rm m}53^{\rm s}$	$-35°18'07''$	9.1 ±1.1	-1.2
J0606-2022	$06^{\rm h}06^{\rm m}33^{\rm s}$	$-20°22'12''$	13.0 ±1.3	-0.56
J0617-3634	$06^{\rm h}17^{\rm m}31^{\rm s}$	$-36°34'12''$	8.8 ±1.2	-0.69
J0620-3711	$06^{\rm h}20^{\rm m}01^{\rm s}$	$-37°11'32''$	11.7 ±1.3	-0.78
J0621-4504	$06^{\rm h}21^{\rm m}00^{\rm s}$	$-45°04'39''$	10.6 ±1.4	-1.03
J0621-5241	$06^{\rm h}21^{\rm m}43^{\rm s}$	$-52°41'32''$	17.5 ±1.8	-0.63
J0626-5341	$06^{\rm h}26^{\rm m}20^{\rm s}$	$-53°41'14''$	47.6 ±1.8	-0.85
J0626-5432	$06^{\rm h}26^{\rm m}46^{\rm s}$	$-54°32'31''$	21.9 ±1.9	-1.06
J0627-3529	$06^{\rm h}27^{\rm m}06^{\rm s}$	$-35°29'13''$	20.5 ±1.3	-0.96
J0627-0553	$06^{\rm h}27^{\rm m}10^{\rm s}$	$-05°53'4''$	46.7 ±2.1	-0.04
J0636-2036	$06^{\rm h}36^{\rm m}31^{\rm s}$	$-20°36'52''$	32.5 ±1.5	-0.36
J0639-2745	$06^{\rm h}39^{\rm m}55^{\rm s}$	$-27°45'09''$	9.4 ±1.2	-1.06
J0644-4344	$06^{\rm h}44^{\rm m}26^{\rm s}$	$-43°44'11''$	10.3 ±1.4	-1.10
J0648-3957	$06^{\rm h}48^{\rm m}11^{\rm s}$	$-39°57'11''$	16.2 ±1.5	-0.96
J0658-2417	$06^{\rm h}58^{\rm m}58^{\rm s}$	$-24°17'27''$	26.4 ±1.5	-1.00
J0705-4248	$07^{\rm h}05^{\rm m}54^{\rm s}$	$-42°48'51''$	11.3 ±1.5	-0.93
PKS 0707-35	$07^{\rm h}09^{\rm m}29^{\rm s}$	$-36°03'37''$	11.6 ±1.4	-0.83
J0711-2043	$07^{\rm h}11^{\rm m}47^{\rm s}$	$-20°43'13''$	14.3 ±1.7	-0.64
J0717-3621	$07^{\rm h}17^{\rm m}08^{\rm s}$	$-36°21'59''$	15.1 ±1.5	-0.75
J0717-2504	$07^{\rm h}17^{\rm m}17^{\rm s}$	$-25°04'53''$	16.9 ±1.7	-0.46
PMNJ0737-3812	$07^{\rm h}37^{\rm m}46^{\rm s}$	$-38°13'02''$	12.7 ±1.7	-0.55
J0749-4412	$07^{\rm h}49^{\rm m}42^{\rm s}$	$-44°12'29''$	15.2 ±1.9	-0.64
J2253-4057	$22^{\rm h}53^{\rm m}03^{\rm s}$	$-40°57'46''$	14.6 ±1.3	-0.05
J2319-2728	$23^{\rm h}19^{\rm m}54^{\rm s}$	$-27°27'59''$	9.7 ±1.2	-0.57
J2321-1622	$23^{\rm h}21^{\rm m}01^{\rm s}$	$-16°23'05''$	10.3 ±1.3	-0.16
J2326-4027	$23^{\rm h}26^{\rm m}34^{\rm s}$	$-40°27'15''$	9.8 ±1.2	-0.06

Source ID	α	δ	F (Jy)	β
J2334-4125	$23^{\mathrm{h}}34^{\mathrm{m}}26^{\mathrm{s}}$	$-41°25'23''$	17.1±1.2	-0.07
J2341-3506	$23^{\mathrm{h}}41^{\mathrm{m}}45^{\mathrm{s}}$	$-35°6'22''$	7.0 ±0.9	-0.21
J2350-2457	$23^{\mathrm{h}}50^{\mathrm{m}}50^{\mathrm{s}}$	$-24°56'59''$	7.3 ±0.9	-0.51
J2357-3445	$23^{\mathrm{h}}57^{\mathrm{m}}01^{\mathrm{s}}$	$-34°45'43''$	16.8 ±0.9	-0.66

Conclusions

Understanding the EoR is a milestone on modern cosmology. The EoR marks the birth of the first stars and galaxies and the last major phase transition of the intergalactic medium from neutral to ionized. The best EoR probe is acknowledged to be the redshifted 21 cm HI line and several radio interferometers have recently been built in order to detect it. Measurements of the redshifted 21 cm line require great sensitivity and exquisite calibration accuracy in order to remove the foreground emission that is orders of magnitude brighter than the 21 cm emission.

In this thesis I analyzed data from the 32–element Donald C. Baker Precision Array to Probe the Epoch of Reionization (PAPER) in order to image the sky region $1^\circ < \delta < 52^\circ$ and $0^{\rm h} < \alpha < 8^{\rm h}$ and $23^{\rm h} < \alpha < 24^{\rm h}$ at 150 MHz with a resolution of $16'$. The images were used to derive a catalogue of 284 compact sources down to a 5 Jy flux density limit, covering $\sim$ 11000 square degrees. I applied the most advanced calibration techniques in order to correct for direction dependent errors around bright sources, enabling a clean measurement of the fainter source population. A multi stage calibration strategy was developed in order to achieve a few percent accuracy in the catalogue's absolute flux density scale. By matching the catalogue sources with 408 MHz measurements from the Parkes-MIT-NRAO catalogue, we found the positions to be accurate within 3 arcminutes. We also derive the spectral index distribution between 150 and 408 MHz, representing the spectral investigation of a large sample of sources at low frequencies. Our spectral index distribution has a mean value $\beta = -0.78$ that agrees with mean spectral index values at 10, 38, 178, 408, 610 and 1421 MHz computed by Williams & Bridle (1967) and is consistent with previous computation of spectral index at frequencies less than 1.4 GHz (DeBreuck et al., 2001; Hunstead, 1991; Oort et al., 1988), with no evidence for a statistical spectral turnover due to synchrotron self–absorption.

The derived catalogue reaches a depth between 3 and 4 orders of magnitude brighter than the expected EoR signal, so it cannot be used to directly subtract the extragalactic foregrounds from EoR observations, but like stated earlier in this thesis, it represents a further step towards creating an accurate global sky model that can be used as an absolute flux density reference scale for EoR observations. A global sky model is crucial to improve interferometric calibration, to map telescope primary beams (Mitchell et al., 2008; Morales & Matejek, 2009) and correct for ionospheric distortions (Bernardi et al., 2010; Intema et al., 2009; Mitchell et al., 2008) in high resolution images of ionized bubbles throughout the EoR (Koopmans et al., 2015).

Bibliography

Ali Z. S., Parsons A. R., Zheng H., Pober J. C., Liu A., Aguirre J. E., Bradley R. F., Bernardi G., et al., 2015, ApJ, 809, 61

Barkana R., Loeb A., 2001, Physics Report, 349, 125

Barkana R., Loeb A., 2004, ApJ, 609, 474

Barkana R., Loeb A., 2008, MNRAS, 384, 1069

Becker G. D., Bolton J. S., Lidz A., 2015, ArXiv e-prints

Bernardi G., de Bruyn A. G., Brentjens M. A., Ciardi B., Harker G., Jelić V., Koopmans L. V. E., Labropoulos P., et al., 2009, aap, 500, 965

Bernardi G., de Bruyn A. G., Harker G., Brentjens M. A., Ciardi B., Jelić V., Koopmans L. V. E., Labropoulos P., et al., 2010, A&A, 522, A67

Bernardi G., Greenhill L. J., Mitchell D. A., Ord S. M., Hazelton B. J., Gaensler B. M., de Oliveira-Costa A., Morales M. F., et al., 2013, ApJ, 771, 105

Beuermann K., Kanbach G., Berkhuijsen E. M., 1985, AAP, 153, 17

Bowman J. D., Morales M. F., Hewitt J. N., 2009, ApJ, 695, 183

Bridle A. H., Baldwin J. E., 1967, MNRAS, 136, 219

Chapman E., Zaroubi S., Abdalla F., 2014, MNRAS

Ciardi B., Ferrara A., White S. D. M., 2003, MNRAS, 344, L7

Cohen A. S., Lane W. M., Cotton W. D., Kassim N. E., Lazio T. J. W., Perley R. A., Condon J. J., Erickson W. C., 2007, AJ, 134, 1245

Condon J. J., Cotton W. D., Greisem E. W., Yin Q. F., Perley R. A., Taylor G. B., Broderick J. J., 1998, The astronomical Journal, 115, 1693

Conway J. E., Sault R. J., 1995, VLBI and the VLBA ASP Conference Series, 82, 309

Cornwell T. J.and Golap K., Bhatnagar S., 2005, Astronomical Data Analysis Software and Systems XIV ASP Conference Series, 347, 86

Cornwell T., Fomalont E. B., 1999, Synthesis Imaging in Radio Astronomy II ASP Conference Series, 180, 187

Cornwell T. J., Perley R. A., 1992, AA, 261, 353

de Oliveira-Costa A., Tegmark M., Gaensler B. M., Jonas J., Landecker T. L., Reich P., 2008, MNRAS, 388, 247

DeBreuck C., vanBreugel W., Röttgering H., Stern D., Miley G., de Vries W., Stanford S. A., Kurk J., Overzier R., 2001, The Astronomical Journal, 121, 1241

DeBreuck C., vanBreugel W., Röttgering H. J. A., Miley G., 2000, A&A Supplement Series, 143, 303

Di Matteo T., Perna R., Abel T., Rees J. M., 2002, ApJ, 564, 576

Dillon J. S., Tegmark M., Liu A., Ewall-Wice A., Hewitt J. N., Morales M. F., Neben A. R., Parsons A. R., et al., 2015, prd, 91, 023002

Douglas J. N., Bash F. N., Bozyan F. A., Torrence G. W., Wolfe C., 1996, AJ, 111, 1945

Fan X., Carilli C. L., Keating B., 2006, Annual Review of A&A, 44, 415

Fialkov A., Barkana R., Visbal E., 2014, Nature, 506, 197

Field G. B., 1959, ApJ, 129, 536

Furlanetto S. R., 2015, ArXiv e-prints

Furlanetto S. R., Peng Oh S., Briggs F. H., 2006, Physics Reports, 433, 181

Geldzahler B. J., Fomalont E. B., 1984, A.J., 89, 1650

Ghara R., Choudhury T. R., Datta K. K., 2015, MNRAS, 447, 1806

Ginzburg V. L., Syrovatskii S. I., 1965, Annual Review of Astronomy and Astrophysics, 3, 297

Gleser L., Nusser A., Benson A. J., 2008, MNRAS, 391, 383

Hamaker J. P., Bregman J. D., Sault R. J., 1996, A&A Supplement, 177, 137

Harker G., Zaroubi S., Bernardi G., Brentjens M. A., de Bruyn A. G., Ciardi B., Jelić V., Koopmans L. V. E., et al., 2009, MNRAS, 397, 1138

Haslam C. G. T., Salter C. J., Stoffel H., Wilson W. E., 1982, A&A Supplement, 47, 1,2,4

Heald G. H., Pizzo R. F., Orrú E., Breton R. P., Carbone D., Ferrari C., Hardcastle M. J., Jurusik W., et al., 2015, AAP, 582, A123

Hunstead R. W., 1991, Australian Journal of Physics, 44, 743

Hurley-Walker N., Morgan J., Wayth R. B., Hancock P. J., Bell M. E., Bernardi G., Bhat R., Briggs F., et al., 2014, Publications of the Astronomical Society of Australia, 31, 45

Iliev I., Santos M., Mesinger A., Majumdar S., Mellema G., 2015, Advancing Astrophysics with the Square Kilometre Array (AASKA14), p. 7

Intema H. T., van der Tol S., Cotton W. D., Cohen A. S., van Bemmel I. M., Röttgering H. J. A., 2009, A&A, 501, 1185

Jacobs D. C., 2011, Scholarly Commons - Publicly accessible Penn dissertations

Jacobs D. C., Aguirre J. E., Parsons A. R., Pober J. C., Bradley R. F., Carilli C. L., Gugliucci N. E., Manley J. R., et al., 2011, The Astrophysical Journal Letters, 734, L34

Jacobs D. C., Parsons A. R., Aguirre J. E., Ali Z., Bowman J., Bradley R. F., Carilli C. L., DeBoer D. R., et al., 2013, ApJ, 776, 108

Jacobs D. C., Pober J. C., Parsons A. R., Aguirre J. E., Ali Z. S., Bowman J., Bradley R. F., Carilli C. L., et al., 2015, ApJ, 801, 51

Jelić V., Zaroubi S., Labropoulos P., Thomas R. M., Bernardi G., Brentjens M. A., de Bruyn A. G., Ciardi B., et al., 2008, MNRAS, 389, 1319

Jensen H., Datta K. K., Mellema G., Chapman E., Abdalla F. B., Iliev I. T., Mao Y., Santos M. G., et al., 2013, MNRAS, 435, 460

Junklewitz H., Bell M. A., Enßlin T., 2014, A&A, p. 13

Koopmans L., Pritchard J., Mellema G., Aguirre J., Ahn K., Barkana R., van Bemmel I., Bernardi G., et al., 2015, Advancing Astrophysics with the Square Kilometre Array (AASKA14), p. 1

Lawson K. D., Mayer C. J., Osborne J. L., Parkinson M. L., 1987, MNRAS, 225, 307

Lidz A., Zahn O., McQuinn M., Zaldarriaga M., Hernquist L., 2008, ApJ, 680, 962

Liu A., Parsons A. R., Trott C. M., 2014a, PRD, 90, 023018

Liu A., Parsons A. R., Trott C. M., 2014b, PRD, 90, 023019

Liu A., Tegmark M., Bowman J., Hewitt J., Zaldarriaga M., 2009, MNRAS, 398, 401

Loeb A., Zaldarriaga M., 2004, Physical Review Letters, 92, 211301

Loi S. T., Murphy T., Bell M. E., Kaplan D. L., Lenc E., Offringa A. R., Hurley-Walker N., Bernardi G., et al., 2015, MNRAS, 453, 2731

Madau P., Meiksin A., Rees M. J., 1997, ApJ, 475, 429

Maddox S. J., Efstathiou G., Sutherland W. J., Loveday J., 1990, MNRAS, 243, 692

Mauch T., Murphy T., Buttery H. J., Curran J., Hunstead R. W., Piestrzynski B., Robertson J. G., Sadler E. M., 2003, MNRAS, 342, 1117

McQuinn M., Lidz A., Zahn O., Suvendra D., Lars H., Matias Z., 2007, MNRAS, 377, 1043

Mellema G., Iliev I. T., Pen U.-L., Shapiro P. R., 2006, MNRAS, 372, 679

Mellema G., Koopmans L., Shukla H., Datta K. K., Mesinger A., Majumdar S., 2015, Advancing Astrophysics with the Square Kilometre Array (AASKA14), p. 10

Mesinger A., Ferrara A., Greig B., Iliev I., Mellema G., Pritchard J., Santos M., 2015, Advancing Astrophysics with the Square Kilometre Array (AASKA14), p. 11

Mesinger A., Furlanetto S., Cen R., 2011, MNRAS, 411, 955

Mitchell D. A., Greenhill L. J., Wayth R. B., Sault R. J., Lonsdale C. J., Cappallo R. J., Morales M. F., Ord S. M., 2008, IEEE Journal of Selected Topics in Signal Processing, Special Issue on Signal Processing for Astronomical and Space Research Applications, 44

Mohan N., Rafferty D., , 2015, PyBDSM: Python Blob Detection and Source Measurement, Astrophysics Source Code Library

Moore D. F., Aguirre J. E., Parsons A. R., Jacobs D. C., Pober J. C., 2013, ApJ, 769, 154

Morales M. F., Bowman J. D., Hewitt J. N., 2006, ApJ, 648, 767

Morales M. F., Hewitt J., 2004, ApJ, 615, 7

Morales M. F., Matejek M., 2009, MNRAS, 400, 1814

Morales M. F., Wyithe J. S. B., 2010, Annual Review of Astronomy and Astrophysics, 48, 127

Mortlock D. J., 2015, ArXiv e-prints

Moshir M., Kopman G., Conrow T. A. O., 1992, IRAS Faint Source Survey, Explanatory supplement version 2

Noordam J. E., 2004, Society of Photo-Optical Instrumentation Engineers (SPIE) Conference Series,, 5489, 9

Oort M. J. A., Steemers W. J. G., Windhorst R. A., 1988, Astronomy and Astrophysics Supplement Series, 73, 103

Paciga G., Albert J. G., Bandura K., Chang T.-C., Gupta Y., Hirata C., Odegova J., Pen U.-L., et al., 2013, MNRAS, 433, 639

Pacucci F., Mesinger A., Mineo S., Ferrara A., 2014, MNRAS, 443, 678

Parsons A. R., Backer D. C., 2009, ApJ, 138, 219

Parsons A. R., Backer D. C., Foster G. S., Wright M. C. H., Bradley R. F., Gugliucci N. E., Parashare C. R., Benoit E. E., et al., 2010, A.J., 139, 1468

Parsons A. R., Liu A., Aguirre J. E., Ali Z. S., Bradley R. F., Carilli C. L., DeBoer D. R., Dexter M. R., et al., 2014, ApJ, 788, 106

Pearson T. J., Readhead A. C. S., 1984, Annual review of astronomy and astrophysics, 22, 97

Pentericci L., Vanzella E., Fontana A., Castellano M., Treu T., Mesinger A., Dijkstra M., Grazian A., et al., 2014, ApJ, 793, 113

Perley R. A., Butler B. J., 2012, Instrumentation and Methods for Astrophysics (astro-ph.IM); Earth and Planetary Astrophysics (astro-ph.EP), 204

Perley R. A., Roser H. J., Meisenheimer K., 1997, A&A, 328, 12

Petrovic N., Oh S. P., 2011, MNRAS, 413, 2103

Planck Collaboration 2015, ArXiv e-prints

Platania P., Bensadoun M., Bersanelli M., De Amici G., Kogut A., Levin S., Maino D., Smoot G. F., 1998, ApJ, 505, 473

Pober J. C., Parsons A. R., Aguirre J. E., Ali Z., Bradley R. F., Carilli C. L., DeBoer D., Dexter M., et al., 2013, The ApJ Letters, 768, L36

Prandoni I., Gregorini L., Parma P., de Ruiter H. R., Vettolani G., Wieringa M. H., Ekers R. D., 2000, A&AS, 146, 41

Pritchard J., Loeb A., 2010, Nature, 468, 772–773

Pritchard J. R., Furlanetto S. R., 2007, MNRAS, 376, 1680

Reichardt C. L., 2015, ArXiv e-prints

Rengelink R. B., Tang Y., de Bruyn A. G., Miley G. K., Bremer M. N., Roettgering H. J. A., Bremer M. A. R., 1997, AAPS, 124

Robertson B. E., Ellis R. S., Dunlop J. S., McLure R. J., Stark D. P., 2010, Nature, 468, 49

Robertson B. E., Ellis R. S., Furlanetto S. R., Dunlop J. S., 2015, ApJ, 802, L19

Rogers A. E. E., Bowman J. D., 2008, AJ, 136, 641

Rybicki G. B., Lightman A. P., 1979, Radiative Processes in Astrophysics. A Wiley-Interscience publication, Wiley

Santos M. G., Cooray A., Knox L., 2005, ApJ, 625, 575

Sault R. J., Hamaker J. P., Bregman J. D., 1996, A&A Supplement, 177, 149

Sault R. J., Staveley-Smith L., Brouw W. N., 1996, Astron. Astrophys. Suppl. Ser., 120, 375

Seo H.-J., Eisenstein D. J., 2005, ApJ, 633, 575

Shaver P. A., Windhorst R. A., Madau P., de Bruyn A. G., 1999, A&A, 345, 380

Sironi G., 1976, Astrophysics and Space Science, 44, 159

Skrutskie M. F., Cutri R. M., Stiening R., Weinberg M. D., Schneider S., Carpenter J. M., Beichman C., Capps R., et al., 2006, AJ, 131, 1163

Smirnov O. M., 2011a, A&A, 527

Smirnov O. M., 2011b, A&A, 527, A107

Sobacchi E., Mesinger A., 2014, MNRAS, 440, 1662

Stark D. P., Ellis R. S., Ouchi M., 2011, ApJ, 728, L2

Tegmark M., Eisenstein D. J., Strauss M. A., Weinberg D. H., Blanton M. R., Frieman J. A., Fukugita M., Gunn J. E., et al., 2006, Physical Review D, 74, 123507

Thompson A. R., Moran J. M., Swenson, Jr. G. W., 1986, Interferometry and Synthesis in Radio Astronomy, 2 edn. Wiley, New York

Ungruhe R., Seitter W. C., Duerbeck H. W., 2003, Journal of Astronomical Data, 9, 1

Valdes M., Evoli C., Ferrara A., 2010, MNRAS, 404, 1569

Varela J., D'Onofrio M., Marmo C., Fasano G., Bettoni D., Cava A., Couch W. J., Dressler A., et al., 2009, AAP, 497, 667

Vedantham H., Udaya Shankar N., Subrahmanyan R., 2012, ApJ, 745, 176

Vedantham H. K., Koopmans L. V. E., de Bruyn A. G., Wijnholds S. J., Ciardi B., Brentjens M. A., 2014, MNRAS, 437, 1056

Wang X., Tegmark M., Santos M. G., Knox L., 2006, ApJ, 650, 529

Williams P. J. S., Bridle A. H., 1967, The Observatory, 87, 280

Wouthuysen S. A., 1952, A.J., 57, 31

Wright A., Otrupcek R., 1990, in PKS Catalog (1990) Parkes Catalog, 1990, Australia telescope national facility.. p. 0

Xu X., White M., Padmanabhan N., Eisenstein D. J., Eckel J., Mehta K., Metchnik M., Pinto P., et al., 2010, ApJ, 718, 1224

Yatawatta S., de Bruyn A. G., Brentjens M. A., Labropoulos P., Pandey V. N., Kazemi S., Zaroubi S., Koopmans L. V. E., et al., 2013, A&A, 550, A136

Zaldarriaga M., Furlanetto S. R., Hernquist L., 2004, ApJ, 608, 622

Zaroubi S., Thomas R. M., Sugiyama N., Silk J., 2007, MNRAS, 375, 1269